Max-Planck-Institute for Solid State Research
Stuttgart, Germany

Synthesis and Characterization of New Alkali-Metal Oxometalates Obtained via the Azide-Nitrate Route

Katarina Đuriš

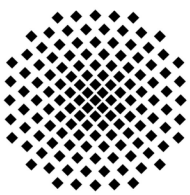

Faculty of Chemistry, University of Stuttgart, Germany

Synthesis and Characterization of New Alkali-Metal Oxometalates Obtained via the Azide-Nitrate Route

Von der Fakultät Chemie der Universität Stuttgart
zur Erlangung der Würde eines Doktors der
Naturwissenschaften (Dr. rer. nat.) genehmigte Abhandlung

Vorgelegt von

Katarina Đuriš

aus Padina, Serbien

Hauptberichter:	Prof. Dr. Dr. h. c. Martin Jansen
Mitberichter:	Prof. Dr. Thomas Schleid
Prüfungsvorsitzender:	Prof. Dr. Joris van Slageren

Tag der mündlichen Prüfung: 13.02.2013

Max-Planck-Institut für Festkörperforschung, Stuttgart
2013

"Ask, and you will receive. Search, and you will find. Knock, and the door will be opened to you." (Matthew 7:7).

To my family...

Acknowledgements

This dissertation would not have been possible without the guidance and the help of several individuals who in one way or another contributed and extended their valuable assistance in the preparation and completion of this study. I would like to thank **Prof. Dr. Dr. h.c. Martin Jansen**, in the first place, for the opportunity to join his team, as well as his continuous support and motivation throughout this work. I am really very thankful for his guidance and his numerous advices given throughout this thesis.

My sincere thanks to my Ph.D. examination committee members **Prof. Dr. Thomas Schleid** and **Prof. Dr. Joris van Slageren** for their evaluation of my Ph.D. thesis.

Also I would like to thank to:

Dr Ulrich Müller for valuable discussion and suggestion concerning the disorder in the structure, as well as group-subgroup relations.

Dr Dieter Fischer for the friendly guidance and encouragement throughout all the time.

Mr. Claus Mühle and **Ms. Sabine Prill-Diemer** for the support during experimental part.

I am very thankful to **Dr. Steffen Pfeifer**, **Dr Naveed Zafar Ali**, (azide/nitrate route group members) for numerous helpful suggestions during the experimental work.

Dr Jürgen Nuss not only for measurement and solution of single-crystal data, but also for his patience and helpful discussions.

Dr Reinhard Keimer and **Dr Hanne Nuss** for their help, enthusiasm and discussion related to some areas of this thesis, especially magnetic measurements.

Dr Christian Schön for his support, helpful discussions and patience in reading and correcting this thesis.

Ms. Marie-Luise Schreiber for quantitative elemental analysis measurements.

Ms. Sabine Paulsen and **Ms. Birgit King** for invaluable assistance in general administrative matters.
Ms. Eva Brücher and **Ms. Gisela Siegle**, for constant assistance in magnetization and specific heat measurements.
Ms. Oxana Magdysyuk for her constant support and patient help, in especially solving the structures from the powder data.
Dr. Jakob Wilfert and **Dr. Thomas Pilz** for the thermal analysis measurements.
I am indebted to **Dr. H. G. Libuda** for his support and IMPRS-AM for funding this research.
For the helpful discussions, suggestions as well as providing a nice atmosphere I would like to thank **Dr. D. Zagorac, Dr. V. Todorova, D. Bragines, Dr. F. Schurz, Dr. Fei Wang, T. Runčevski, Dr. V. Saltykov, M. Kabdulov, Dr. R. Hübner, A. Sanns** and of course all the members of the Department.

Needless to say, a thousand thanks go directly to my family for their love, patience and support.

Contents

List of Figures

List of Tables

Part I.

Introduction

1.

Introduction

Transition metal oxides continue to be a central field of research in solid state chemistry and materials research. Much of the interest is due to their properties like high T_c superconductivity or magnetoresistance that have been discovered to occur in some multinary transition oxides.

Quite generally, there is an endless search for new materials that have to meet the demands of advanced technology. One of the greatest challenges of solid state chemistry today is the design and the synthesis of novel inorganic solids possessing desired structures and properties [3–5]. For example, microporous and mesoporous structures are employed for molecular sieves and catalysts; layered structures containing CuO_2 sheets are desired for high critical temperature superconductivity. In the context of energy materials, there are several requirements materials must fulfill to meet the challenges: for example, one needs more efficient photocatalytic materials for the utilization of solar energy [6], better electrode materials in fuel cells [7], new thermoelectric materials [8], materials for spintronics application [9], multiferroics [10], novel high-performance ceramics [11], pigments [12], etc. the list is endless.

Due to the increase interest in the physical phenomena mentioned, the quest for new materials has intensified and a wide range of compounds has been investigated. Among others, alkali-metal oxometalates have attracted attention due to the wide variety of physical properties they exhibit, being insulators as well as ionic or metallic conductors, or even superconductors (Na_xCoO_2 [13]). Furthermore, this class of materials also attract attention due to their interesting structural features, where the transition metal ions exhibit a wide variety of oxidation states as well as coordination numbers (K_2FeO_4, K_3NiO_2) [14,15]. Due to this, it does not come as a surprise that

alkali-metal oxometalates continue to be a rich source of inspiration in basic research and a fertile ground for creating functional materials [16].

Chemical methods of materials synthesis play a crucial role in designing and discovering new materials as well as providing better and less cumbersome methods for preparing known materials [17]. While tailor materials of desired structures and properties remains the holly grail of solid state chemistry and materials science, it is not always possible. A large variety of inorganic solids has been prepared in recent years by the traditional ceramic method, which involves mixing and grinding powders of the constituent oxides, carbonates, etc. And heating them at high temperatures with intermediate grinding when necessary. A wide range of conditions, often at the limits of synthesis methods, such as very high temperatures or pressures, very low oxygen fugacities and rapid quenching, have been employed in material synthesis. The-low temperature chemical routes are however, of even greater interest. The trend now a days is to avoid brute-force methods in order to have better control of the structure, stoichiometry and phase purity. There have been significant attempts in recent years to overcome the limitations of conventional synthetic methods, resulting in the development of alternative routes for solid state synthesis. These new methods have not only enabled the synthesis of known materials in a state of high purity at far lower temperatures than conventional methods, but have resulted in the synthesis of the completely new phases and compounds.

Using classical solid state reactions in the synthesis of transition metal oxides typically results in compounds with "normal" coordination numbers. However recently, the CdO-route has been proposed as a route for the synthesis of alkali-metal oxometalate [18]. This approach may be described as a redox-metathesis kind of reaction: an intermediate alkali-metal oxocadmate is exposed to a transition metal, which reduces cadmium to the metal and binds the alkali component, forming the new alkali metal [16].

Similarly, in 1999, a new method was proposed for the synthesis of alkali-metal oxometallates - azide/nitrate route [19] providing in general a considerably increased thermodynamic driving force and more favorable kinetics conditions force than traditional approaches [16].

The crucial feature of the azide/nitrate route is the analogue to the reaction of sodium azide with sodium nitrite or sodium nitrate, first described by Zintl and Baumbach [20]:

$$3NaN_3 + NaNO_2 = 2Na_2O + 5N_2 \quad (1.1)$$

$$5NaN_3 + NaNO_3 = 3Na_2O + 8N_2 \quad (1.2)$$

This particular method (reactions 1.1 and 1.2) was usually not employed for the preparation of the sodium oxide itself, because the components often react in an unpredictable way, with the high tendency to explode. Nevertheless, the reaction can be used in a controlled manner if several aspects of the reaction are taken into account. Firstly, the starting materials should already contain the transition metal oxide needed for the synthesis of the alkali-metal oxometalate, thus diluting the azide nitrate mixture, and, secondly, the reaction should be conducted in specially designed steel containers (Figure 2.4). Under these conditions, the evolving N_2 can moderate the reaction by increasing the nitrogen partial pressure.

Nevertheless, in spite of the high precautions wile reaction take place, this synthetis approach features several highly beneficial characteristics, such as a simplification of the preparative work, a significantly increased free enthalpy of reaction, and an increased kinetic activation. More importantly, the total composition of the respective product, in particular its oxygen content and thus the valence state of the transition metal involved, can be well controlled by weighing-in the alkali metal azides and nitrates in an appropriate ratio, such as:

$9NaN_3 + 3NaNO_3 + 2ZnO = 2Na_6ZnO_4 + 15N_2$ (neutral)

$7KN_3 + 2KNO_3 + 6CuO = 3K_3Cu_2O_4 + 23/2N_2$ (oxidizing)

$8KN_3 + KNO_3 + 3NiO = 3K_3NiO_2 + 25/2N_2$ (reducing)

$4NaN_3 + NaNO_3 + CuO = Na_5Cu_3O_6 + 13/2\ N_2$ (doping)

The main advantage of the azide/nitrate route is the *in situ* synthesis of the respective alkali oxide which makes the reaction more favorable, and the simplification of the preparative work because the synthesis of alkalimetal oxides can be rather

tedious and difficult task. Especially, for the heavier alkali metal oxides, the traditional procedure involves the preparation and purification of the metal, followed by their oxidation with molecular oxygen to oxides, peroxides, or hyperoxides with a well defined composition. Most interestingly, the thermodynamic driving force of a synthesis along the azide/nitrate route is not only caused by the acid-base reactions but is substantially enhanced by the contributions from the azides and nitrates involved.

The high potential of the azide nitrate route is reflected by a large number of mixed-valent ternary transition metallates with intriguingly complex composition that have been synthesized along this route [16, 21]. An overview about the compounds synthesized by this method is given in reference [16]. For example, by employing this route a new family of intrinsically doped quasi-one-dimensional oxocuprates(II,III) ($Na_{1+x}CuO_2$ [22], [23]) and oxomanganates(II,III) ($A_{1+x}MnO_2$ [21]) have been synthesized. Also, $Na_{10}Co_4O_{10}$, which shows four different types of competing magnetic exchange interactions [24], has been prepare via the azide/nitrate route.

In addition to the actual synthesis, the development of new solid state materials demands more and more an understanding of their properties as they relate to structure. Thus, the present work comprises both the synthesis and the characterization of new alkali-metal oxometalates using the azide/nitrate route. This route has been successfully used in the synthesis of oxonickelate characterized with different structural motives (dumbbells and chain compounds). Furthermore, a new feature in the synthesis has been the introduction of earth alkali azides ($Ba(N_3)_2$) in the process, which shown to be an efficient tool in the synthesis of the new materials containing unusual structural features.

Part II.

General Part

2.

Apparatus and Experimental Conditions

2.1. Handling of Air-Sensitive Materials

Most of the compounds that were used in this work are sensitive to air and moisture. Handling of these materials, as well as their storage were carried out in a highly purifed argon atmosphere. Here, the materials were stored by using the standard Schlenk technique or glove boxes.

2.1.1. Vacuum and Inert Gas Apparatus

The inert conditions were achieved by using a vacuum and inert gas system which is known as "setup line" shown in Figure 2.1 (Duran glass). It consists of a vacuum line and protective gas line filled with argon that are tightened via specially prepared bended stopcocks or teflon valves (Young valves). The argon pressure as well as the vacuum control are adjusted with the help of these teflon valves. The vacuum in the vacuum line setup is obtained with a rotary valve oil pump (Type: RD4, Vacuubrand GmbH). The quality of vacuum is controlled by a Pirani manometer (Thermovac TM 20, Company: Leybold) within a range of 10^{-3}-10^{3} mbar. Silicone grease (Wacker Chemie AG, Munich, Germany) was utilized in order to connect the glasswares to the vacuum line by joints. The reaction vessels that are connected to one of the connectors through the glass spirals and glass bends could be evacuated or filled with a protective gas. Before use, the vessels were heated several times by a gas flame of a gas-burner, where at the same time the whole system was evacuated.

Between heating steps the vessels were filled with argon.

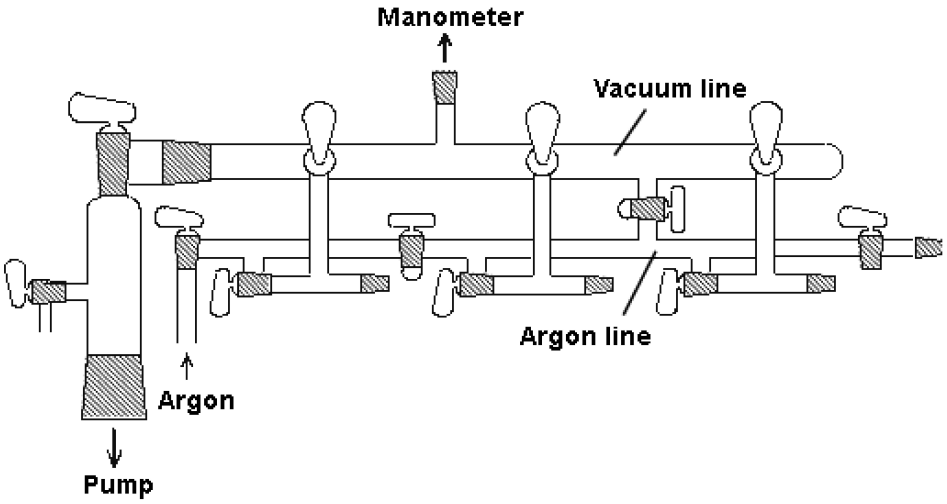

Figure 2.1.: Schematic view of the argon and vacuum line (Schlenk system).

As an inert gas, argon was used, due to its higher density in comparison to air and thus creating higher protection for open vessels in the gas stream. Pure argon (Messer-Griesheim, Krefeld, Germany) was supplied by the low temperature service department (Max Planck Institute, Stuttgart, Germany) through copper lines to a specially designed cleaning setup (Figure 2.2), in order to remove additional traces of oxygen and humidity. Argon gas was firstly passed through the bubble counter filled with paraffin oil (1) to control the gas stream. The first drying tube (2) is filled with a blue gel which is used for preliminary drying. Afterwards, the argon passes through potassium hydroxide (3) to remove the oxygen containing gases (especially CO_2). The molecular sieve in the next drying tube (4) absorbs moisture and carbon hydrides. Phosphorous pentaoxide (P_4O_{10}) (5) is used to remove additional moisture traces. After passing through all drying tubes (made from Duran glass) the argon reaches the drying tube (Quartz) (7) filled with a titanium sponge and heated up to 750 °C by a tube oven, where the rest of oxygen as well as nitrogen are removed. The manometer (8) filled with paraffin oil is used to protect the whole setup from overpressure. Afterwards, the dried argon enters the protective gas line part of the whole vacuum line setup. A trap cooled with liquid nitrogen is connected to the line to protect the vacuum line from solvent vapors or gaseous products.

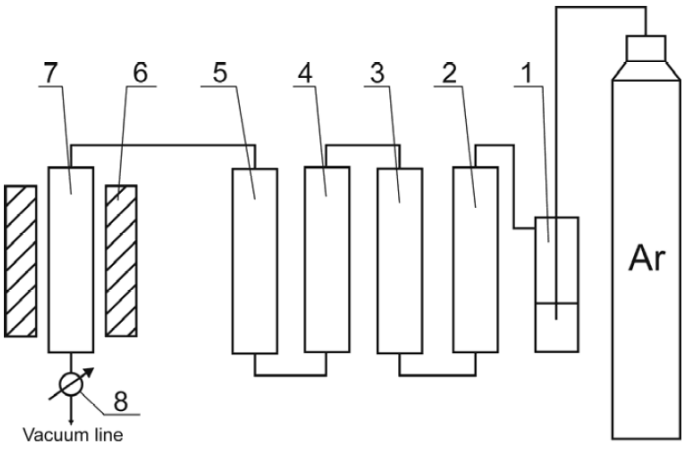

Figure 2.2.: Schematic plot of argon cleaning system.

All important operations under inert conditions were accomplished by use of the standard apparatus (Figure 2.3 *a* and *b*) or a drying tube (Figure 2.3 *c*), which are based on the technology developed by Schlenk [25] for handling air sensitive substances. These apparatuses provide possibilities for substance homogenization using a dried glass rod as well as dividing a sample into smaller amounts by sealing smaller pieces into glass ampoules (5-10 mm in diameter) (see Figure 2.3*b*). Also it is possible to fill capillaries for X-ray analysis with the help of the Schlenk apparatus shown in Figure 2.3*b*. For open apparatuses all operations were performed under the flow of dried argon. The drying tube presented in Figure 2.3 *c* was used for drying the starting components before reaction.

2.1.2. Glove Box

The operations, that could not be performed using the Schlenk setup (e.g. weighing of air sensitive substances or pressing of pellets), were performed in a glove box. The argon filled glove box MB 150B-G-II (M. Braun GmbH, Munich, Germany) was used during experimental work. The inert gas was sent through the molecular sieve and copper contact for cleaning from humidity as well as oxygen. The atmosphere inside the glove box is controlled by the gas analyzers and achieves H_2O and O_2 levels less then 0.1 ppm. Apparatus and samples can be taken into and out of the glove box through a special airtight chamber, which can be evacuated.

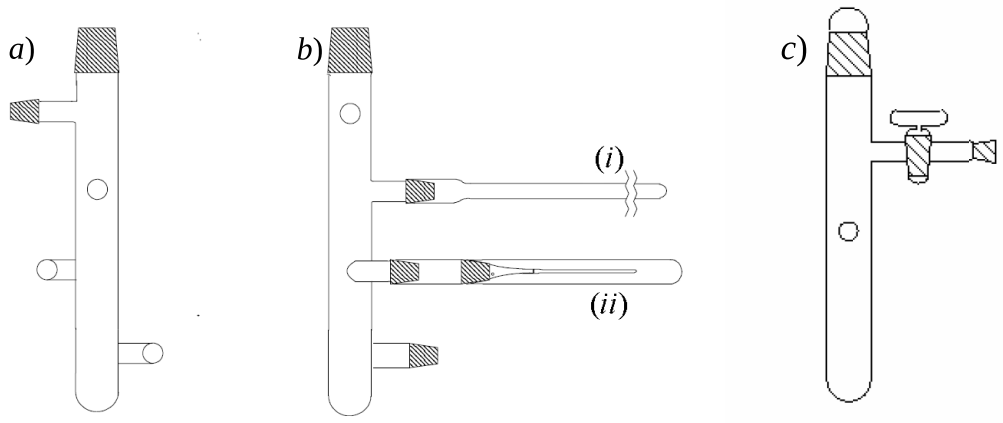

Figure 2.3.: Schlenk apparatus a) and b) having remaining connections for (i) sealing of ampoules, and (ii) filling of capillaries and drying tube (c) (Length ca. 20 cm, diameter ca. 3 cm).

2.2. Synthesis Approaches

Throughout the experimental part of this PhD work, two synthetic approaches were used: Azide/nitrate route and classical solid state synthesis.

2.2.1. Azide/Nitrate Route

As already highlighted in the reactions 1.1 and 1.2, mentioned in the introduction, in the azide/nitrate route during the reaction a significant amount of nitrogen is released. In order to run the reaction safely, special containers had to be constructed.

This cylindrical reaction container is equipped with squeeze seals (Figure 2.4). While the body is made from steel, the inlay consists of special metals according to the requirements of the chemical system under study (in this research Ag inlays were used). Squeeze seals withstand the internal pressure to a certain degree, and they let the nitrogen formed during the reaction escape in a safe manner.

The experimental procedure is always the same and it is independent of the particular system under study. The starting mixture, which consists of the appropriate molar ratio of azides, nitrates and transition metal oxide is good and thoroughly homogenized, for which purpose a ball mill can often be used. Depending on the

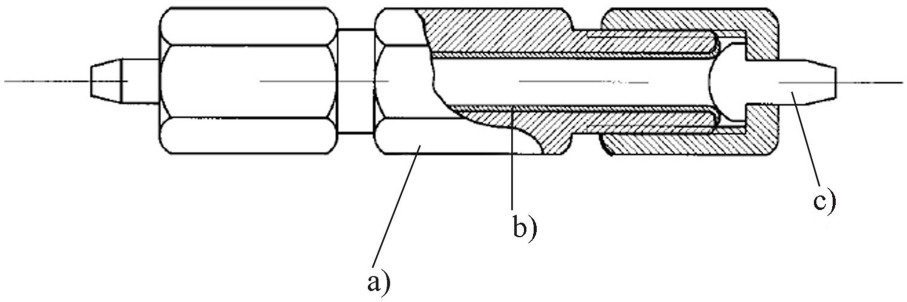

Figure 2.4.: Construction of the steel container for the experiments. a) container, b) inlay, c) stopper.

system under study, the temperature schedule has to be optimized and usually the required annealing temperature is different for each system. In order to run reactions in a controlled manner the heating rate has to be kept low (2–5 K/h), in the temperature range where the decomposition of azides takes place ($\sim$ 533–653 K, for LiN_3 353–653 K).

2.2.2. The Classical Solid State Approach

The most widely used method for the preparation of polycrystalline solids is the so called classical solid state method, which consists of heating together two or more solid materials, which react to form the desired product. In order for the reaction to occur at an appreciable rate, it is necessary to heat the reactants to high temperatures (often over 1273 K), which means that a large input of energy is needed to start the reaction. Raising the temperature enables the reaction at the interface and the atom diffusion through the solid to go faster; however, even at higher temperatures, the diffusion is a limiting step. Due to this fact, it is often important that the starting materials are grinded to give a small particle size, and are well-mixed to maximize the surface contact area and minimize the distance that the reactants have to diffuse.

The mixing of the starting materials during the experimental work was achieved by grinding it in the agate mortar or the ball mill. Employing starting materials with a high specific surface area was also pursued due to higher activity of the starting components, as well as due to lower annealing temperatures. Containers used for the reactions had to withstand higher temperatures and they had to be sufficiently

inert (gold, silver, nickel, corundum, platinum, gold as shown on Figure 2.5).

Figure 2.5.: Different types of containers used during experimental part (from left to right: silver, nickel, corundum, platinum, gold).

Figure 2.6.: Corundum crucible in the quartz ampoule.

The preparation of the alkali oxometalates as well as alkalineearth-transition metal oxides often required that the reaction take place under a special atmosphere, such as Ar, O_2 or vacuum. Pursuing the reactions under vacuum atmosphere, required a specially designed quartz apparatus containing a corundum crucible (Figure 2.6), where before use the whole apparatus was connected to the vacuum line and dried under vacuum. Afterwards, the powder or the pressed pellets were transferred into, and sealed under vacuum (Figure 2.6 right), and further thermally treated.

2.3. Preparation of Single Crystals for X-ray Analysis

In order to obtain single crystals, the products were additionally annealed in silver crucibles, that had been sealed under argon atmosphere in the quartz ampule. In some cases the reactions were left to run for a longer annealing time in the steel containers, followed by cooling at a slow rate (1–5 K/min), to some definite temperature.

Suitable crystals were separated in the glove box compartment under the microscope, picked up using a 0.1 mm sharp edged glass capillary and inserted into a 0.3 mm Lindemann capillary. This bounced capillary was finally sealed under dry argon using a heating filament, to be finally used for single crystal analysis. Before picking the crystals, the capillaries were dried overnight under vacuum.

Preparation of single crystals for X-ray analysis of the extremely air sensitive substances (e.g. Cs_2NiO_2) or single crystals measured at elevated temperatures (e.g. K_3NiO_2), was performed in the apparatus shown in Figure 2.7, which has been specially constructed for searching and mounting single crystals into the capillaries using a modified Schlenk technique. The apparatus consists of one long tube for separating the crystals and two rows, with a 90° angle in-between, of three capillary holders for mounting the crystals.

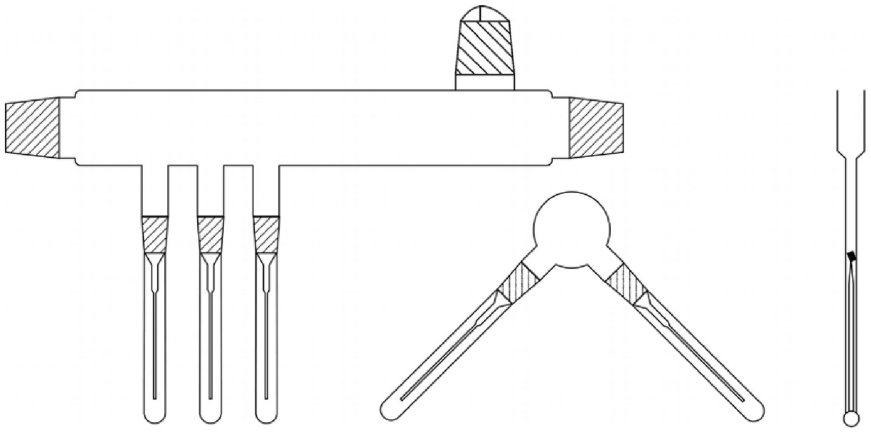

Figure 2.7.: Single crystal mounting apparatus.

The crystalline sample was transferred into the tube through the upper joint, in such a way that the ampoule with crystals is broken under argon stream. The suitable crystals were selected with the help of a stereomicroscope, picked with a

micro-needle and transported to one of the cones of the capillary holder. The Lindemann capillaries (Hildenberg, Malsfeld) were fixed by parafilm (PARAFILMRM) on the capillary holders after heating at 120 °C overnight under vacuum. For better fixing of a crystal in the capillary, a thin pulled-out capillary ($\oslash = 0.1$ mm) was inserted into a second thicker capillary ($\oslash = 0.2$ mm), and both were sealed together at the end (Figure 2.7 right). After mounting the crystals, the capillaries were sealed under argon by a small hand burner after removing the protective jacket.

2.4. High Temperature Facilities

The high temperatures for the syntheses in the present work were achieved in tube furnaces (LOBA type, HTM Reetz GmbH, Berlin). These feature a KANTHAL heating wire and are capable of achieving temperatures up to 1273 K. The temperature is monitored using Ni-Cr/Ni thermocouples and regulated by Eurotherm controls. Usually the quartz tube was placed inside the furnace whereby the streaming argon was required; however, for annealing the sample at elevated temperatures, an encapsulated sealed quartz tube was placed inside the corundum tube in the furnace with automated central temperature control [26].

Figure 2.8.: Tube oven.

3.

Analysis Techniques

The range of the physical methods which are used to investigate the structure of compounds, as well as their physical properties is quite large, where each of the techniques exhibits its own advantages. In this chapter, the techniques, that were used for the characterization of the synthesized compounds, will be described.

3.1. X-ray Diffraction Methods

The foundation of X-ray diffraction is based on the classical phenomenon of wave interference, where parallel-monochromatic electromagnetic (EM) waves superimpose to produce a resultant wave whose amplitude is a function of the relative phases (or path difference) of the original interacting waves. The amplitude of the resultant wave increases (constructive interference) if the path difference between the interfering waves is an integer multiple of the incident wavelength; the amplitude decreases (destructive interference) if the path difference is odd-half integer multiple (1/2, 3/2, 5/2, etc.) of the incident wavelength [27, 28]. For diffraction to take place, the wavelength of the incident light has to be of the same order of magnitude as the spacing of the grating. Due to periodic ordering of atoms in the internal structure, the crystal lattice acts as a three-dimensional diffraction grating (Figure 3.1). When crystals diffract X-rays, the atoms in the lattice are becoming the secondary point sources and they scatter the X-rays. Therefore the atoms diffract the incident X-rays allowing them to form unique symmetrical reflection patterns on a detector placed in the inverted frequency or reciprocal space. The positions and the magnitudes of intensities formed on the detector are governed by the wavelength

and geometrical conditions imposed by Bragg's law (3.1):

$$n\lambda = 2dsin\theta \tag{3.1}$$

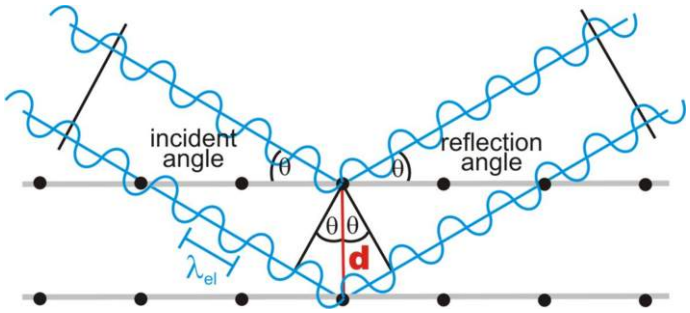

Figure 3.1.: Bragg reflection from a set of crystal planes with a spacing d.

According to Bragg's law, only certain waves incident at the angles θ_{hkl} on the fictitious atomic planes (with spacings - d_{hkl}) are going to be diffracted. The intensities (I_{hkl}) of the waves diffracted by a crystal lattice at Bragg angles (θ_{hkl}) and their corresponding (relative) phases are unique for each diffracted wave. These properties (the magnitude (I_{hkl}), direction (θ_{hkl}) and relative phases) of the diffracted waves carry information about the atomic co-ordinates, the unit cell dimensions and symmetry of the diffracting crystal. Out of the three properties, only the magnitudes (intensities) of the waves diffracted in the directions (θ_{hkl}) are directly measurable from X-ray diffraction experiments. Typically, in an X-ray diffraction experiment the diffractometer provides a long list of Bragg intensities (I_{hkl}) diffracted in the directions θ_{hkl}. A major part of X-ray crystallography is concerned with the reconstruction of the real space crystal structure of the diffracting material using a set of experimentally measured intensities (I_{hkl}) reflected in the directions θ_{hkl}, assisted by various methods that can find/assign suitable phases to the measured wave amplitudes (I_{hkl}) [27].

In an X-ray diffraction experiment, the crystalline specimen to be probed can either be of a single crystal of suitable size and quality, or of a powder consisting of small randomly oriented crystallites. Depending on the form of the crystalline sample, the observed diffraction patterns also vary. X-rays incident on a single crystal are diffracted as lines, which when obstructed by a 2D detector form well resolved spots of Bragg intensities on the detector plane (Figure 3.2). If the sample

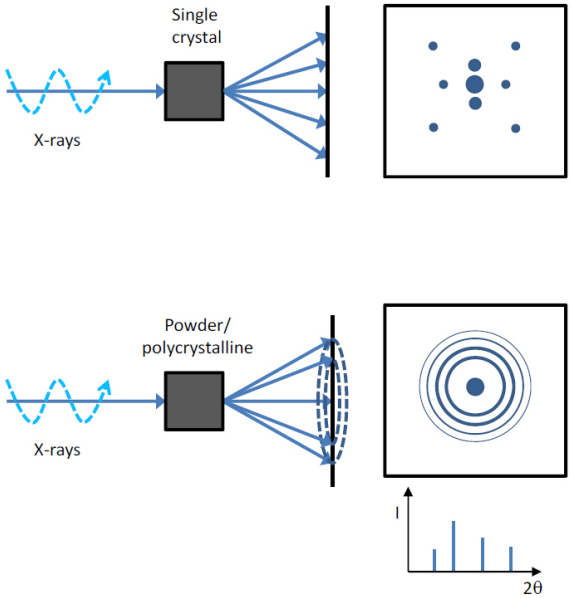

Figure 3.2.: The intensities observed (schematic) from XRD experiments performed using a single crystal and powder sample are projected in the 2D reciprocal space. Intensity spots are formed if the diffracting material is in the form of a single crystal. (Debye) Rings are formed if the diffracting material is an ideal powder.

is polycrystalline, the incident X-rays are diffracted as cones in the directions (h,k) whose projection on the 2D detector plane are confocal ellipses (Figure 3.2). As the number of small crystallites in the powder sample tends towards infinity, their orientations in space become completely random [27, 28], and the spots that constitute the elliptical base of the cones smear out to form circles (or ellipses) called Debye rings whose intensities are almost uniform.

3.1.1. Powder X-ray Analysis

Powder X-ray diffraction (XRD) was one of the most-employed techniques in this research. It was mostly used in order to ascertain the phase purity of the starting compounds as well as the products, but was also used for crystal structure determination (Rietveld analysis [29, 30]) and for defining/determing the unit cell parameters (Le-Bail fit [31]) of the examined sample.

The powder X-ray diffraction (XRD) pattern is characterized by positions, intensities and shapes of the Bragg peaks. According to the Bragg law given in equation

3.1, it can be seen that since the wavelength λ of the cathode used in experiment is known, the Bragg angles θ_{hkl} can be directly measured. Bragg angles are a discontinuous function of interplanar distances and the wavelengths, from which the d-spacing can be calculated, i.e. the unit cell dimensions. Therefore, both the unit cell dimensions and the wavelength are the two major factors that determine Bragg angle. The characteristic set of d-spacings generated in a typical X-ray scan provides a unique "fingerprint" of the investigated compound. Scattering of the powder samples gives one-dimensional projections of the reciprocal lattice, in contrast to three dimensional data of the reciprocal space in single crystal diffractometry.

Powder diffraction data has long been used as a tool for identification and characterization of crystalline materials. However, in 1967 Rietveld [29, 30] has developed a method, which has greatly enhanced the power of powder diffraction experiments. Although the crystal structure determination from powder data is much more difficult than from single crystal data, the interest for the Rietveld method is very great. This development in powder diffraction has been driven by a growing need for tools that are able to probe the structure of materials that are only available in powder form. Such materials include many zeolite catalysts, as well as certain high T_c superconductors [32]. In his approach, Rietveld proposed a method for analyzing the more complex patterns obtained from low symmetry materials by means of a curve-fitting procedure. The basic idea behind this method is the calculation of the entire powder pattern using a variety of different refinable parameters, such as structural parameters (unit cell size, atom position and occupancy factors) but also scale factors, background intensity coefficients and profile parameters describing peak shapes and widths. These parameters are then varied in a least-squares procedure until the calculated pattern best matches the observed pattern. The quantity R to be minimized is given by:

$$R = \sum w_i (I_{i0} - I_{ic})^2 \tag{3.2}$$

where I_{i0} is the observed intensity at step i, I_{ic} is the calculated intensity and w_i is a weighting assigned to each step. The stronger the observed intensity is (i.e. the smaller the counting error), the larger is w_i [33]. The graphical representation of a Rietveld refinement, shows the observed powder pattern, the best Rietveld fit profile, the position of Bragg reflection and the difference curve between observed

and calculated profiles. When the structure of an examined compound is not known or is difficult to describe, it is recommendable to use the Le Bail method [31] which is a popular method for whole pattern decomposition. Nowdays, the LeBail method is being used to refine the total envelope of a powder pattern without knowing the crystal structure and to extract the intensities which can later be used for crystal structure determination, by e.g. direct methods programs. These methods may also be used preferentially to the Rietveld method when experimental artifacts are difficult to model. These techniques are also used to obtain reflection intensity estimates as a precursor to structure solution [34]. In this work, Rietveld refinements, as well as LeBail fits were computed with the help of the program Topas [35].

Powder samples were examined by X-ray powder diffraction using an automatic powder diffractometer (STADI-P, Stoe Cie GmbH, Darmstadt, Germany) and D8 Advance (Bruker AXS GmbH, Karlsruhe, Germany) diffractometer, equipped with a molybdenum anode (MoK_α radiation $\lambda = 0.70930$ Å) for measuring samples, which contain strongly beam absorbing elements. The samples were measured using the Debye-Scherrer geometry. In addition the D8 Advance diffractometer equipped with a copper anode (CuK_α radiation $\lambda = 1.54060$ Å) was used for samples containing elements with low absorption.

The STADI-P diffractometer is equipped with a linear PSD (Position-Sensitive Detector) with a focused Ge single crystal monochromator.

The D8 Advance diffractometer is equipped with a LynxEye - Super Speed Detector, which allows to perform extremely fast measurements.

The data were calibrated with respect to an external Si-standard, regarding 2θ zero points. Recording and analysis of the powder pattern was carried out with the help of the Stoe STADI-P software [36]. The identification of the measured substances was accomplished by comparing them with known substances, the crystallographic data of which were already stored in databases (e.g. PCPDFWIN [37]) or had been manually calculated according to known literature data using the Stoe STADI-P software [36].

3.1.2. Single Crystals X-ray Analysis

Single crystal structure analysis is one of the most powerful methods of structural determination. From the single crystal X-ray data, it is possible to measure the

position and intensity of the *hkl* reflections accurately and from this data determine not only the unit cell dimensions and space group, but also the precise atomic positions.

The single crystal diffraction data were collected on a smart APEX I three circle single crystal diffractometer (Bruker AXS, Karlsruhe, Germany) equipped with a CCD detector. For the measurement pursued below 100 K, the single crystal data were collected with a smart APEX-II CCD X-ray diffractometer (Bruker AXS, Karlsruhe, Germany) with graphite-monochromated Mo-K radiation, equipped with a N-Helix low temperature device Oxford Cryosystems, Oxford, United Kingdom (28-300 K) [38]. Data collection and reduction were carried out with the Smart software package [39]. Intensities were corrected for absorption effects applying a semi-empirical method [40]. The structures were solved by direct methods and refined by full-matrix least squares fitting with SHELXTL [41].

The structure refinement includes the refinement of such parameters as: the atomic coordinates, the atomic displacement parameters (temperature parameter) as well as scale, weighting and extinction factors. The quality of the calculated structure model was evaluated according to the residual values R_1 (unweighted factor) and wR_2 (weighted factor). Both values are calculated according to equations:

$$R_1 = \frac{\sum ||F_0| - |F_c||}{\sum |F_0|} \tag{3.3}$$

$$wR_2 = \sqrt{\frac{\sum w(F_0^2 - F_c^2)^2}{\sum w(F_0^2)^2}} \tag{3.4}$$

The goodness-of-fit is calculated by equation:

$$GooF = \sqrt{\frac{\sum (F_0^2 - F_c^2)^2}{n - p}} \tag{3.5}$$

where $w = (\sigma^2 {F_0}^2 + a^2 P^2 + b^2 P^2)$ - weighting factor.

a and b are variables; n is the number of independent reflections; p is the number of refined parameters; F_0 is the measured structure amplitude; F_c is the calculated structure amplitude.

During refinement the residual values should be as small as possible while the goodness-of-fit factor should only deviate slightly from value 1 [42].

Before the accurate X-ray single-crystal structure analysis, the crystals were tested on a precession camera. A crystal has to be initially fixed and then adjusted on the precession camera goniometer in such a way that a reciprocal crystal axis is oriented parallel to the rotation axis of the camera. A constant orientation of a crystal with respect to the film plane during the precession around the X-Ray beam is achieved by a mechanical coupling. In such a way an undistorted image of the reciprocal lattice could be obtained. From this, the metric, type of lattice (integral extinction) and diffraction symbol (serial and zone extinction) of a measured compound could be definitely determined by taking several layers into account.

3.2. Energy Dispersive X-ray Spectroscopy/EDX

EDX makes use of the X-ray spectrum emitted by a solid sample bombarded with a focused beam of electrons to obtain a localized chemical analysis. All elements from atomic number 4 (Be) to 92 (U) can be detected in principle, though not all instruments are equipped for 'light' elements ($Z < 10$). Qualitative analysis involves the identification of the lines in the spectrum and is fairly straightforward owing to the simplicity of X-ray spectra. Quantitative analysis (determination of the concentrations of the elements present) entails measuring line intensities for each element in the sample and for the same elements in calibration standards of known composition. By scanning the beam in a television-like raster and displaying the intensity of a selected X-ray line, element distribution images or 'maps' can be produced. Also, images produced by electrons collected from the sample reveal surface topography or mean atomic number differences according to the mode selected. The scanning electron microscope (SEM), which is closely related to the electron probe, is designed primarily for producing electron images, but can also be used for element mapping, and even point analysis, if an X-ray spectrometer is added. There is thus a considerable overlap in the functions of these instruments.

The chemical composition was determined using a scanning electron microscope (XL30 TMP, Philips, Holland, tungsten electrode, 25 kV), equipped with an integrated EDAX-EDX system (EDX = Energy Dispersive X-Ray Analysis; EDAX, Wiesbaden, Germany) and with a S-UTW-Si(Li)-detector (S-UTW = Super Ultra Thin Window, polymer window, active detector surface 10 mm^2). The self-

absorption of this detector allows the detection of elements with an atomic number Z of more than 5, which corresponds to Bor. The qualitative as well as quantitative analysis of the energy spectra (resolution $<$ 135 eV for Mn-Kα 1000 cps and 65 eV for C) was carried out with the program system Phoenix (EDAX, Wiesbaden, Germany). The air sensitive samples were prepared in a glove box and transferred under argon to the electron microscope using special a transfer chamber.

3.3. Chemical Elemental Analysis

Inductively coupled plasma with optical emission spectroscopy (ICP-OES) is a method for elemental analysis. A high-frequency current (typically 27 or 41 MHz) is sent through a coil, generating a magnetic field. Plasma is then formed from the gas (argon) flowing through the coil. In the plasma, the same number of Ar^+ and electrons coexist, maintaining the charge balance. The argon plasma reaches a temperature of 6000 to 8000 K. When the sample, in the form of fine aerosol, is introduced into the plasma via a carrier gas, nearly all of the elements in the sample become highly excited by the energy from the plasma and begin emitting light. Each element emits light with a wave length (spectrum) specific to that element (usually in the range 165 800 nm). It is, therefore, possible to analyze and identify the elements in the test sample by separating the emitted light into its spectral components using a high-performance spectrometer. The emission intensity for each element is monitored for each standard solution and a calibration curve of emission intensity versus element concentration can be constructed. The analyses in this work were performed with the help of Vista-Pro (Simultaneous ICP-OES, CCD detector, with axial plasma, Varian). The digestion of the samples was performed using a Berghof-Pressure- System with PTFE coating.

3.4. Thermal Analysis

As the name implies, thermal analysis is the measurement of chemical and physical properties of a substance as a function of temperature. In this work thermogravimetric analysis (TGA), differential thermal analysis (DTA), and differential scanning calorimetry (DSC) were employed to study the phase transitions and respective

decomposition temperature of the substance of interest. The registration of thermal activities using DTA and TGA were performed simultaneously on the STA 429 thermal analysis device (Netzsch GmbH, Selb, Germany). Differential Scanning Calorimetry (DSC) was performed with a computed-controlled DSC sensor (DSC 404 C Pegasus, Netzsch GmbH, Selb, Germany) equipped with a Pt10%Rh-Pt thermoelement (type S). As a sample holder the cylindrical form corundum or alumina were used. The samples were weighed in a glove box and transported in Schlenk apparatures directly to the thermal devices. The whole process took place under argon.

3.5. Specific Heat Measurements

Specific heat as a function of temperature of a polycrystalline sample of almost all the mentioned compounds were measured between 2 and 350 K using a commercial PPMS (Physical Property Measurement System, Quantum Design, 6325 Lusk Boulevard, San Diego, CA.) employing the relaxation method [43, 44]. To thermally fix the sample tablet ($\oslash = 5$ mm and thickness 1mm) to the sapphire sample platform, Apiezon N vacuum grease was used. The heat capacity of the sample holder platform and the grease were individually determined in a separate run and subtracted from the total measured heat capacities.

3.6. EPR Spectroscopy

Electron paramagnetic resonance spectroscopy is a technique employed for studies of paramagnetic substances, whose properties can be explained by considering the behavior of a free electron. An electron has a spin which can be understood as an "angular momentum" leading to a magnetic moment. Consequently, the negative charge that electron carries is also spinning and makes a circulating electric current, inducing a magnetic moment μ_S [45]. When the electron is being subjected to a magnetic field $\mathbf{H}_0$, it experiences a torque tending to align the magnetic moment with the field. The relation between the magnetic moment and the spin vector is:

$$\mu_S = -\frac{g\mu_B}{\hbar} S \tag{3.6}$$

where μ_B is the Bohr magneton and g is the Landé factor. The energy of the system depends upon the projection of the spin vector along $\mathbf{H}_0$, where the electron magnetic moment can only assume two projections onto the applied field leading consequently to:

$$\mu_z = \pm\frac{1}{2}g\mu_B \tag{3.7}$$

and the ensemble of energy levels therefore reduce to the two values:

$$E_\pm = \pm\frac{1}{2}g\mu_B H_0 \tag{3.8}$$

If the electromagnetic radiation is applied at a frequency that corresponds to the separation between the permitted energies equal to $\triangle E$=E_+-E_-=$g\mu_B H_0$=$\hbar\omega$, energy is absorbed from the electromagnetic field. This is the phenomenon of EPR.

For electrons bound into an atom or a molecule, the phenomenon of EPR may not be observed at all, because electron spins pair up in atomic or molecular orbitals so that virtually no net spin magnetism is exhibited and the material is said to be diamagnetic. When an atom or a molecule has an odd number of electrons, however, complete pairing is clearly not possible and the material is said to be paramagnetic. In that case EPR can be observed.

Electron paramagnetic resonance (EPR) was measured with a Bruker ER040XK microwave X-band spectrometer and a Bruker BE25 magnet equipped with a BH15 field controller, which was calibrated against Diphenylpicrylhydrazyl.

3.7. Magnetic Measurements

The temperature dependent magnetic susceptibility (χ) of the samples was measured using a SQUID magnetometer (Superconducting Quantum Interference Device, MPMS 5.5, Fa., Quantum Design, USA). The magnetometer allows to perform investigations in the temperature range 1.7 - 300 K in a homogeneous magnetic field up to 7 T. The specimen that had been ground into a powder was put into a gelatin capsule or sealed in a high purity synthetic fused silica (SUPRASILR) tube under helium. The magnetization was corrected for the holder contribution. The values of diamagnetic core corrections [46] were evaluated for all compounds.

The plot χ^{-1} versus temperature gives an informative view about the magnetic

behavior of a given sample, especially if χ^{-1} grows linearly with increase of temperature.The magnetic susceptibility behavior of measured samples was evaluated by via the *Curie Weiss* law:

$$\chi_{mol} = \frac{C}{T - \theta} \tag{3.9}$$

where χ_{mol} is the magnetic susceptibility of the compound; C is the Curie constant; T is absolute temperature(K); and θ the Weiss constant (K), respectively. The Curie constant can be computed according to the expression:

$$C = \frac{\mu_0 N_a \mu^2}{3k_B} \tag{3.10}$$

where μ_0 is the magnetic constant (μ_0= 1 in CGS unit system); N_A the Avogadro constant; k_B the Boltzmanns constant; and μ the magnetic moment (1.73 μ_B for a single electron with spin quantum number S = 1/2; μ_B is the Bohr magneton, respectively.

4.

Starting Compounds

In order to undertake the physical characterization of the new synthesized products in a proper manner, it is of great importance that they are obtained in the phase pure form. In addition to the fact that the synthesis should proceed under strictly inert conditions, it is also of great importance to use starting materials of high purity, whose quality is constantly being controlled by X-ray powder diffraction.

4.1. Alkali Azides

The phase pure starting materials LiN_3, KN_3, RbN_3 and CsN_3 were prepared via distillation of hydrazoic acid. HN_3 is a colorless and toxic liquid which should be handled with great caution. It is produced by reaction of an aqueous solution of NaN_3 (99.5 %, Sigma) with drops of 20 % H_2SO_4 (99.9 %, Merck) in a flask as shown schematically in Figure 4.1. Up to $\sim$ 20 g of NaN_3 was dissolved in water and transferred in 500 ml flask fitted with dropping funnel and a Liebig condenser. Firstly, the solution is heated (close to $\sim$ 320–330 K), and afterwards H_2SO_4 is added dropwise. It is important to add the acid in to the already heated solution, as otherwise concentrated hydrazoic acid vapors build up in the reaction flask and can cause an explosion [47].

The distillate is condensed in the flask containing the appropriate alkali carbonate. The whole process can be summarized with the following reaction equations:

$$2NaN_3 + H_2SO_4 \rightarrow Na_2SO_4 + 2HN_3 \tag{4.1}$$

$$2HN_3 + A_2CO_3 \rightarrow 2AN_3 + H_2O + CO_2 \quad (A = \mathrm{Li, K, Rb, Cs}) \tag{4.2}$$

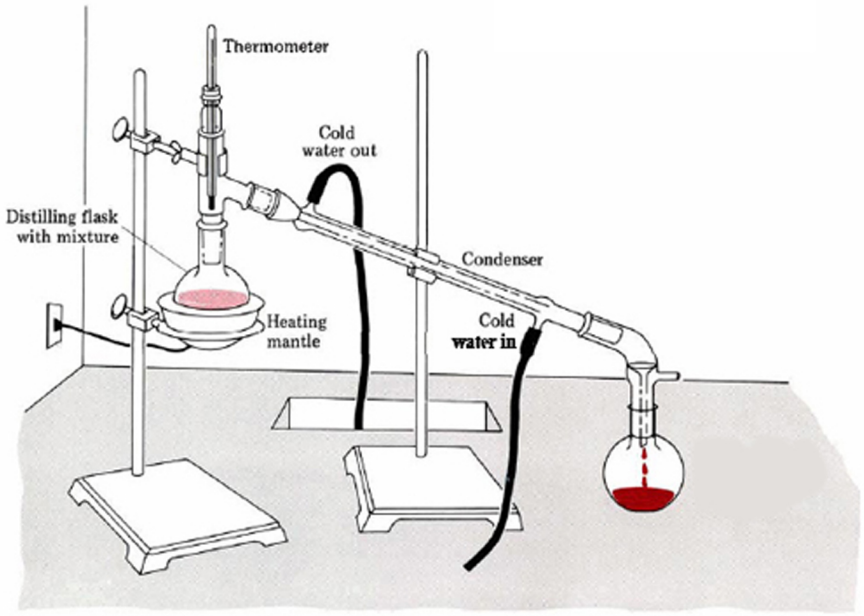

Figure 4.1.: Synthesis of HN_3.

Completeness of reaction 4.2 can be observed through the absence of CO_2 bubbles formation, which can also be simultaneously controlled via the pH of the solution (pH = 5-6). After the reaction is complete, the distillate, containing appropriate alkali azide, is let to dry on 350 K on a sand bath in the fume hood. Next, the solid residue is ground, transferred into the schlenk line, dried under vacuum overnight at 373 K, and stored in the Glove box.

The whole drying procedure cannot be applied to LiN_3. The reason is, that it tends to decompose close to 388 K [47]. The drying of LiN_3 can be achieved under vacuum in a specially designed assembly called "Trockenpistole" [26], which contains also P_4O_{10} as the drying agent. The XRD diffraction confirmed that phase pure LiN_3 can also be obtained by transferring it to the Schlenck apparatus and dry; at room temperature under vacuum overnight.

The phase purity of synthesized alkali metal azides was constantly controlled with the X-ray powder diffraction (Figures 4.2- 4.5).

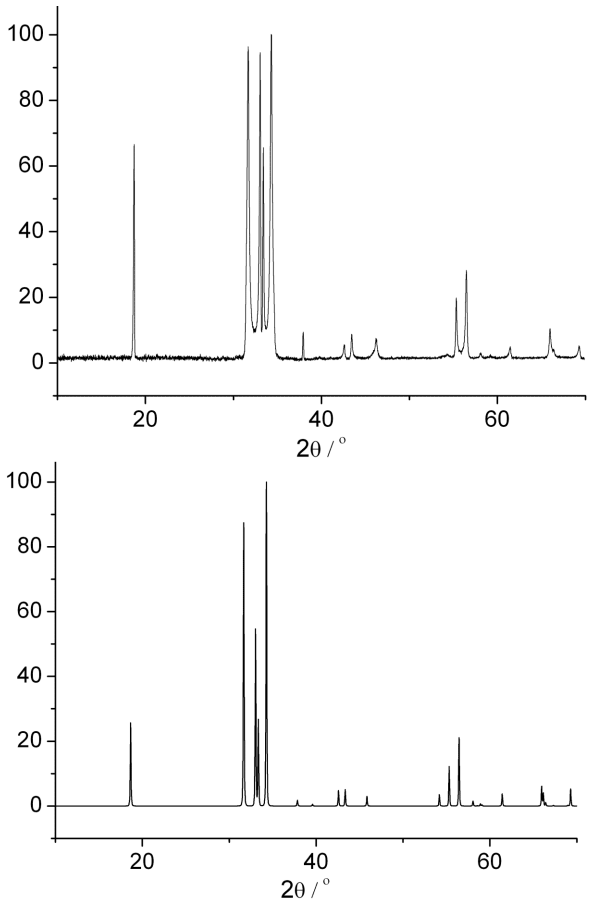

Figure 4.2.: Theoretical and experimental XRD pattern for LiN_3.

4.2. Potassium Oxide, K_2O

The preparation of potassium oxide, K_2O was performed from the reaction of elementary alkali metals with a stoichiometric amount of oxygen [48]:

$$2K + O_2 \rightarrow K_2O \tag{4.3}$$

Firstly, potassium metal was distilled twice and sealed in glass ampoules under argon. It was weighed by the difference method and put into the reaction vessel which had been connected to the vacuum line through a gas dosimeter. Afterwards, the whole setup was evacuated and the required amount of oxygen was introduced in small portions through the gas dosimeter to the alkali metal. However, initially the reaction product consisted of a mixture of non reacted potassium metal, potassium

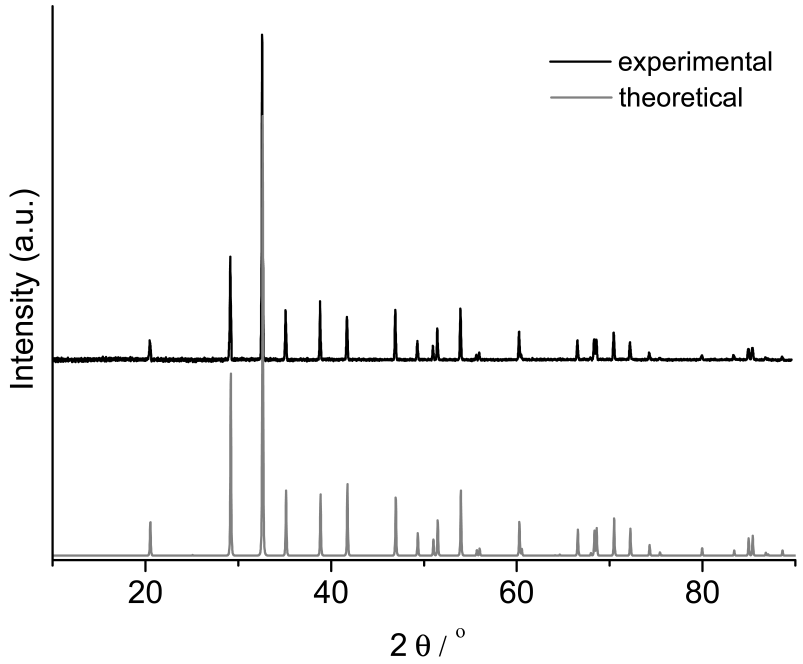

Figure 4.3.: Theoretical and experimental XRD pattern for KN_3.

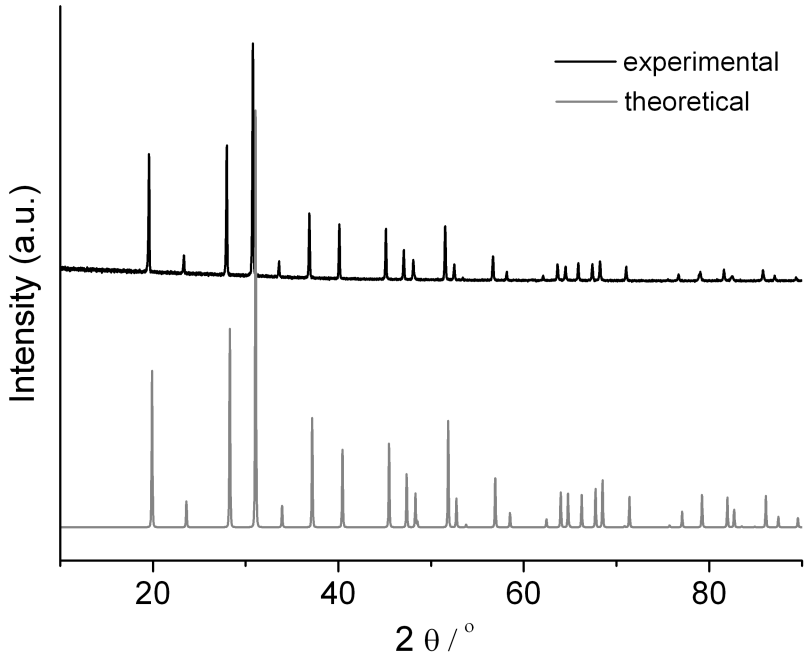

Figure 4.4.: Theoretical and experimental XRD pattern for RbN_3.

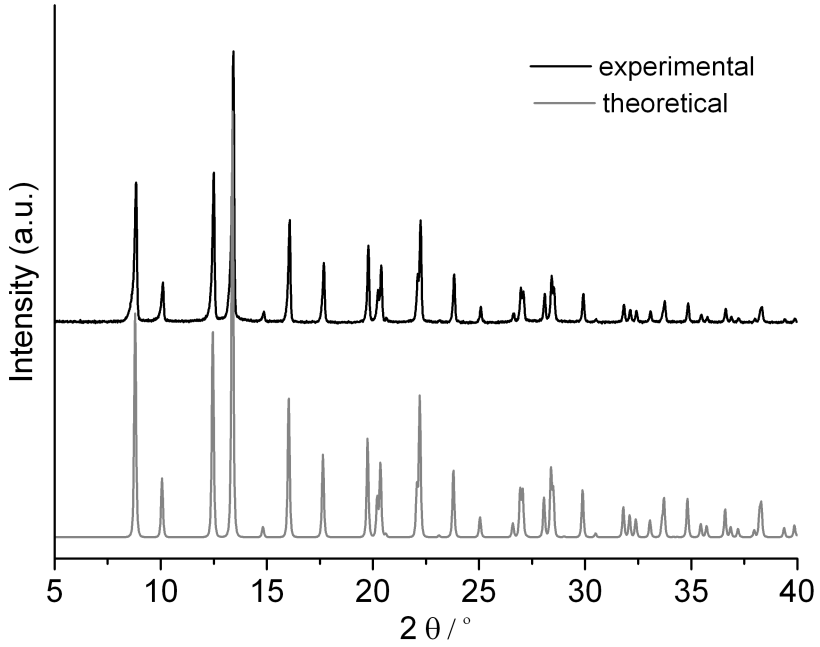

Figure 4.5.: Theoretical and experimental XRD pattern for CsN_3.

oxide, peroxide and hyperoxide. Therefore, to homogenize the end product and to produce the potassium oxide as a single phase the system was heated up to 523 K during 1-2 days, several times. Finally, the excess of alkali metal was distilled off. The purity of potassium oxide was controlled by the X-ray powder diffraction method (Figure 4.6).

.

4.3. Transition Metal Oxides

In order to increase the chemical activity of the starting compounds (small crystal size), transition metal oxides were synthesized in the laboratory. Due to high specific surface area, transition metal oxides, prepared in this way, possess high chemical activity which influences the kinetics of the reaction.

4.3.1. Nickel Oxide, NiO

Nickel oxide with high specific surface area was prepared from the thermal decomposition of $NiC_2O_4 \cdot 2\,H_2O$ in a corundum crucible under oxygen stream.

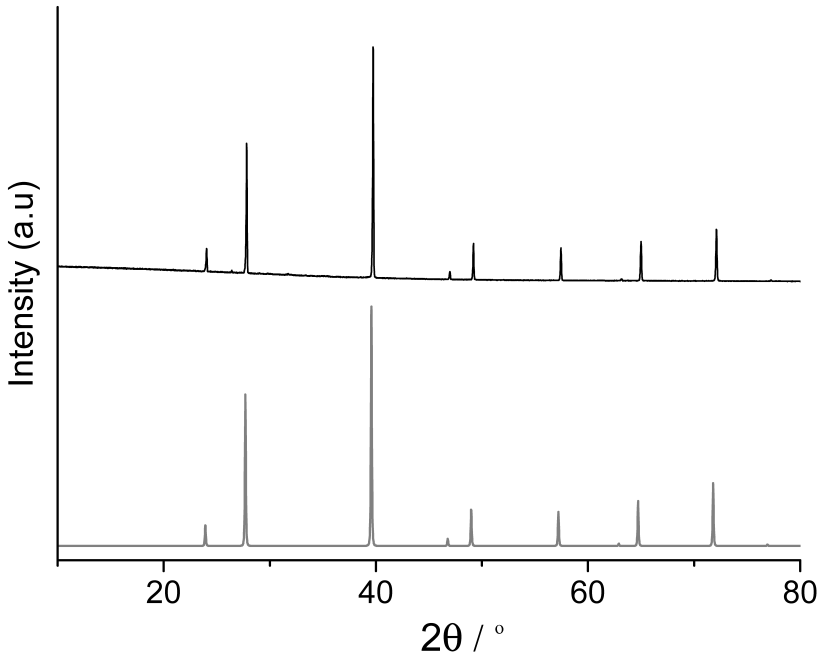

Figure 4.6.: Theoretical and experimental XRD pattern for K_2O.

$NiC_2O_4 \cdot 2\,H_2O$ was prepared by precipitation of $Ni(NO_3)_2$ with $H_2C_2O_4$. For the decomposition of nickel oxalate, the following temperature treatment was applied: 423 K $\rightarrow$ 623 K (heating rate 5 K/h); annealing at 623 K for 20 h and subsequent cooling down to room temperature. From the XRD powder data of NiO (Figure 4.7) it can be seen that the sample is nanocrystalline.

4.3.2. Copper Oxide, CuO

Chemically active CuO was prepared from $CuC_2O_4 \cdot 2\,H_2O$ by thermal decomposition in a corundum crucible under oxygen stream. The following temperature treatment was applied: 423 K $\rightarrow$ 623 K (heating rate 5 K/h); annealing at 623 K for 20 h and subsequent cooling down to room temperature, and cooling down to room temperature. X-ray powder data of CuO are presented in Figure 4.8.

.

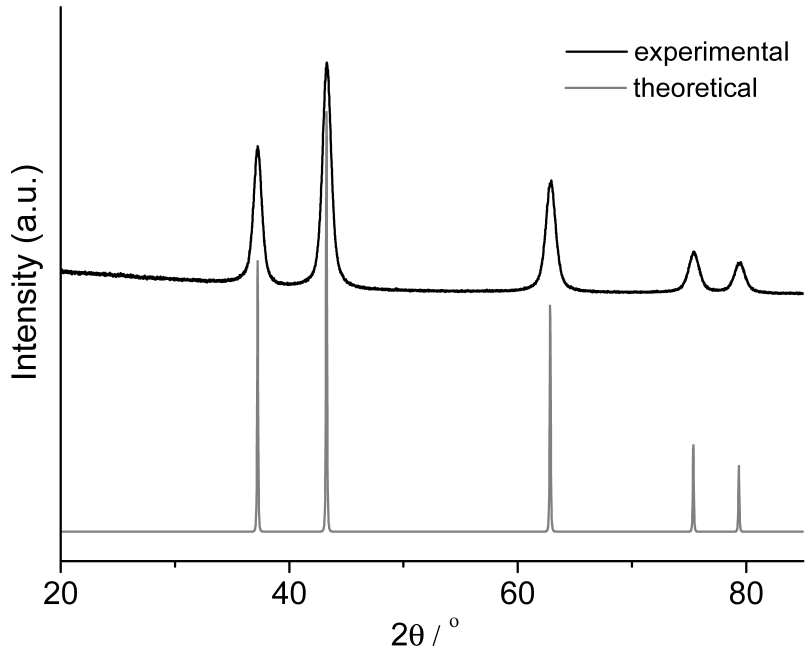

Figure 4.7.: Theoretical and experimental XRD pattern for NiO.

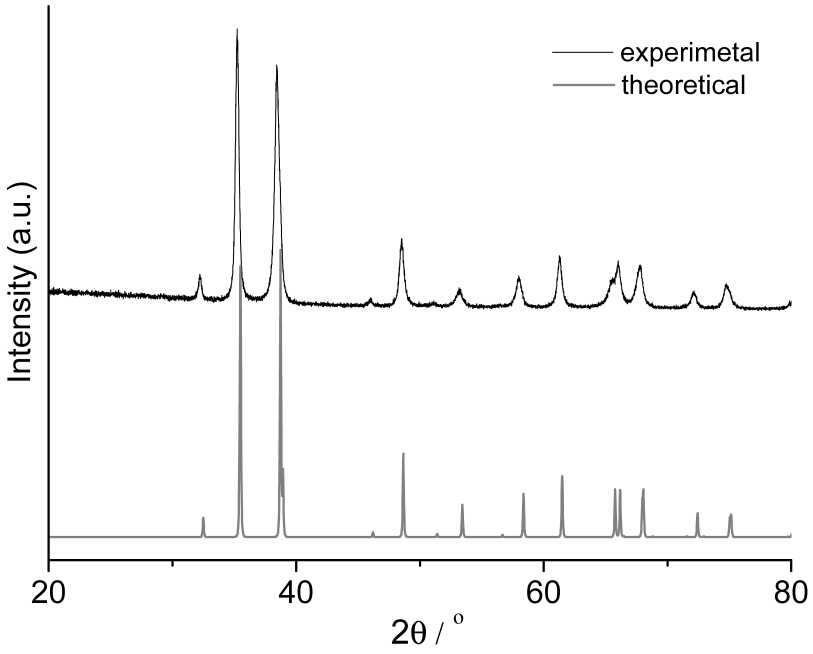

Figure 4.8.: Theoretical and experimental XRD pattern for CuO.

Part III.

Special Part

Ternary transition metal oxides are one of the most exciting areas of research in solid state chemistry and materials science today. One of the main reasons for this is that transition metals exhibit a wide range of oxidation states as well as coordination numbers, which results in the formation of a large variety of structures, exhibiting very interesting physical properties. The coordination number in transition metal oxides is usually four or six with approximately tetrahedral/tetragonal or octahedral geometries. Distortions from ideal geometries are usually associated with the steric activity of the metal *d*-electrons, most typically due to the Jahn-Teller effect, or with metal-metal bonding. Larger distortions are found in certain complexes of d^0 metal ions. A straightforward assumption is that the high oxidation states of transition metal atoms in compounds are stabilized via coordination by a larger number of highly electronegative elements [49], like in $KMnO_4$ [50], K_2FeO_4 [14], Cs_2CuF_6 [51]. Nevertheless, if it were possible to lower the coordination number of the transition metal and at the same time to compensate the negative charge of the ligands by additional cations, a whole series of middle and lower oxidation states of the transition metal could be obtained.

A large number of compounds of general formula A_xMO_2 containing linear, or almost linear $[MO_2]^{x-}$ dumbbells (M any transition metal; $x = 2$ or 3) have been synthesized and characterized by the method of single crystal X-ray analysis [1, 15, 52–56]. These dumbbells contain usually equidistant M–O lengths. However, in some asymmetric crystal fields the O–M–O dumbbells can be distorted, like for example, the two Cu–O distances in compounds like KNa_2CuO_2 are 173.1 ± 3.0 and 182.4 ± 3.4 pm [57]. The only linear transition metal complexes that have been known and investigated before are transition metal dihalides [58], studied either in the gas phase or isolated in a noble gas matrix. With the discovery of new A_2MO_2 and A_3MO_2 compounds [15, 53–56] in the 1980' years, a new field was opened for investigating structural properties.

In this chapter we extend this field by investigating new members of these compound families and elaborating the phase transitions they exhibit.

5.

Synthesis and Characterization of A_3NiO_2 (A = K, Rb, Cs) Family of Compounds

The A_3MO_2 family of alkali-metal oxometalates include similar or even isotypic structures, which may be regarded as stuffed KrF_2 structures [59]. The crystal structure determinations of A_3MO_2 compounds reported so far are of high quality throughout. However, common for some of the tetragonal variants (K_3NiO_2, K_3FeO_2 [15]) is that there exists a striking anomaly in the coefficients of the thermal displacement parameters for only one of the alkali ions' positions, while all other parameters are quite regular. In the special cases of K_3NiO_2 and K_3FeO_2 the enantiomorphic space groups $P4_32_12$ and $P4_12_12$, and their supergroup $P4_2/mnm$ are involved. Possible reasons for the systematic anomalies might be related to twinning caused by phase transitions, or even to an inappropriate space group symmetry applied [60].

In order to settle the apparent inconsistencies, concerning the anomalies related of increased anisotropic parameters for one of the potassium ion, we re-investigated K_3NiO_2, and refined its crystal structure from single crystal data collected at temperatures below and above ambient conditions. Also, in this chapter the synthesis and the structure data for new compounds A_3NiO_2 (A = Rb, Cs) are reported, where it was found that Rb_3NiO_2 crystallizes isostructurally in the $P4_12_12$ space group. Structure determinations of Rb_3NiO_2 and Cs_3NiO_2 were performed from the X-ray powder data by the Rietveld refinement.

Significance of the Ni(I) Oxidation State

Alkali-metal oxonickelates, of general formula A_3NiO_2 (A = K, Rb, Cs) are especially interesting due to presence of the low oxidation state of nickel Ni(I). This oxidation state of nickel occurs quite rare in the compounds and cannot be easily stabilized. The first discovery related to the presence of the Ni(I) ions in any compound was found in the complex $K_2[Ni_2(CN)_6]$ (dNi–Ni = 2.32 $\AA$). This red diamagnetic compound was obtained by adding the NH_3 to the solution of $K_2[Ni(CN)_6]$ [61].

First evidence related to the presence of a Ni(I) ion in the solid state systems was reported in 1983 [62, 63]. The authors identified $LaNiO_2$ containing formally Ni(I), and its layered structure was described by the stacking sequence of $NiO_2{}^{3-}$–La^{3+}–$NiO_2{}^{3-}$– La^{3+}. Such compounds gained additional interest after the discovery of superconductivity in cuprates, which led to many other transition metals systems being investigated for superconductivity, where among others the nickelates were also suggested to have the potential to exhibit physics similar to the cuprates. Theoretical studies have shown that only nickelates with Ni(I) (d^9, S = 1/2) in a square planar coordination can form an antiferromagnetic insulator directly analogous to the parent undoped cuprates [64]. The Ni(I)/Ni(II) states of nickelates have identical ($3d^9/3d^8$) electronic configuration as Cu(II)/Cu(III) in the high temperature superconducting cuprates, and are expected to show interesting properties. Several new phases involving Ni(I) in an ordered defect K_2NiF_4- type structure were obtained: $La_{1.6}Sr_{0.4}NiO_{3.47}$, $LaSrNiO_{3.5}$, $LaSrNiO_{3.1}$ [65, 66], as well as new compounds with the basic structural feature of infinite NiO_2 layers; $La_3Ni_2O_6$ [67], $Ln_4Ni_3O_8$ (Ln = La, Nd) [68]. Although the crystal chemistry of lanthanum nickelates is strongly related to the corresponding cuprates, especially those of composition $La_{2-x}Sr_xCuO_4$ which exhibit high temperature superconductivity, there are no reports that these compounds exhibit this property.

Further manifestation of the Ni(I) ion in solid state systems was found in the alkali-metal oxometalates(I) [15]. Originally, oxometalates(I) were expected to exist only for Groups 11 (Ib) and 13 (IIIa) metals, as reported in 1958 [69]. These compound are remarkable not just due to the low coordination of the transition metal, but also due to its low oxidation state (CsAuO [70], KAgO, CsAgO [71], KCuO [72, 73]). Further research resulted in the synthesis of a new series of compounds containing the Ib elements, which can be represented by the general formula

A_3MO_2 (Na_3AgO_2 [74], K_3CuO_2 [53], Na_3AuO_2 [55], Rb_3CuO_2 [56]). In 1993, the synthesis of new alkali-metal oxometalates(I) containing Ni(I), Co(I) and Fe(I) was reported (K_3NiO_2, K_3FeO_2 [15], K_3CoO_2, Na_3CoO_2, KNa_2NiO_2, $RbNa_2NiO_2$ [75]). The +1 oxidation state of the nickel ion in $[NiO_2]^{3-}$ is unusually low for a metal oxide. More typically the π-donor property and electronegativity of oxygen is used to stabilize the higher oxidation states of nickel and other elements, making these compounds interesting in terms of electronic structure and physical properties. Crystallographic data revealed that this 'linear' $[O–Ni–O]^{3-}$ anion is slightly bent away from linearity (175° at KNa_2NiO_2, and 179.9° for K_3NiO_2). The electronic and magnetic properties (EPR spectroscopy) of these nearly linear complexes were investigated by several authors [76,77]. However, the magnetic susceptibility characterization of this type of compounds is lacking until now. In this chapter, except the structural characterization of alkali-metal oxonickelates(I) (A_3NiO_2 (A = K, Rb, Cs), the magnetic susceptibility data are reported for the first time for this type of compounds.

Parts of this chapter are included in the publications "K_3NiO_2 Revisited, Phase Transition and Crystal Structure Refinement" [60] and "Syntheses, structures and magnetic properties of the alkali-metal oxonickelates(I) A_3NiO_2 (A = K, Rb, Cs)" [78].

5.1. Synthesis, Crystal Structure, Phase Transition and Magnetic Properties of K_3NiO_2

5.1.1. Synthesis and Thermal Analysis

K_3NiO_2 was synthesized from KNO_3 (Alfa Aesar, 99,8 %) and potassium azide, which was prepared from aqueous HN_3 and potassium carbonate (Fluka, 99 %). The synthesis of nickel oxide, NiO has been described in chapter 4.3.1. The starting compounds were dried under vacuum (10^{-3} mbar) at 393 K overnight, mixed thoroughly in an agate mortar in a ratio according to equation 5.1, and placed under argon in a closed steel container, provided with a silver inlay.

$$8KN_3 + KNO_3 + 3NiO \rightarrow 3K_3NiO_2 + \frac{25}{2}N_2 \tag{5.1}$$

In the reaction, a small excess of azide was used (0.5 mol excess of KN_3). Dark

red powders as well as single crystals of K_3NiO_2 were obtained in a flow of argon when the following temperature treatment was applied: 298 → 533 K (100 K/h) 533 → 653 K (5 K/h), 653 → 873 K (100 K/h), and subsequent annealing for 50 h at 873 K.

The single crystals obtained, as well as the powders, because of their sensitivity to air and moisture, were sealed in glass ampoules in an argon atmosphere. All further manipulations were performed in an inert atmosphere of purified argon.

The thermal analysis of K_3NiO_2 (Figure 5.1) revealed that the product is thermally stable up to ∼ 900 K.

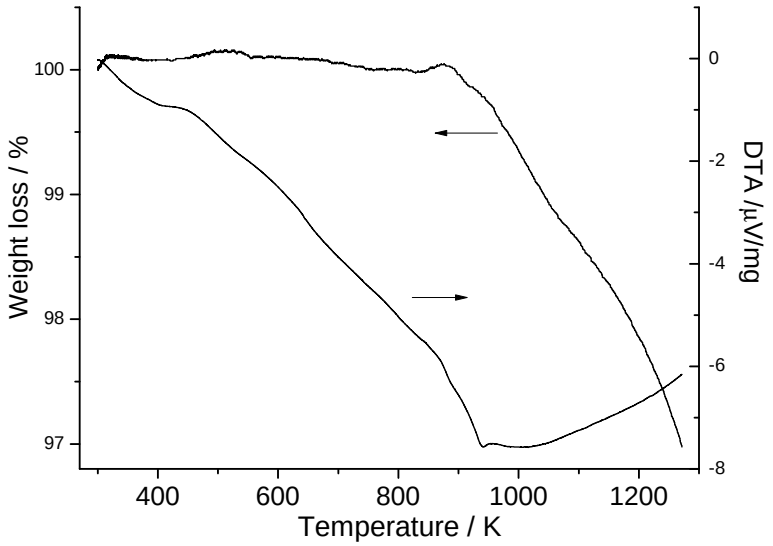

Figure 5.1.: Thermal analysis of K_3NiO_2.

5.1.2. Group Theoretical Classification of K_3NiO_2 and Related Crystal Structures

As already mentioned, K_3NiO_2 crystallizes tetragonal in the $P4_12_12$ space group [15] (more detailed structural characterization will be given in sections 5.1.3 and 5.1.4). However, this compound exhibits increased values of anisotropic parameters for one of the potassium ions. A possible cause for this may be related to the use of space group symmetries applied during the phase transitions at elevated

temperatures. If a substance forms several polymorphic forms, and at first a high-temperature form is obtained, than subsequent cooling may result in unnoticed phase transition with symmetry reduction. If the high- and low-temperature structure can be related via translationsgleiche group-subgroup relation, that could lead to formation of a twinned crystal [79]. To determine what the these assumptions are, firstly it was necessary to analyze the possible implications on the basis of group-subgroup relations among the space groups involved $P4_12_12$, the space group which is suggested for α-K_3NiO_2. This implies the existence of another enantiomorph in space group $P4_32_12$, as well as the possibility of racemic twins and of a polymorph in a non-enantiomorphic supergroup.

Indeed, taking a closer look at the reciprocal layer of $hk0$ α-K_3NiO_2 the presence of systematic extinctions that do not comply with any space group (all $0kl$ absent, when $k = 2n$, $l = 4n + 2$, and $k = 2n + 1$, $l = 4n$) might indicate the crystal investigated to be twinned [60].

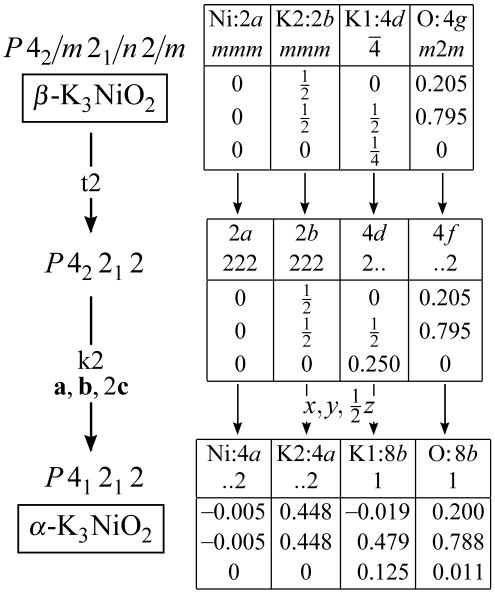

Ni:2*a*	K2:2*b*	K1:4*d*	O:4*g*
mmm	*mmm*	$\bar{4}$	*m*2*m*
0	$\frac{1}{2}$	0	0.205
0	$\frac{1}{2}$	$\frac{1}{2}$	0.795
0	0	$\frac{1}{4}$	0

2*a*	2*b*	4*d*	4*f*
222	222	2..	..2
0	$\frac{1}{2}$	0	0.205
0	$\frac{1}{2}$	$\frac{1}{2}$	0.795
0	0	0.250	0

Ni:4*a*	K2:4*a*	K1:8*b*	O:8*b*
..2	..2	1	1
–0.005	0.448	–0.019	0.200
–0.005	0.448	0.479	0.788
0	0	0.125	0.011

Figure 5.2.: Group-subgroup relation between α-K_3NiO_2 and β-K_3NiO_2, (Bärnighausen-tree). (The atomic coordinates of isotypic α-Li_3BN_2 are nearly the same as for α-K_3NiO_2, with the origin shifted for 1/2, 1/2, 1/2 in comparison to published data).

However, it was essentially impossible to identify a rational twin law. When considering the possible supergroups, in particular $P4_2/mnm$, it is obvious that the extinctions mentioned fit to this space group with the length of the original

c-axis divided by two. Indeed, such a group-subgroup relationship can be substantiated by real compounds: Li_3BN_2 crystallizing in $P4_2/mnm$ and α-K_3NiO_2 in $P4_12_12/P4_32_12$. The respective Bärnighausen tree is displayed in Figure 5.2. Remarkably, for none of the space groups included in Figure 5.2 there are subgroups or supergroups that might explain the enlarged thermal expansion parameters U_{33} and U_{12} for K2 without assuming dynamic disorder.

From these considerations, a straightforward research plan was designed to follow up on the analysis of the strange features associated with K2. Firstly, it was necessary to to check whether the crystals of K_3NiO_2 are racemic twins at ambient conditions. Secondly, one had to trace possible phase transitions above and below ambient temperatures, and finally, the changes of the coefficients of thermal motion upon lowering the temperature had to be monitored. All of these details are described in the following sections.

5.1.3. Phase Transition

α-K_3NiO_2 crystallizes in the tetragonal space group $P4_12_12$. In-situ temperature dependent X-ray powder diffraction revealed that α-K_3NiO_2 is stable below approx. 410 K, where it exhibits a phase transition to β-K_3NiO_2.

Experimental and calculated XRD patterns of α-K_3NiO_2 (at 298 K) and β-K_3NiO_2 (at 483 K) are given in Figure 5.3, and the parameters related to the Rietveld refinements in Table 5.1. The observed phase transition follows the expectations which were analyzed according to the group-subgroup relations as discussed previously in the section 5.1.2, where the transformation is accompanied with a change of the c-axis of α-K_3NiO_2 to almost half of its value as for β-K_3NiO_2. The lattice parameter c of α-K_3NiO_2 shows a significant thermal expansion (approx. 3 %) from 13.77 Å at 50 K to 14.157 Å at 403 K (Figure 5.4), while the a parameter stays virtually unchanged. At the phase transition, the unit cell volume changes discontinuously from $V(\alpha) = 514.4$ Å^3 to $2V(\alpha) = 515.6$ Å^3 ($V(\alpha) = 257.8$ Å^3 at 423 K). The marked temperature range 400–423 K in Figure 5.4, indicates coexistence of both phases and thus a significant hysteresis.

The volume discontinuity and the hysteresis point to a first order phase transition.

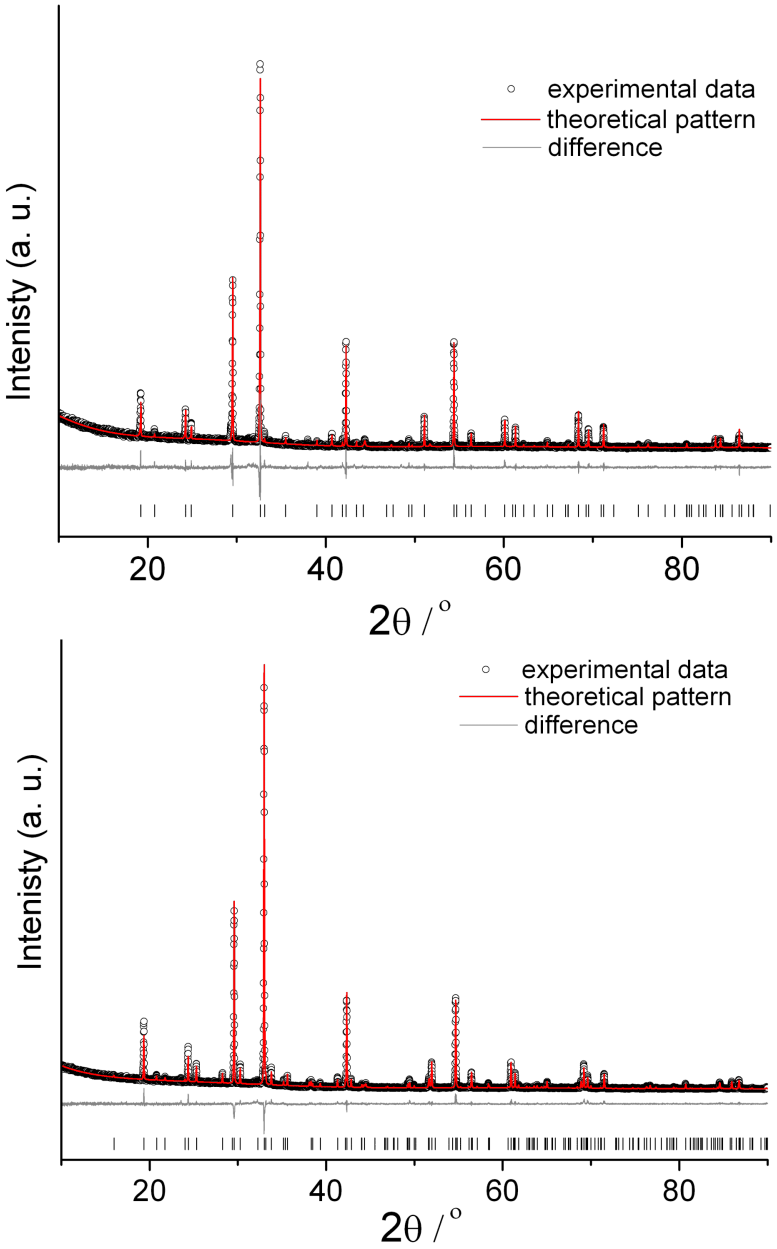

Figure 5.3.: Experimental and calculated XRD patterns for α-K_3NiO_2 (lower picture) and β-K_3NiO_2 (upper picture). Black marks experimental, red calculated profile. The difference between the experimental and theoretical patterns is given in grey. Bragg positions are given by tick marks.

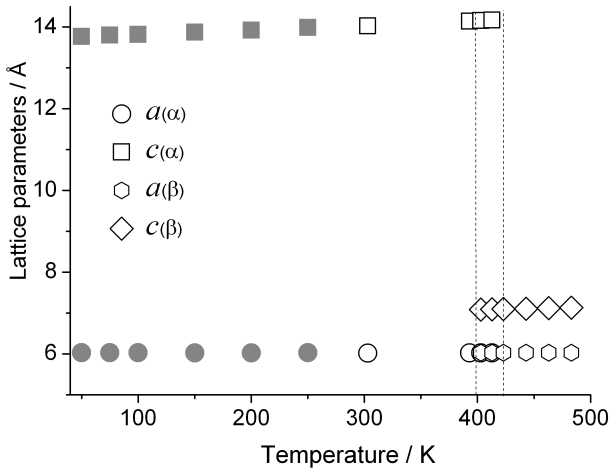

Figure 5.4.: Temperature dependence of the unit cell parameters of K_3NiO_2 obtained from Rietveld refinements (open circles) and single crystal analyses (grey marks).

Table 5.1.: Crystallographic data for K_3NiO_2 (obtained by Rietveld refinement) at temperatures of 303 K and 483 K.

	α-K_3NiO_2	β-K_3NiO_2
Space Group, Z	$P4_12_12$ (No.92), 4	$P4_2/mnm$ (No. 136), 2
Temperature/K	303(5)	483(5)
Cell parameters/Å	a = 6.0337(1) Å	a = 6.0436(1) Å
	c = 14.0623(1) Å	c = 7.1485(2) Å
Cell Volume/Å^3	511.94	261.09
Crystal density/g/cm^3	2.70	2.65
Wavelength/Å	1.540598	1.540598
Range data collection ($2\theta/^o$	10–90	10–90
Time range for data collection/h	36	36
R_{Bragg}/%	7.30	4.13
R_p/%	6.63	6.27
R_{wp}/%	8.77	9.24

5.1.4. Crystal Structures of the Low-Temperature (α-K_3NiO_2) and High Temperature Modifications (β-K_3NiO_2)

The crystal structure determinations and refinements were performed on X-ray single crystal data collected at 50, 100 and 298 K (α-K_3NiO_2) and 500 K (β-K_3NiO_2). Details of the single crystal solutions are given in Table 5.2, Table 5.3, and Table 5.4 (for α-K_3NiO_2). Table 5.5, Table 5.6, and Table 5.7 contain the corresponding

results, collected at 500K, for β-K_3NiO_2. Interatomic distances and coordination numbers (CN) can be found in Table 5.8.

Crystal structure data for the low-temperature form α-K_3NiO_2, are in good agreement with the previously published results [15]. The initial refinement in the space group $P4_12_12$ resulted in a Flack parameter of 0.53(5) [80]. This was strong evidence for the presence of a racemic twin ($P4_12_12/P4_32_12$) with approximately the same portions of both enantiomorphic forms. Refinement as a racemic twin actually resulted in an improvement of the residual value from $R_1 = 0.043$ to $R_1 = 0.032$. During the transition to β-K_3NiO_2 only small displacements of the atoms are noticed, where the oxygen atoms shift from the general position $8b$ of $P4_12_12$ to the special position $4g$ of the space group $P4_2/mnm$, with $m2m$ site symmetry.

Like the nickel and K2 atoms, the oxygen atoms now occupy positions on a twofold rotation axis, along the diagonal in the ab plane. The nickel, oxygen and K2 atoms in β-K_3NiO_2 thus are arranged in linear chains. These consist of O–Ni–O dumbbells, separated by K2 atoms (Figure 5.5). The short Ni–O distance of 176 pm indicates the formation of a complex NiO_2^{3-} anion. The orientation of the chains alternates between the [110] and [$\bar{1}$10] directions, along the c axis. The space group $P4_2/mnm$, which we found for the high temperature form β-K_3NiO_2, is one of the supergroups of $P4_12_12$ and $P4_32_12$ (see Figure 5.2).

The intermediate space group $P4_12_12$ cannot occur in this case, because all atoms occupy special positions, which fulfil the higher symmetry of the space group $P4_2/mnm$ (so called noncharacteristic orbits) [82]. The atomic arrangement in the low-temperature modification α-K_3NiO_2 is essentially the same as in β-K_3NiO_2.

However, the K2 atoms have been shifted slightly away from the linear chain –Ni–O–K2–O–Ni–, leaving the O–Ni–O dumbbells virtually linear (∠O–Ni–O is 178.9° at 50 K), while the O–K2–O angle is reduced to 157.6° (Figure 5.5).

In addition, in both modifications, potassium atoms occupy two crystallographically independent sites, showing unusual low coordination numbers: 4 for K1 and 2 for K2. The K1–O bond length of 2.78 Å is in good agreement with the sum of the ionic radii of potassium and oxygen ion (Table 5.8). However, when compared with the distances of K2–O of 2.51 Å and 2.56 Å (at 500 K and 50 K, respectively), the obtained value seems to be too small. Also, in both modifications K2 exhibits conspicuously enlarged parameters of thermal motion as compared to the other atoms in the structure, particularly pronounced for U_{33} and U_{12} (Table 5.4 and

Table 5.2.: Crystal data and structure refinement data for α-K_3NiO_2.

Space Group, Z	$P4_12_12/P4_32_12$ twin, 4	$P4_12_12/P4_32_12$ twin, 4	$P4_12_12/P4_32_12$ twin, 4
Cell parameters/Å	a = 6.0280(9) c = 13.769(3)	a = 6.012(4) c = 13.843(8)	a = 6.0300(9) c = 14.065(3)
Temperature/K	50	100	298
Cell Volume/Å^3	500.3(1)	500.3(5)	511.4(1)
M_r/g/mol	208.01	208.01	208.01
Calculated density/g/cm^3	2.761	2.762	2.702
Crystal form, color	Block, transparent red	Block, transparent red	Block, transparent red
Crystal size/mm	0.2 × 0.15 × 0.1	0.25 × 0.12 × 0.1	0.25 × 0.12 × 0.1
Difrfractometer	Bruker AXS, APEX SMART CCD	Bruker AXS, APEX SMART CCD	Bruker AXS, APEX SMART CCD
Monochromator	Graphite	Graphite	Graphite
X-ray radiation/λ/Å	Mo-K_α, 0.71073	Mo-K_α, 0.71073	Mo-K_α, 0.71073
θ range/^{o}	3.69 to 36.33	3.69 to 34.79	3.68 to 36.33
Index range	– 10 ≤ h ≤ 10 – 9 ≤ k ≤ 10 – 22 ≤ l ≤ 22	– 9 ≤ h ≤ 9 – 9 ≤ k ≤ 9 – 21 ≤ l ≤ 21	– 10 ≤ h ≤ 9 – 10 ≤ k ≤ 9 – 23 ≤ l ≤ 23
Absorption correction	Multi-scan, SADABS [81]	Multi-scan, SADABS [81]	Multi-scan, SADABS [81]
Total no. reflections, N_{all}	9462	5101	9546
Independent reflections, N	1208	1058	1243
Reflections with $I > 2\sigma(I)$, $\acute{N}$	1187	934	962
Absorption coefficient/μ/mm^{-1}	6.224	6.224	6.089
Volume fractions of twin domains	0.53(2)/0.47(2)	0.52(4)/0.48(4)	0.53(5)/0.47(8)
F(000)	404	404	404
Refinement method	Full matrix least-squares on F^2	Full matrix least-squares on F^2	Full matrix least-squares on F^2
Weighting Scheme	$w = 1/[\sigma^2(Fo^2) + (0.0149P)^2 + 0.1396P]$ where $P = (F_0{}^2 + 2F_c{}^2)/3$	$w = 1/[\sigma^2(Fo^2) + (0.0390P)^2 + 0.1346P]$ where $P = (F_0{}^2 + 2F_c{}^2)/3$	$w = 1/[\sigma^2(Fo^2) + (0.0430P)^2 + 0.4157P]$ where $P = (F_0{}^2 + 2F_c{}^2)/3$
Goodness-on-fit on F^2	1.196	1.161	1.073
R_1 ($\acute{N}$, N)	0.0143; 0.0146	0.0292; 0.0340	0.0318; 0.0453
wR_2 ($\acute{N}$, N)	0.0377; 0.0379	0.0698; 0.0728	0.0823; 0.0911

Table 5.7). The same phenomenon has been noticed for the structure refinements performed previously [15] as well as for isostructural compounds such as K_3FeO_2, ($P4_12_12$) [15], Li_3BN_2 [83, 84], $LiSr_2CoN_2$ [85] and $Li_xCa_2Cu_{1-x}N_2$ ($P4_2/mnm$) [86]. The origin of this particular feature could be dynamic or static disorder. In order to distinguish these two possibilities, the structure refinements were performed using intensity data sets which had been collected at different temperatures (50 K, 75 K, 100 K, 150 K, 200 K, 250 K).

The observed anisotropic displacement parameters, which define the thermal ellipsoids, i.e. the position probability of an atom, are strongly temperature dependent,

Table 5.3.: Atomic coordinates and isotropic displacement parameters / Å^2 for α-K_3NiO_2.

Atom	Site	x	y	y	U_{eq}
Ni					
50 K	4a	–0.0061(1)	–0.0061(1)	0	0.0005(1)
100 K		–0.0057(1)	–0.0057(1)	0	0.0010(1)
298 K		–0.0052(1)	–0.0052(1)	0	0.0017(1)
K1					
50 K	8b	–0.0269(1)	0.4722(1)	0.1255(1)	0.0008(1)
100 K		–0.0252(1)	0.4738(1)	0.1252(1)	0.0015(1)
298 K		–0.0192(1)	0.4788(1)	0.1250(1)	0.0028(1)
K2					
50 K	4a	0.4335(1)	0.4335(1)	0	0.0015(1)
100 K		0.4335(1)	0.4335(1)	0	0.0031(1)
298 K		0.4478(2)	0.4478(1)	0	0.0070(1)
O					
50 K	8b	0.1984(1)	0.7854(1)	0.0148(1)	0.0009(1)
100 K		0.1990(2)	0.7859(2)	0.1040(1)	0.0017(1)
298 K		0.1997(3)	0.7879(3)	0.0105(1)	0.0029(1)

Table 5.4.: Anisotropic displacement parameters ($\times 10^3$) / Å^2 for α-K_3NiO_2.

Atom	U_{11}	U_{22}	U_{33}	U_{23}	U_{13}	U_{12}
Ni						
50 K	4.3(1)	4.3(1)	6.5(1)	–0.1(1)	0.1(1)	0.7(1)
100 K	8.8(1)	8.8(1)	13.3(2)	–0.1(1)	0.1(1)	1.3(1)
298 K	15.6(1)	15.6(1)	20.2(1)	–0.4(1)	0.4(1)	2.8(1)
K1						
50 K	7.7(1)	7.7(1)	7.5(1)	–0.3(1)	0.5(1)	0.5(1)
100 K	15.8(2)	14.9(2)	14.5(2)	–1.2(2)	0.3(2)	0.7(2)
298 K	28.4(3)	31.0(3)	25.7(2)	–2.3(3)	0.9(2)	–0.3(3)
K2						
50 K	8.6(1)	8.6(1)	27.1(2)	–0.4(1)	0.4(1)	4.0(1)
100 K	18.4(2)	18.4(2)	56.9(5)	–1.0(3)	1.0(3)	8.6(2)
298 K	48.1(5)	48.1(5)	113(1)	–1.4(4)	1.4(4)	34.2(6)
O						
50 K	6.8(3)	6.8(3)	12.7(3)	0.3(2)	–1.0(2)	1.5(2)
100 K	12.1(6)	11.2(6)	27.1(6)	0.7(5)	–0.5(6)	2.5(4)
298 K	20.3(7)	21.6(7)	45.3(9)	2.4(9)	–0.1(9)	7.0(5)

especially the U_{11}, U_{22}, U_{33} and U_{12} parameters for K2.

This tendency is more obviously visible from a plot of the principal mean square atomic displacements (U_{min}, U_{med}, U_{max}) for K2 against temperature, as shown in Figure 5.7. What can be noticed from this plot is that the U_{min}, U_{med}, U_{max} values are considerably reduced and quite uniform at 50 K, which implies that a dynamic type of disorder is present in the structure. In order to have a better visual representation of this trend of the K2 atom thermal motion, the crystal structure of K_3NiO_2 is presented in terms of anisotropic parameters at different temperatures (Figure 5.6 and Figure 5.5). It can be easily seen, that at 50 K thermal oscillations

Table 5.5.: Crystal data and structure refinement data for β-K_3NiO_2.

Space Group, Z	$P4_2/mnm$, 2
Cell parameters/Å	a = 6.0310(9) c = 7.156(1)
Temperature/K	500
Cell Volume/Å^3	511.17(6)
M_r/g/mol	260.28(7)
Calculated density/g/cm^3	2.702
Crystal form, color	Block, transparent red
Crystal size/mm	0.25 × 0.12 × 0.1
Difrfractometer	Bruker AXS, APEX SMART CCD
Monochromator	Graphite
X-ray radiation/λ/Å	Mo-K_α, 0.71073
θ range/^{o}	4.42 to 34.70
Index range	$-9 \leq h \leq 9$ $-9 \leq k \leq 9$ $-11 \leq l \leq 11$
Absorption correction	Multi-scan, SADABS [81]
Total no. reflections, N_{all}	3731
Independent reflections N	333
Reflections with $I > 2\sigma(I)$, $\acute{N}$	262
Absorption coefficient/μ/mm^{-1}	5.982
$F(000)$	202
Refinement method	Full matrix least-squares on F^2
Weighting Scheme	$w = 1/[\sigma^2(Fo^2) + (0.0534P)^2 + 0.1973P]$ where $P = ({F_0}^2 + 2{F_c}^2)/3$
Goodness-on-fit on F^2	1.153
R_1 ($\acute{N}$, N)	0.0371; 0.0458 1
wR_2 ($\acute{N}$, N)	0.1045; 0.1115

of all atoms present in the structure are uniformly described.

5.1.5. Discussion

Backed by group theoretical considerations, apparent inconsistencies of the coefficients of thermal motion as determined for K_3NiO_2 have been rationalized. The same observation of substantially enlarged U_{33} and U_{12} for one of the two crystallographically independent potassium atoms was found in previously reported isostructural K_3FeO_2 ($P4_12_12$) [15] and related Li_3BN_2 [83, 84], or $LiSr_2CoN_2$ [85] ($P4_2/mnm$). We have shown that at the synthesis conditions of 873 K, K_3NiO_2 forms as the high temperature polymorph β-K_3NiO_2 in space group $P4_2/mnm$, and undergoes a phase transition at 423 K (150 °C) to the ambient temperature form (α-K_3NiO_2). Neither of the two space groups offers any possibility to trace back the enhanced thermal motion of K2 to causes other than dynamic disorder. This result has been corroborated by refinements on data sets recorded down to 50 K, which show a substantial reduction of the anisotropy and the total (U_{eq}) of thermal motion of K2. Thus,

Table 5.6.: Atomic coordinates and isotropic displacement parameters / Å^2 for β-K_3NiO_2.

Atom	Site	x	y	y	U_{eq}
Ni	$2b$	0	0	0	0.0031(1)
K1	$4d$	0	1/2	1/4	0.0052(1)
K2	$2a$	1/2	1/2	0	0.0148(2)
O	$4g$	0.2054(4)	0.7946(4)	0	0.0055(1)

Table 5.7.: Anisotropic displacement parameters ($\times 10^3$) / Å^2 for β-K_3NiO_2.

Atom	U_{11}	U_{22}	U_{33}	U_{23}	U_{13}	U_{12}
Ni	29(1)	29(1)	35(1)	0	0	5(1)
K1	55(1)	55(1)	44(1)	0	0	0
K2	137(3)	137(3)	169(4)	0	0	111(3)
O	40(1)	40(1)	85(3)	0	0	14(1)

Table 5.8.: Interatomic distances and coordination numbers (CN) for / Å^2 for K_3NiO_2.

Atom	O	CN
Ni (50 K)	1.773	2
Ni (100 K)	1.767	2
Ni (298 K)	1.762	2
Ni (500 K)	1.752	2
K1 (50 K)	2.733	4
	2.780	
	2.781	
	2.822	
K1 (100 K)	2.734	4
	2.776	
	2.781	
	2.825	
K1 (298 K)	2.763	4
	2.794	
	2.796	
	2.834	
K1 (500 K)	2.809	4
K2 (50 K)	2.558	2
K2 (100 K)	2.549	2
K2 (298 K)	2.543	2
K2 (500 K)	2.513	2

these numbers reflect thermally induced displacements, the pronounced anisotropy of which is primarily an intrinsic consequence of the unusual low coordination of K2

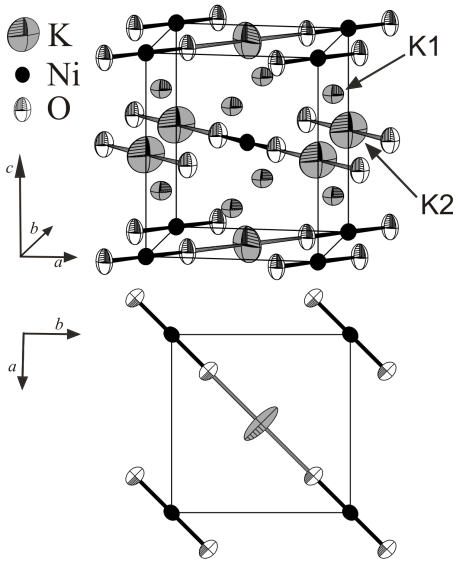

Figure 5.5.: Crystal structure of β-K_3NiO_2 at 500 K and its presentation in the *ab* plane. Displacement ellipsoids are drawn at the 50 % probability level.

by only two oxygen atoms.

5.1.6. Magnetic Measurements

The magnetic susceptibility of a K_3NiO_2 powder sample was measured using a SQUID - magnetometer, in the temperature range 1.8–400 K at different strengths of the magnetic field (0.01–7 T). The magnetic susceptibility shows paramagnetic behavior in the whole temperature range (Figure 5.8), where magnetic behavior of K_3NiO_2 can be well described with the modified *Curie-Weiss* law, which contains a temperature independent positive contribution χ_0 (Eq. 5.2).

$$\chi_{mol}^{exp} = \frac{C}{T - \theta} + \chi_0 \tag{5.2}$$

χ_{mol}^{exp} - measured molar susceptibility
T - temperature
C - *Curie* constat
θ - *Weiss* constant
χ_0 - temperature independent factor

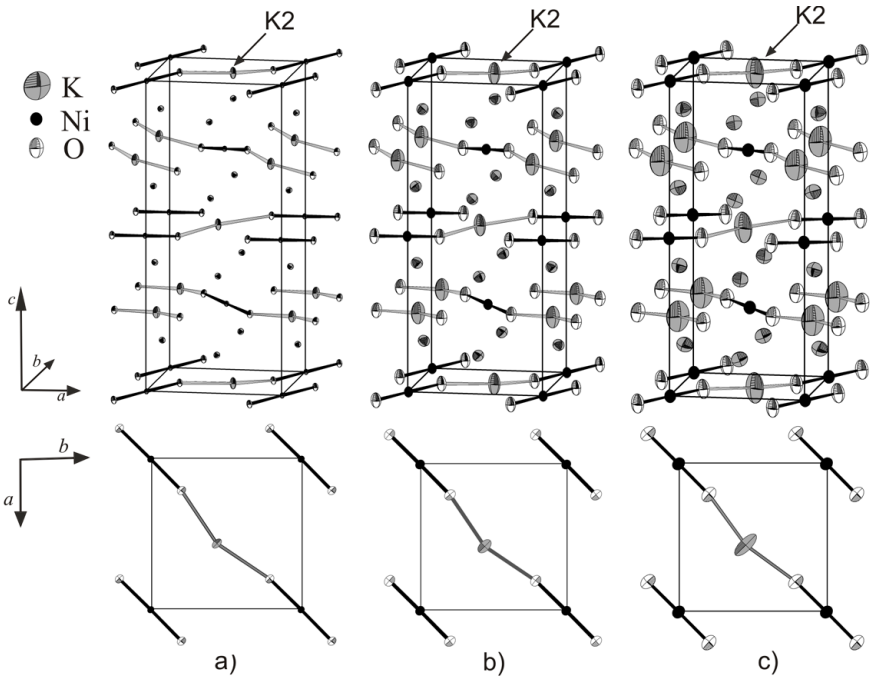

Figure 5.6.: Crystal structure of α-K_3NiO_2 and its presentation in the ab plane (a) at 50 K (b) at 100 K (c) at 298 K. Displacement ellipsoids are drawn at the 75% probability level.

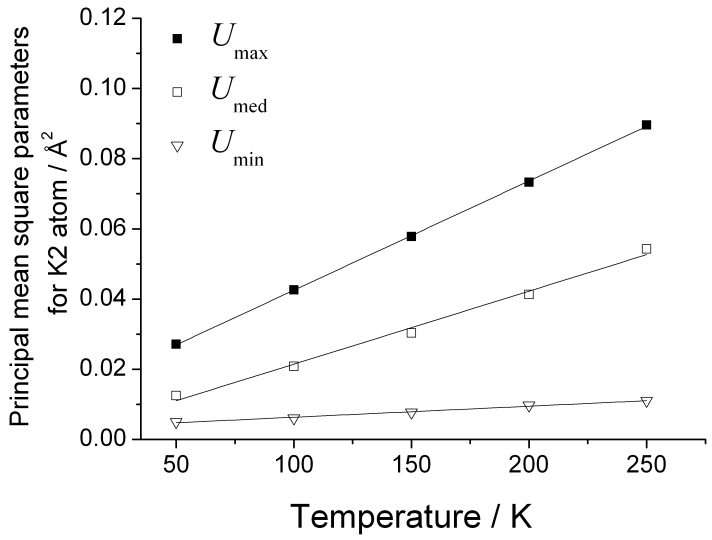

Figure 5.7.: Principal mean square parameters for the atom K2 in α-K_3NiO_2 as a function of temperature.

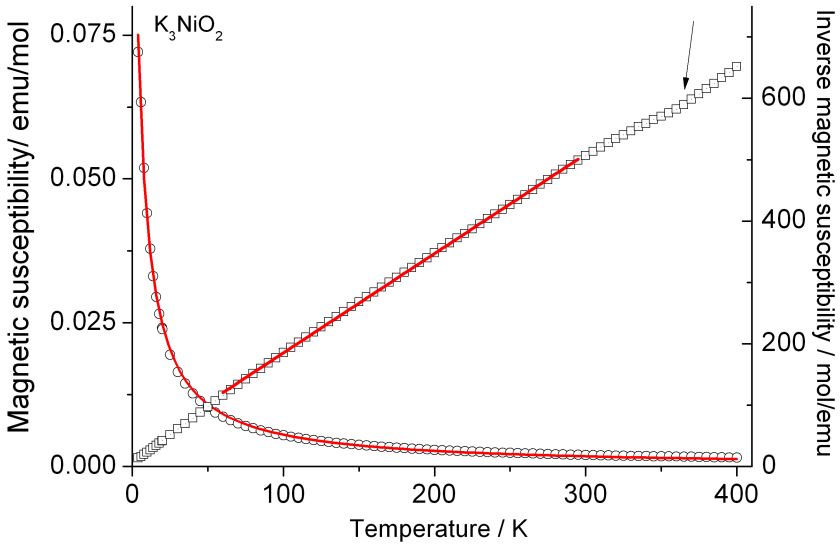

Figure 5.8.: χ - T and $1/\chi$ - T Magnetic susceptibility behavior and magnetic field $H \rightarrow \propto$ of for K_3NiO_2.

In general, the temperature independent factor χ_0 can be described with two different contributions:

$$\chi_0 = \chi_{vV} + \chi_{ferro}(H) \tag{5.3}$$

χ_{vV} corresponds to the *van Vleck*-paramagnetism, which is a field independent contribution. $\chi_{ferro}(H)$ is a strongly temperature dependent term due to ferromagnetic impurities inside the sample. The measured magnetic susceptibility of K_3NiO_2 exhibits a slight field dependency, which implies the presence of ferromagnetic impurities. This impact could also be seen from the values of χ_0 evaluated at different magnetic fields. According to a preliminary investigation of the K–Ni–O solid state system along the azide-nitrate route, there is a phase equilibrium between K_3NiO_2 and elementary nickel phases. Therefore, the formation of a small amount of ferromagnetic nickel impurity can hardly be avoided during the synthesis (these impurities influences magnetic behavior, even if they are below the detection limit of XRD powder diffraction). However, the influence of these ferromagnetic impurities on the proper K_3NiO_2 susceptibility can be eliminated by the substraction method of *Honda* and *Owen*. With this method the molar susceptibility is being measured

at different strengths of magnetic fields ($H > 1$ T) and different temperatures, and χ_{mol} is than extrapolated to infinite magnetic field ($1/H \rightarrow 0$). Afterwards, the extrapolated magnetic susceptibility is ploted against temperature. This correction is based on the principle that at the infinite high magnetic field it comes to a saturation of ferromagnetic impurities, meaning that the only response being recorded comes from the sample.

Figure 5.9, presents the d-orbital splitting in the linear crystal field. Ni(I) having the d^9 configuration, should comply with the expectation to have a spin S = 1/2 contribution. Based on the evaluation of the Curie-Weiss law (in the 60–300 K temperature range), the calculated magnetic moments for K_3NiO_2 are $\mu = 2.22$ μ_B. These values, in the range of $\mu = 1.70$–2.20 μ_B are in a good agreement with expected magnetic moments for a spin contribution of a d^9 free ion, with orbital contribution. The value of the Weiss constant close to $\theta \sim$ –14.4 K indicates to a presence of antiferromagnetic interactions.

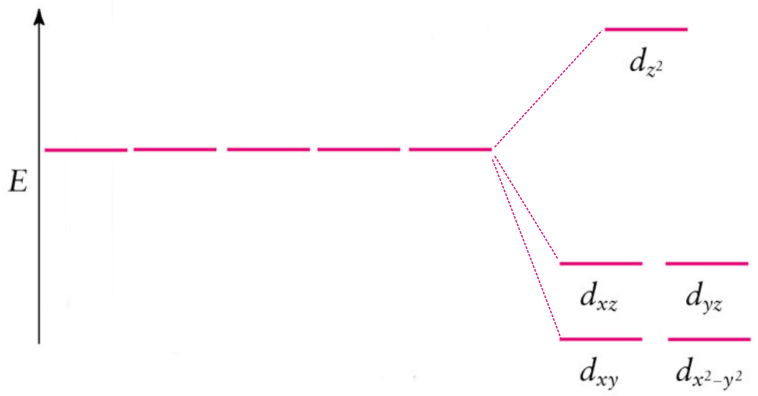

Figure 5.9.: d-orbital splitting in the linear crystal field.

From Figure 5.8 it can also be noticed that a slight change in the susceptibility is seen in the temperature range 380–400 K. This observation can be good related to the results obtained from temperature dependent powder X-ray diffraction, indicating a first-order phase transition. The high-temperature phase (β-K_3NiO_2) possesses the higher symmetry, where the $[O–Ni–O]^{3-}$ dumbbells are totally linear, while at lower temperatures (in the (α-K_3NiO_2 modification) these dumbbells are slightly distorted from their linearity. The Ni(I)ion oxygen environment could have an impact on the

change in the susceptibility.

5.2. Synthesis, Crystal Structure, Phase Transition and Magnetic Properties of Rb_3NiO_2

5.2.1. Synthesis and Thermal Analysis

Starting materials for the preparation of Rb_3NiO_2 were RbN_3, $RbNO_3$ and NiO, and the first step in the synthesis of this material consisted of drying the starting compounds at 130°C/12h under vacuum (10^{-3} mbar). Rubidium azide was prepared from aqueous HN_3 and rubidium carbonate. Nickel oxide NiO is obtained as described in the section 4.3.1. The starting compounds were mixed in an agate mortar in a molar ratio according to the following reaction:

$$8RbN_3 + RbNO_3 + 3NiO \rightarrow 3Rb_3NiO_2 + \frac{25}{2}N_2 \tag{5.4}$$

In this procedure 3 mol of RbN_3 were added in excess. Mixed powder was transported in a silver crucible, provided with the tightly closed steel vessels. In a flow of argon the following temperature treatment was applied: 398 → 533 K (100 K/h) 533 → 653 K (5 K/h), 653 → 723 K (20 K/h) and subsequent annealing for 50 h at 723 K. The obtained powder was dark red, and because it is very sensitive to air and moisture it was sealed in a glass ampoule in an argon atmosphere. All further manipulations were performed in an inert atmosphere of purified argon. The resulting powders turn black when they are exposed to air. According to TG/DTA analysis of Rb_3NiO_2, after 823 K, decomposition of the substance occurs.

5.2.2. Phase Transition

Indexing of the XRD pattern of Rb_3NiO_2 at room temperature (referred to in the following as α-Rb_3NiO_2) gave a tetragonal solution in the space group $P4_12_12$, with the lattice constants for $a = 6.264(1)$ Å, $c = 14.7419(1)$ Å, where Rietveld refinement resulted to isostructural α-K_3NiO_2 (Table 5.9 and 5.10). In situ temperature dependent X-ray powder diffraction revealed that above 400 K, Rb_3NiO_2 exhibits a phase transition, where the structure transforms to the space group of a higher symmetry (β-Rb_3NiO_2, analogue to β-K_3NiO_2). β-Rb_3NiO_2 crystalizes in the space group $P4_2/mnm$ with the lattice constants $a = 6.2748(1)$ Å, $c = 7.5085(1)$ Å (at 523 K). Rietveld plots of α-Rb_3NiO_2 and β-Rb_3NiO_2 polymorphs form are presented

Table 5.9.: Crystallographic data for Rb_3NiO_2 (obtained by Rietveld refinement) at temperatures of 398 K and 523 K.

Space Group, Z	$P4_12_12$ (No.92), 4	$P4_2/mnm$ (No. 136), 2
Temperature/K	303(5)	523(5)
Cell parameters/Å	$a = 6.2644(1)$	$a = 6.2747(1)$
	$c = 14.7419(2)$	$c = 7.5084(1)$
Cell Volume/Å^3	578.52	295.62
Crystal density/g/cm^3	3.98	3.90
Wavelength/Å	1.540598	1.540598
Range data collection ($2\theta/^o$	10–90	10–90
R_{Bragg}/%	2.32	2.81
R_p/%	5.32	6.96
R_{wp}/%	7.16	9.16

in the Figure 5.10.

Table 5.10.: Atomic coordinates and isotropic displacement parameters / Å^2 for α-Rb_3NiO_2.

Atom	Site	x	y	y	U_{eq}
Ni	4a	0.9966(5)	0.9966(5)	0	0.005(1)
Rb1	4a	0.9836(3)	0.4805(3)	0.1261(2)	0.020(1)
Rb2	8b	0.4548(3)	0.4548(3)	0	0.055(2))
O	8b	0.1931(9)	0.7954(9)	0.0096(5)	0.018(3)

Table 5.11.: Atomic coordinates and isotropic displacement parameters / Å^2 for β-Rb_3NiO_2.

Atom	Site	x	y	y	U_{eq}
Ni	2a	0	0	0	0.016(1)
Rb1	4b	0	1/2	1/4	0.031(1)
Rb2	2a	1/2	1/2	0	0.102(3)
O	4b	0.1989(9)	0.8011(9)	1/2	0.025(3)

As the initial starting model for both modifications in the refinement, the coordinates of isostructural α- and β- K_3NiO_2 were used. Also in the Rietveld refinement the coordinates for elementary silver (coming from the silver inlay) and nickel were included, where the calculated amount of these phases was less than 1 %. The phase transition in Rb_3NiO_2 is in agreement with the expectations of the group-subgroup

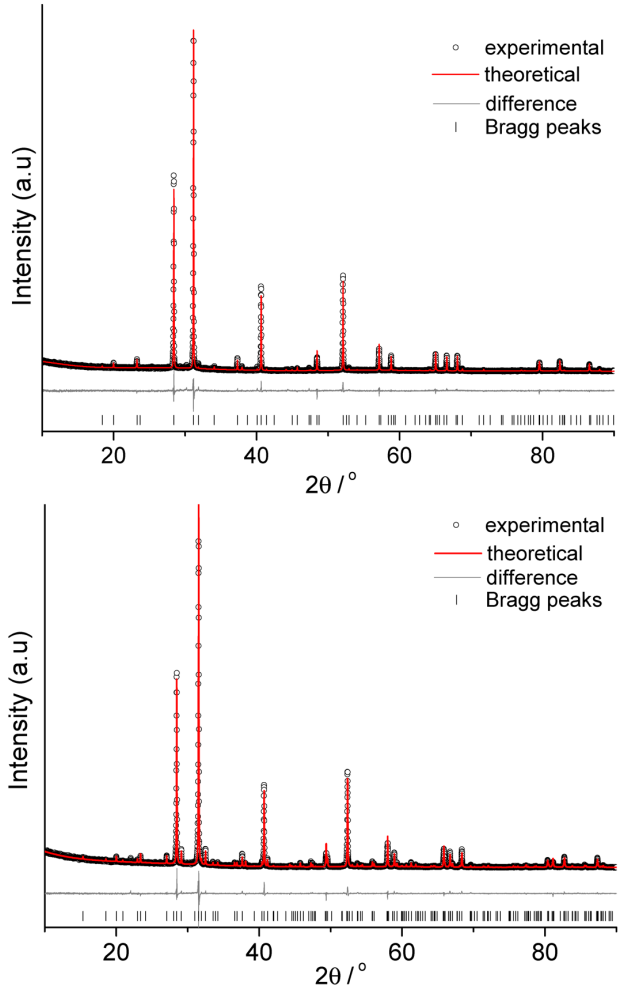

Figure 5.10.: Experimental and calculated XRD patterns for α-Rb_3NiO_2 (lower picture) and β-Rb_3NiO_2 (upper picture). Black marks experimental, red calculated profile. The difference between the experimental and theoretical patterns is given in grey. Bragg positions are given by tick marks.

relations as in K_3NiO_2 (see Figure 5.2). During the heating, the lattice parameters of α-Rb_3NiO_2 are negligibly changed (Figure 5.11). Common to both representatives, K_3NiO_2 and Rb_3NiO_2, is that during the phase transition coexistence of both (α- and β-) phases over a certain temperature range is observed, implying a first order phase transition. In the case of Rb_3NiO_2, the coexistence of the phases is observed in the 370–390 K temperature range, which is approx. 20 K lower as compared with K_3NiO_2.

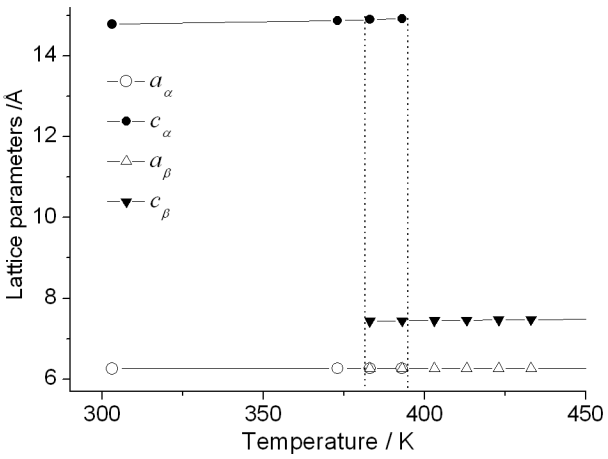

Figure 5.11.: Temperature dependence of the unit cell parameters of Rb_3NiO_2 obtained from Rietveld refinements.

5.2.3. Crystal Structures of the Low-Temperature (α-Rb_3NiO_2) and High-Temperature Modifications (β-Rb_3NiO_2)

An essential feature of the structures for both modifications are isolated O–Ni–O ($[NiO_2]^{3-}$) dumb-bells, formed by Ni(I) ion and oxygen. Orientation and distribution of O–Ni–O units in α-Rb_3NiO_2 is presented in Figure 5.12. These units exhibit very small deviations from linearity and they are slightly bent (O–Ni–O = 178.7 °) (Table 5.12), which is in a fair agreement with the published data for K_3NiO_2 compound (O–Ni–O = 179.6, [15])

The obtained values of Ni–O distances, (Table 5.12), are in a good agreement with the results obtained for isotypic K_3NiO_2 (175.9 pm) as well as $RbNa_2NiO_2$ (176 pm) and KNa_2NiO_2 (177 pm). Rubidium occupies two crystallographically independent sites, where Rb2 has the coordination number 2. Rb1 is coordinated by 4 oxygen ions, forming distorted tetrahedra where the alkali-oxygen bonds (dRb–O = 285.5 pm, 289.5 pm, 296.9 pm, 297.2 pm) follow the same pattern as in K_3NiO_2 (274.5 pm, 281.3 pm, 281.4 pm, 282.3 pm) [15]. These values are in a good agreement with the values of Rb–O distances in Rb_2O (292 pm, resp. [87]). Each Rb1 atom connects four $[NiO_2]^{3-}$ dumb-bells, of which only two are lying in one plane (Figure 5.13).

Coordination number 2 for Rb2 is to low, as well as the Rb2–O distances (269.5 pm). This fact implies that Rb2 follows the same thermal oscillation in the z-direction as for the case of potassium ion (K2) in K_3NiO_2.

Table 5.12.: Interatomic distances (in Å), coordination numbers (CN), and mean fictive ionic radii (MEFIR) for α-Rb_3NiO_2 and β-Rb_3NiO_2.

	O	CN	Denoted angles	Angles/°
α-Rb_3NiO_2				
Ni	1.767	2	O–Ni–O	178.7
Rb1	2.879	4	O1–Rb1–O2	107.4
	2.927		O1–Rb1–O3	115.7
	2.938		O1–Rb1–O4	102.0
	2.950		O2–Rb1–O3	101.2
			O2–Rb1–O4	110.7
			O3–Rb1–O4	119.5
Rb2	2.695	2	O–Rb2–O	165.1
β-Rb_3NiO_2				
Ni	1.771	2	O–Ni–O	180.0
Rb1	2.941	4	O–Rb1–O	180.0
Rb2	2.666	2	O–Rb2–O	180.0

The crystal structure of β-Rb_3NiO_2 is shown in Figure 5.14, where the Rb2 atom is schown with the anisotropic displacement parameters (50 % probability level). β-Rb_3NiO_2 is isostructural to β-K_3NiO_2. During the phase transition from α- to β-form it can be seen that the $\angle$ O–Rb2–O changes from 165.1° to 180.0° and thus creating totally linear [–O–Ni–O–Rb2–O–Ni–O–] chains. The smaller values of the $\angle$ O–K2–O angle (162.2°) in the potassium representative brings out the fact that with the incorporation of the bigger alkali ion in the structure, the distortion from the linearity of the [–O–Ni–O–Rb2–O–Ni–O–] chain is smaller.

5.2.4. Magnetic Measurements

The magnetic susceptibility has been measured on a powder sample in the temperature range from 2–400 K, at magnetic fields of 1–7 T. The measured magnetic susceptibility exhibits a small field dependency. In Figure 5.15, the magnetic behavior of Rb_3NiO_2 is shown (corrected for diamagnetic contributions of the closed electronic shells and for traces of ferromagnetic impurities by the Honda-Owen extrapolation). The diamagnetic contribution of the closed electronic shells were estimated using the increments: $Rb^{+1} = 25 \times 10^{-6}$ cm^3/mol, $Ni^{+2} = 15 \times 10^{-6}$ cm^3/mol, $O^{2-} = 15$

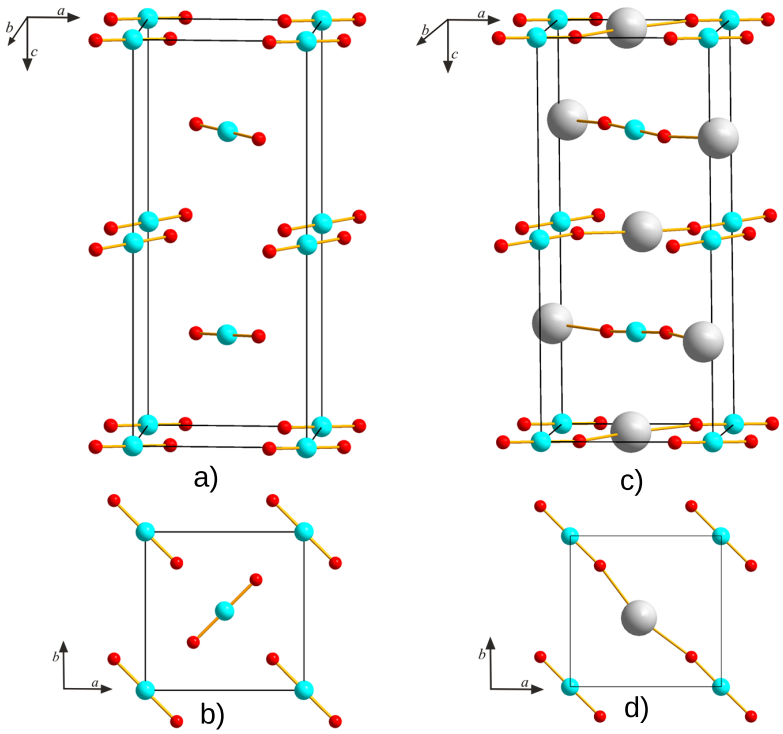

Figure 5.12.: Primary and secondary structure of Rb_3NiO_2.

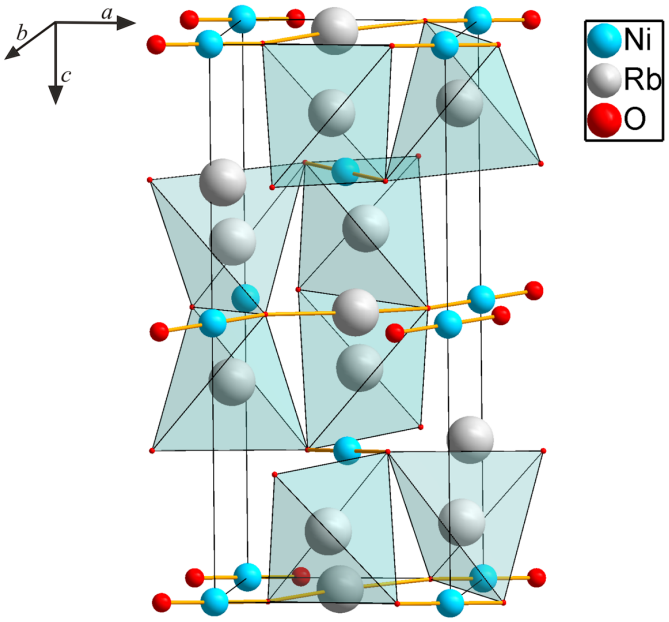

Figure 5.13.: Crystal structure of Rb_3NiO_2.

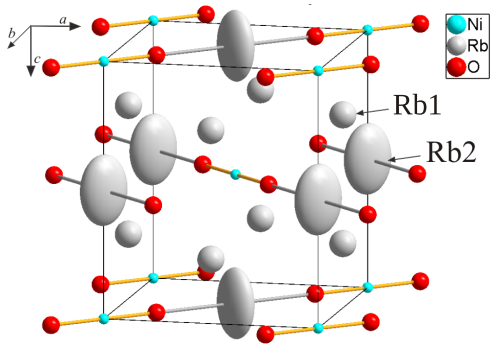

Figure 5.14.: Crystal structure of β-Rb_3NiO_2. Displacement ellipsoid is drawn at the 50 % probability level.

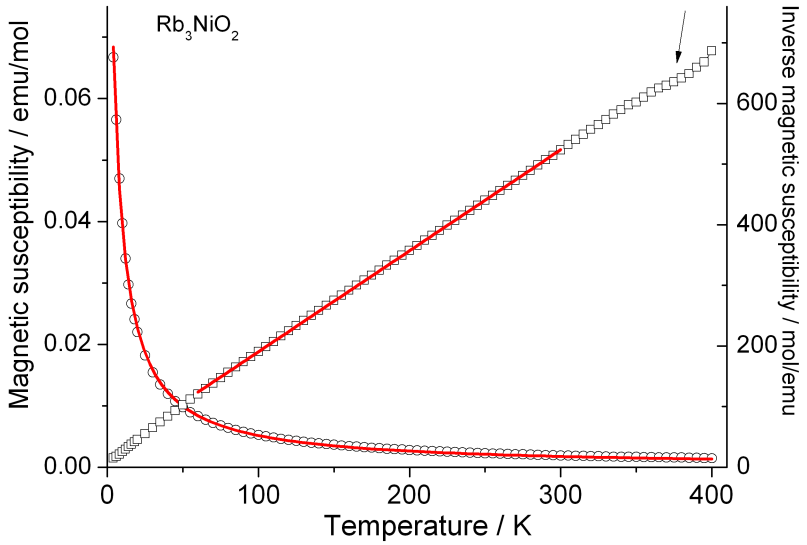

Figure 5.15.: χ - T and $1/\chi$ - T Magnetic susceptibility behavior and magnetic field $H \rightarrow \infty$ for Rb_3NiO_2.

$\times$ 10^{-6} cm^3/mol [46].

The magnetic susceptibility of Rb_3NiO_2 shows paramagnetic behavior over the whole temperature range. The magnetic moment was derived with the help of the Curie-Weiss law from the corrected values of magnetic susceptibility data (Figure 5.15). Obtained values of the magnetic moment is $\mu = 2.11$ μ_B are in good agreement with a magnetic moment as expected for a d^9 free ion [46], including a slight orbital contribution. The negative value of the Weiss contant $\theta \sim$ –9.37 K indicates the

presence of small antiferromagnetic interactions.

For the magnetic behavior, in the temperature range 350–400 K, it can be noticed that it comes to a slight change in the susceptibility. In the same temperature range it comes to a phase transition where the coexistence of both (α and β) phases occurs. This phenomenon is in a good correlation with the structural phase transition in Rb_3NiO_2.

5.3. Synthesis, Structure and Magnetic Properties of Cs_3NiO_2

5.3.1. Synthesis and Thermal Analysis

Starting materials for the preparation of Cs_3NiO_2 were CsN_3, $CsNO_3$ and NiO, which were first dried at 373 K/12h under vacuum (10^{-3} mbar). The synthesis of caesium azide and nickel oxide is described in sections 4.1 and 4.3.1. The starting compounds were mixed in an agate mortar in a molar ratio according to the following reaction:

$$8CsN_3 + CsNO_3 + 3NiO \rightarrow 3Cs_3NiO_2 + \frac{25}{2}N_2 \tag{5.5}$$

In this procedure 2 mol of CsN_3 were added in excess. The mixed powder was transported to specially designed container provided with the silver inlay (section 2.4). In a flow of argon the following temperature treatment was applied: 298 → 533 K (100 K/h) 533 → 653 K (5 K/h), 653 → 723 K (100 K/h), and subsequent annealing for 30 h at 723 K. The obtained powder was dark red, and because it is very sensitive to air and moisture it was sealed in a glass ampoule in an argon atmosphere. All further manipulations were performed in an inert atmosphere of purified argon. The thermal analysis revealed that the sample is thermally stable up to ∼ 823 K.

5.3.2. Structure Solution from X-ray Powder Diffraction - Rietveld Refinement

Phase pure powder of Cs_3NiO_2 was obtained according to equation 5.5. Indexing of obtained X-ray powder pattern suggested that Cs_3NiO_2 crystallizes tetragonal with the lattice constants a= 6.4337 Å and c= 8.0798 Å. Rietveld refinement of Cs_3NiO_2 at room temperature showed the compound to be isostructural to β-K_3NiO_2. Temperature dependent X-ray powder measurements of Cs_3NiO_2 were performed up to 433 K. However, there were not any hints for changing in the phase composition.

The crystallographic data of the final Rietveld refinement (Figure 5.16) are listed in Table 5.13, the coordinates are given in Table 5.14. A selection of interatomic

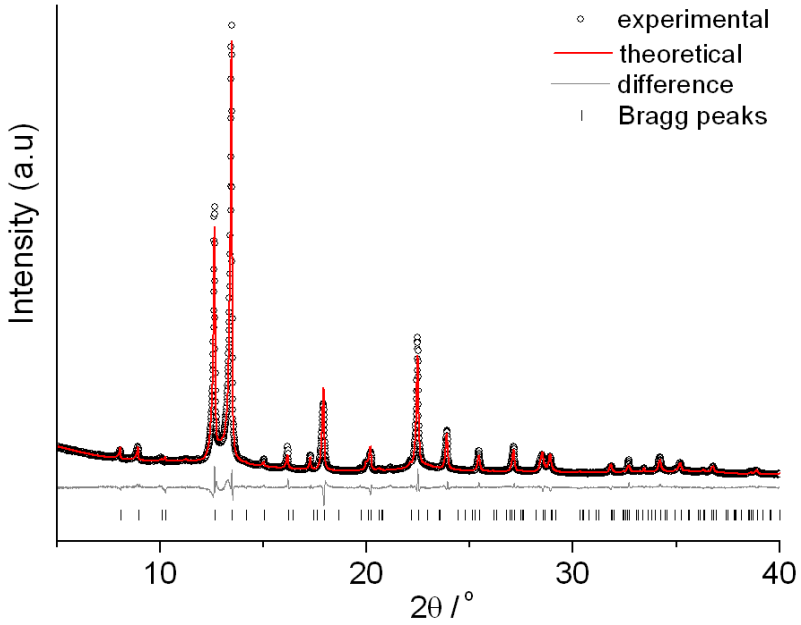

Figure 5.16.: Experimental and calculated XRD patterns for Cs_3NiO_2. Black marks - experimental, red - calculated profile. The difference between the experimental and theoretical patterns is given in grey. Bragg positions are given by tick marks.

Table 5.13.: Crystallographic data for Cs_3NiO_2 (obtained by Rietveld refinement) at temperatures of 398 K and 523 K.

Space Group, Z	$P4_2/mnm$ (No. 136), 2
Temperature/K	298(5)
Cell parameters/Å	a = 6.4336(3)
	c = 8.0844(4)
Cell Volume/Å^3	334.6
Calculated density/g/cm^3	4.86
Wavelength/Å	0.7093
Range data collection ($2\theta/^o$	4–40
R_I/%	2.72
R_p/%	3.73
R_{wp}/%	5.21

distances and angles is given in Table 5.15.

Cs_3NiO_2 crystallizes isostructurally to the β-A_3NiO_2 (A = K, Rb) members of the family, in the space group $P4_2/mnm$. Since the isotropic parameters of the Cs2 ion in the structure are increased (Table 5.14), it was possible to refine them anisotropically as well. The crystal structure of Cs_3NiO_2 is presented in the Figure

Table 5.14.: Atomic coordinates and isotropic displacement parameters / Å^2 for Cs_3NiO_2.

Atom	Site	x	y	y	U_{eq}
Ni	$2a$	0	0	0	0.009(3)
Cs1	$4b$	0	1/2	1/4	0.052(2)
Cs2	$2a$	1/2	1/2	0	0.137(4)
O	$4b$	0.194(2)	0.806(2)	0	0.077(2)

Table 5.15.: Interatomic distances (in Å) and coordination numbers (CN) for Cs_3NiO_2.

	O	CN	Denoted angles	Angles/°
Ni	1.762	2	O–Ni–O	180.0
Cs1	3.085	4	O–Cs1–O	180.0
			O1–Cs1–O2(4)	98.2
			O1(2)–Cs1–O3(4)	115.4
Cs2	2.787	2	O–Cs2–O	180.0

5.17, where the occupation of the Cs2 ion is displayed with the anisotropic thermal tensors. It can be seen that the ratio of the thermal oscillations of the caesium ion correspond to those in potassium and rubidium oxonickelate(I) (Figures 5.5 and 5.14).

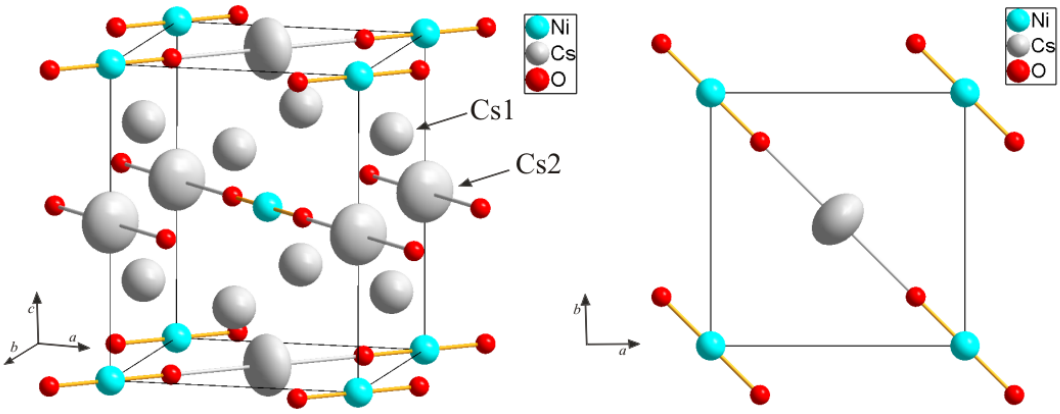

Figure 5.17.: Crystal structure of Cs_3NiO_2 (left); Projection of the Cs_3NiO_2 in the *ab*-plane.Displacement ellipsoid is drawn at the 50 % probability level.

5.3.3. Magnetic Measurements

Magnetic susceptibility measurements were performed on the powder sample using a SQUID magnetometer at different strengths of the magnetic field (1–7 T). Cs_3NiO_2 exhibits paramagnetic behavior over the whole temperature range, where the susceptibility can be well described with the Curie-Weiss law in the temperature range (60–300 K). However, the Honda-Owen correction had to be applied due to the presence of ferromagnetic impurities.

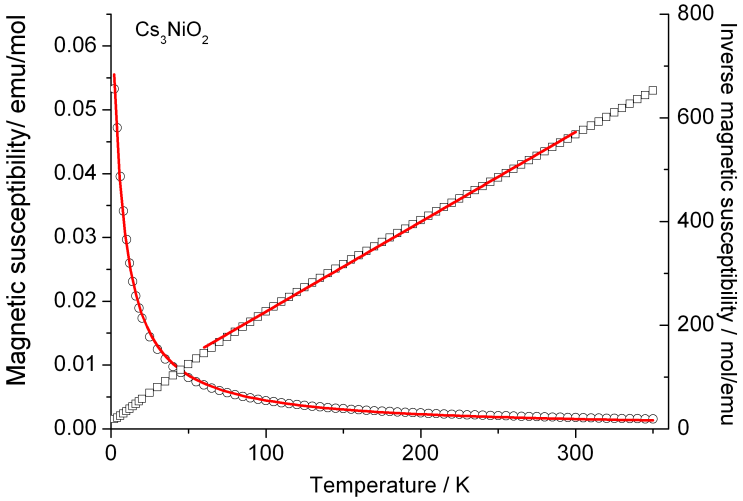

Figure 5.18.: χ - T and $1/\chi$ - T magnetic susceptibility behavior and magnetic field $H \rightarrow \propto$ of for Cs_3NiO_2.

The effective magnetic moment amounts to $\mu = 2.15\ \mu_B$ per nickel atom, which is very close to the value expected for the effective magnetic moment of a d^9 free ion, with an orbital contribution. The Curie-Weiss value close to –30.5(1.5) K indicates strong antiferromagnetic interactions in this system, the highest in the A_3NiO_2 family of compounds.

5.4. Discussion of the A_3NiO_2 Family of Compounds

In this work we showed that the azide/nitrate route has proven to be a convenient method in the synthesis of alkali-metal oxonickelates(I), for obtaining both a good quality single crystal (in the case of K_3NiO_2) and phase pure powders.

Thanks to the azide-nitrate route we have managed to synthesize two new alkali-metal oxonickelates(I), where in the case of α-Rb_3NiO_2 it was found that the room-temperature and high-temperature modification is isostructural to α-K_3NiO_2 and β-K_3NiO_2. The phase transition from the α- to the β- polymorph is not accompanied by big changes in the local structure elements. The only difference observed is the formation of (totally) linear $[O–Ni–O]^{3-}$ units in the α-form, as well as change of the O–A2–O angle from 162.3° (for K2, 298 K) and 165.1° (for Rb2, 298 K) to 180°. In Cs_3NiO_2, the incorporation of the Cs ion leads to a linear O–Cs2–O angle already at room temperature. Temperature dependent X-ray analysis of the α-polymorph of the rubidium and potassium analogues, revealed that displacements of atoms are increasing with lowering the temperature (considering the corresponding β-forms as undistorted), where the largest displacement is noticed for the A2 ion (A = K, Rb) (Figure 5.19, the analysis was performed using the program AMPLIMODES [88]).

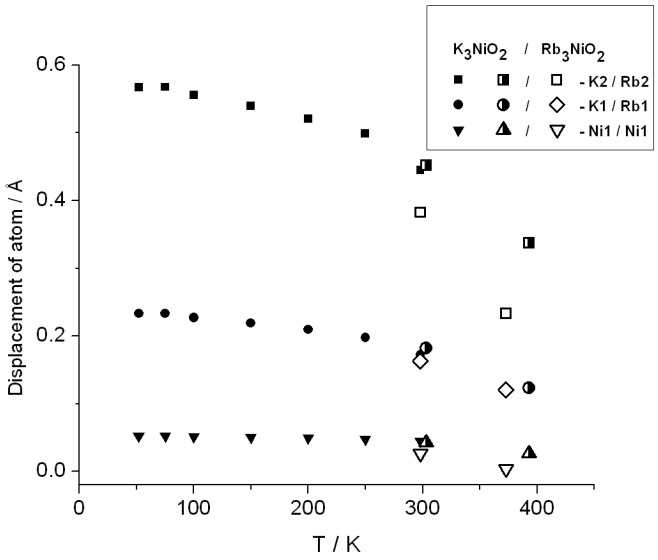

Figure 5.19.: Temperature dependent atomic displacement in α-K_3NiO_2 and α-Rb_3NiO_2. Full symbols - single crystal data of α-K_3NiO_2, half-full symbols - powder data of α-K_3NiO_2, empty symbols - powder data of α-Rb_3NiO_2.

Table 5.16 gives the Madelung part of the lattice energy for oxonickelates(I) (at room temperature). The values obtained are in a good agreement within the analogues.

The magnetic susceptibilities of all three family members exhibit similar temperature dependences (Figure 5.8, 5.15 and 5.18). The evaluation of the magnetic

Table 5.16.: Madelung Part of Lattice Energy, MAPLE in kcal/mol for K_3NiO_2, Rb_3NiO_2 and Cs_3NiO_2 at room temperature.

	K_3NiO_2	Rb_3NiO_2	Cs_3NiO_2
A1	180.1	184.1	191.7
A2	104.7	100.1	94.6
Ni	97.8	91.4	86.6
O	416.1	401.3	386.0
$\sum$	1319.5	1278.2	1239.6

data according to the Curie-Weiss law alowed magnetic moments as expected for a Ni(I)-$3d^9$ system. The magnetic moments as determined are about 2.2 μ_B for all three representatives which indicates a substantial orbital contributions. This result agrees with the g-values of 2.3 as observed and calculated by A. Möller [89] for K_3NiO_2. The inverse magnetic susceptibility curves of K_3NiO_2 and Rb_3NiO_2 exhibit a slight shift in the 370 – 400 K temperature range, which corresponds to the structural α- to β- phase transition. The inverse magnetic susceptibility of Cs_3NiO_2 exhibits linear behavior in the whole temperature range (4 – 350 K).

6.

Cs_2NiO_2 Revisited: Crystal Structure and Magnetic Properties

6.1. Introduction

Linear molecules may be assumed to arise from tetragonal MX_4Z_2 by removing the equatorial (X) ligands to infinity. The most investigated linear transition metal complexes are transition metal dihalides, which are studied either in the gas phase or in the matrix isolation studies [58]. The electronic and geometric structure of this type of compounds is still challenging for both, experimental and theoretical chemistry. Linear coordination geometries are usually a characteristic structural feature in the chemistry of transition metals with $n\mathrm{d}^{10}(n{+}1)\mathrm{s}^0(n{+}1)p^0$ electron configuration. However, linear [X–M–X] anions are also quite common for Fe, Co and Ni in low oxidation states. In addition to the dihalides, new alkali-metal oxometalates were synthesized containing the O–Ni–O linear units (K_2NiO_2, Rb_2NiO_2, Cs_2NiO_2 [1]). The discovery of this type of compounds has opened a new challenge towards investigation of their physical properties as well as electronic structure. Potassium and rubidium representatives have been well characterized and re-investigated with respect to their magnetic and optical properties [89,90]. However, knowledge about Cs_2NiO_2 has still remained rudimentary. In this chapter, the growth of single crystals and a structure determination from single crystal data are reported, as well as the magnetic properties of a single phase sample.

Parts of this chapter are included in the publication "Cs_2NiO_2 Revisited: Crystal Structure and Magnetic Properties" [91].

6.1.1. Synthesis and Thermal Analysis

Starting materials for the preparation of dicaesium nickelate(II) were caesium azide, caesium nitrate (Riedel-De Han AG Seelze Hannover 99.5 %) and NiO, prepared by decomposition of $NiC_2O_4 \cdot 2\ H_2O$ (Alfa Aesar, 98 %) in a flow of oxygen at 623 K for 20 h. The caesium azide was synthesised from aqueous HN_3 and $CsCO_3$ (Sigma Aldrich, 99 %). The starting compounds were dried under vacuum (10^{-3} mbar) at 393 K over night, mixed and thoroughly ground in an agate mortar in a glove box, and placed under argon in a tightly closed steel container, provided with a silver inlay [92].

$$5CsN_3 + CsNO_3 + 3NiO \rightarrow Cs_2NiO_2 + 8N_2 \tag{6.1}$$

Green microcrystalline samples of Cs_2NiO_2 were obtained from stochiometric mixtures of the reactants according to reaction 6.1, and applying the following temperature treatment: 298 → 533 K (100 K/h) 533 → 653 K (5 K/h), 653 → 773 K (20 K/h) and subsequent annealing for 30 h at 773 K.

Single crystals of Cs_2NiO_2 were obtained when an excess of azide and nitrate as related to equation 6.1 was used (30 % molar excess for CsN_3 and 150 % excess for $CsNO_3$) and the mixture heated with the following temperature program: 298 → 533 K (100 K/h), 533 → 653 K (5 K/h), 653 → 723 K (20 K/h), with a subsequent annealing for 100 h at 723 K.

The obtained powders as well as the single crystals are very sensitive towards air and moisture, thus they were sealed in glass ampoules under argon atmosphere, and all further manipulations were made in an inert atmosphere of purified argon.

Due to high sensitivity to air and moisture, separation of the Cs_2NiO_2 single crystal was performed with the help of the dried Schlenck technique method (as explained in the Chapter 2, Figure 2.7).

According to the thermal analysis its decomposition starts close to 923 K, where above approx. 1073 K NiO is left as the only solid residue (Figure 6.1).

6.1.2. X-ray Single Crystal and Powder Analysis

The crystal structure determination and refinement were performed on X-ray single-crystal data collected at 298 K [91]. Details of the solution are given in Tables

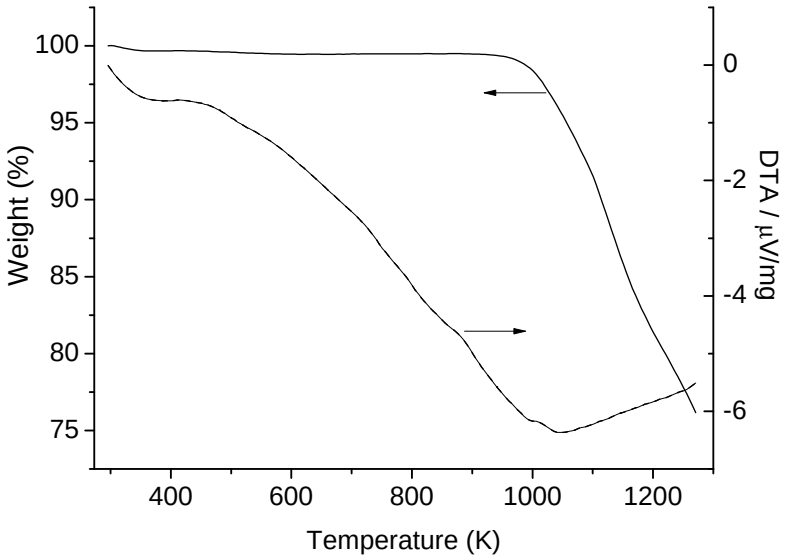

Figure 6.1.: Thermal analysis of Cs_2NiO_2.

6.1- 6.2. According to the results of single crystal refinement, Cs_2NiO_2 crystallizes tetragonal in the space group $I4/mmm$ (Z = 2, a = 4.4090(6), c = 13.576(3) Å). This outcome is in good agreement with the previously published results obtained from powder data [1]. Cs_2NiO_2 crystallizes isostructurally with A_2NiO_2 (A = K, Rb) and can be regarded as a stuffed XeF_2 structure. The green color of this compound originates from the unusual linear O–Ni–O units (d(Ni–O) = 1.68 Å, Figure 6.2), which are aligned parallel to the [001] crystal axis. The electronic spectra of potassium and rubidium representative have been already published [89, 90].

The caesium ion is surrounded by five oxygen atoms, forming a tetragonal pyramid. Adjacent CsO_5–pyramids are connected through their basal edges, which leads to the formation of infinite $^2_\infty$CsO– double sheets. Each of these oxygen atoms is thus common to four pyramids in a $^2_\infty$CsO–sheet, and at the same time they are positioned above those of the pyramids of the adjacent sheet (Figure 6.2b). Interconnection between these double layers is attained through the O–Ni–O units, whose oxygen atoms occupy the apical positions of the CsO_5 pyramids.

K_2NiO_2, Rb_2NiO_2 and Cs_2NiO_2 display identical Ni–O distances (within the margins of experimental error, Table 6.3). However, with the incorporation of the bigger

Table 6.1.: Crystal data and structure refinement data for Cs_2NiO_2.

Space Group, Z	$I4/mmm$, 4
Cell parameters/Å	$a = 4.4090(6)$
	$c = 13.576(3)$
Temperature/K	298
Cell Volume/Å^3	263.91(7)
M_r/g/mol	356.53
Calculated density/g/cm^3	4.49
Crystal form, color	Block, transparent green
Crystal size/mm	$0.25 \times 0.12 \times 0.1$
Difrfractometer	Bruker AXS, APEX SMART CCD
Monochromator	Graphite
X-ray radiation/$\lambda/\mathring{A}$	Mo-K_α, 0.71073
θ range/^{o}	3.00 to 31.57
Index range	$-6 \leq h \leq 6$
	$-6 \leq k \leq 6$
	$-20 \leq l \leq 20$
Absorption correction	Multi-scan, SADABS [81]
Total no. reflections, N_{all}	2922
Independent reflections N	158
Reflections with $I > 2\sigma(I)$, $\acute{N}$	157
Absorption coefficient/μ/mm^{-1}	17.1723
$F(000)$	308
Refinement method	Full matrix least-squares on F^2
Weighting Scheme	$w = 1/[\sigma^2(Fo^2) + (0.0516P)^2 + 0.5355P]$
	where $P = ({F_0}^2 + 2{F_c}^2)/3$
Goodness-on-fit on F^2	1.459
R_1 ($\acute{N}$, N)	0.0364; 0.0389
wR_2 ($\acute{N}$, N)	0.0831; 0.0930

Table 6.2.: Atomic coordinates and anisotropic displacement parameters / Å^2 for Cs_2NiO_2 ($U_{11} = U_{22}$, $U_{12} = U_{13} = U_{23} = 0$).

Atom	Site	x	y	y	U_{eq}	U_{11}	U_{33}
Cs	$4e$	0	0	0.3478(1)	0.0316(6)	0.0318(6)	0.0310(7)
Ni	$2a$	0	0	0	0.0247(6)	0.0245(6)	0.025(1)
O	$4e$	0	0	0.1242(9)	0.044(2)	0.045(3)	0.041(6)

Table 6.3.: Lattice constants and interatomic distances(Å) in A_2NiO_2 (A= K, Rb, Cs) compounds.

	K_2NiO_2 [1]	Rb_2NiO_2 [1]	Cs_2NiO_2
a	3.953	4.166	4.4069*
c	12.853	13.146(2)	13.561(1)*
d(Ni–O)	1.68	1.67	1.68
d(A–O)	2.72	2.87	3.03
d(A–O)	2.82	2.97	3.14

* Lattice contstanst were refined from the powder data

Table 6.4.: Crystallographic data for Cs_2NiO_2 obtained by Rietveld refinement.

Space Group, Z	$I4/mmmm$ (No. 139), 2
Temperature/K	298(5)
Cell parameters/Å	a = 4.4069(3)
	c = 13.561(1)
Cell Volume/Å^3	263.37(4)
Crystal density/g/cm^3	4.49
Wavelength/Å	Mo$K_{\alpha 1}$, λ = 0.559421
Range data collection ($2\theta/^o$	5–40
R_{Bragg}/%	2.02
R_p/%	7.46
R_{wp}/%	9.56

alkali anion in the structure of A_2NiO_2 (A = K, Rb, Cs) and the increasing size of the unit cell, the Ni–Ni distances are also expanded, with the consequence that the N*é*el temperature within this family of compounds is expected to be lowest for Cs_2NiO_2. In order to investigate the magnetic properties of Cs_2NiO_2, phase pure microcrystalline powder was synthesized. The phase purity of the powder was analyzed by the methods of X-ray powder analysis (Rietveld method), according to which the only second phase noticeable was silver in traces (< 1 %), due to the silver inlay. Rietveld plots of the refinement are shown in Figure 6.3, parameters related to the Rietveld refinements are given in Table 6.4.

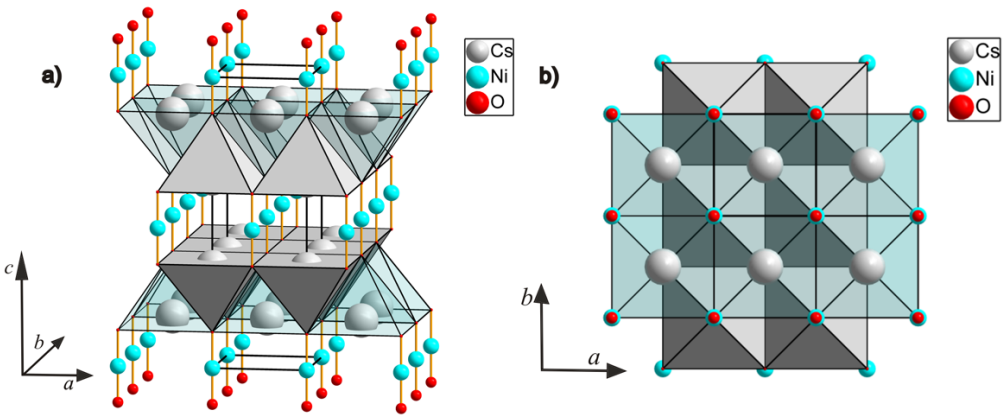

Figure 6.2.: Crystal structure of Cs_2NiO_2 presented in different views.

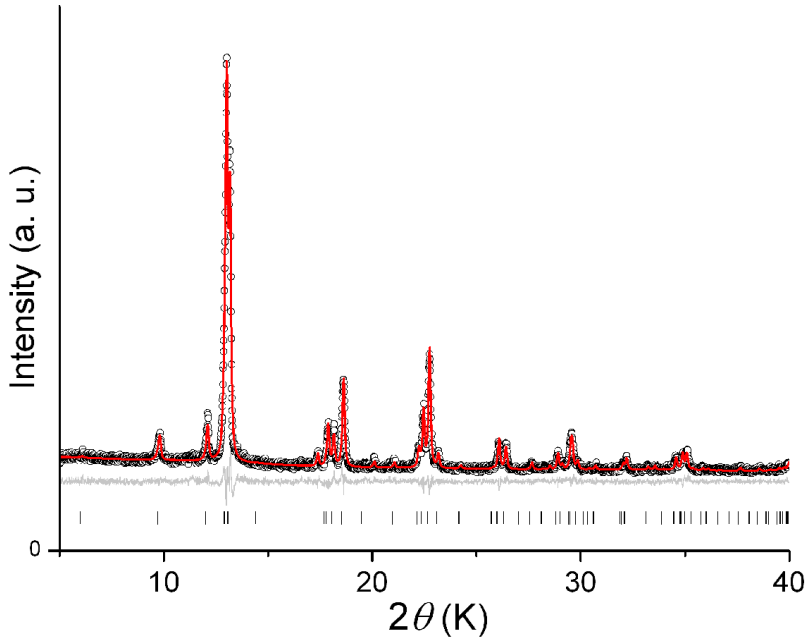

Figure 6.3.: Experimental and theoretical XRD pattern for Cs_2NiO_2; black marks: experimental, red: theoretical pattern. The difference between the experimental and theoretical pattern is given in gray. Bragg positions are given by thick marks.

6.1.3. Magnetic Measurements

The magnetic susceptibility of Cs_2NiO_2 was investigated at different strengths of magnetic field (1, 3, 5 and 7 T). Figure 6.4 presents the magnetic behavior of Cs_2NiO_2 corrected for diamagnetic contributions of the closed electronic shells [46]

and for traces of ferromagnetic impurities. A weak magnetic field dependency indicates the presence of small ferromagnetic impurities. Assuming a saturation of the magnetization of the ferromagnetic impurities a correction was made by plotting χ against 1/H and extrapolating linearly to 1/H = 0 (Honda-Owen plot). From the magnetic susceptibility data, it can be seen that above 20 K Cs_2NiO_2 exhibits paramagnetic behavior which can be well described according to the Curie-Weiss law. At 20 K, Cs_2NiO_2 orders antiferromagnetically.

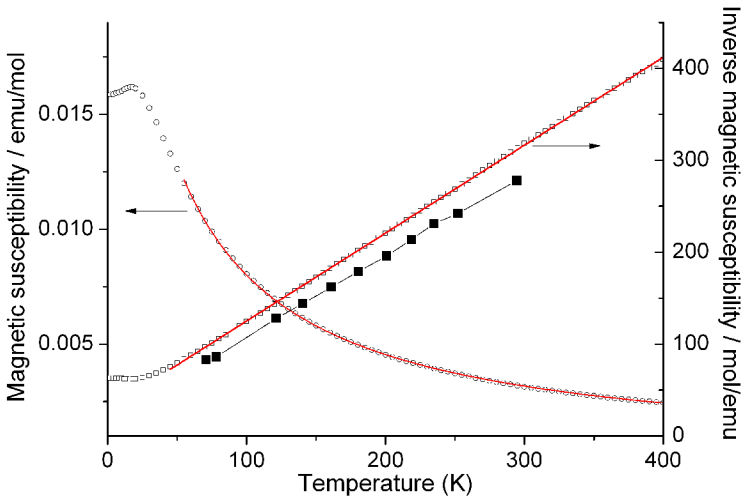

Figure 6.4.: Magnetic susceptibility and inverse magnetic susceptibility for Cs_2NiO_2. Red curves correspond to the fitting by the Curie-Weiss law. Black squares correspond to published data [1].

Even though the Ni–Ni distances are surprisingly large (4.4090 Å, Table 6.3), they are ruling out the direct interactions. An effective magnetic moment of $\mu = 2.89\ \mu_B$ ($\theta = -30.8$ K) was derived from the measurement in the highest magnetic field, which is in good agreement with a magnetic moment as expected for a d^8 free ion [46], including a slight orbital contribution, as well as with the magnetic susceptibility data obtained by Rieck and Hoppe [1]. The expected magnetic behavior for the Cs_2NiO_2, would be that it is a diamagnetic compound due to a distribution of d^8 electrons in the linear crystal field (Figure 5.9, $(xy,\ x^2{-}y^2)^4$,$(xz,\ yz)^4$,$(z^2)^0$). However, the antiferromagnetic ordering close to 20 K brings the new point of view in this observation.

In previous reports the electronic structure of K_2NiO_2 was determined with the help of spectroscopic studies of $[NiO_2{}^{2-}]$ in K_2NiO_2, as reported by Hitchmann

et.al [90]. In their course of research they found that the ground state of K_2NiO_2 corresponds to the electron configuration $(xy,\ x^2{-}y^2)^4$,$(xz,\ yz)^3$,$(z^2)^1$. These results can be also related to isostructural Cs_2NiO_2, whose Curie-Weiss fit from magnetic behavior results in the magnetic moment for a spin S = 1 contribution (μ = 2.89 μ_B).

Following this result, it can be assumed that peak broadening in Cs_2NiO_2 close to 20 K corresponds to antiferromagnetic ordering, which originates from the distribution of $3d^8$ electrons as in K_2NiO_2. Among the other members of the A_2NiO_2 family, only for Rb_2NiO_2 low temperature magnetic susceptibility data are available [89]. As a striking, still unresolved discrepancy with our result, no antiferromagnetic ordering for Rb_2NiO_2 has been observed [89].

7.

Synthesis and Characterization of new Quasi-One-Dimensional Alkali-metal oxometalates

Dimensionality plays a key role in solid state magnetism. Reduction of a systems dimensionality leads to various interesting physical properties which are usually explained using concepts from statistical mechanics and quantum mechanics. Applying three-dimensional theoretical models to lower dimensional systems is not at all trivial and tends to fail in many cases [93]. For instance, the separation of spin and charge excitations is a fascinating quantum feature related to the dimensionality of the system. The magnetism in three dimensions can be understood in the context of classical formalism. However, it is more challenging to understand the magnetic interactions in lower dimensions due the quantum effects. For example, quantum fluctuations are responsible for the absence of a long-range ordered state at finite temperatures in the two-dimensional $S = \frac{1}{2}$ Heisenberg antiferromagnet and in all one-dimensional quantum magnets [93].

Cuprate based insulators can be highlighted as the best realization of quantum magnets providing a wide variety of low-dimensional magnetic structures as well as wide spectrum of fascinating physical phenomena. With no doubt, the most prominent example is high temperature superconductivity in doped lanthanum cuprates exhibiting a two-dimensional substructure of CuO_4 units. The interplay between the magnetic and electric properties of cuprates has recently been the subject of intense research. Since theoretical methods are well established in one dimension,

compounds with quasi-one-dimensional structures are particulary suitable as model systems to obtain a detailed understanding of this interplay. Nevertheless, research on the effect of doping in copper oxide chain compounds has been limited due to the lack of materials that feature significant densities of holes in the chains. In the past few years, most of the attention was focused on the so-called "telephone number compounds" such as $(La,Sr)_{14-x}Ca_xCu_{24}O_{41}$ which contain the chain and ladder structural motives based on edge sharing CuO_4 plaquettes (Figure 7.1).

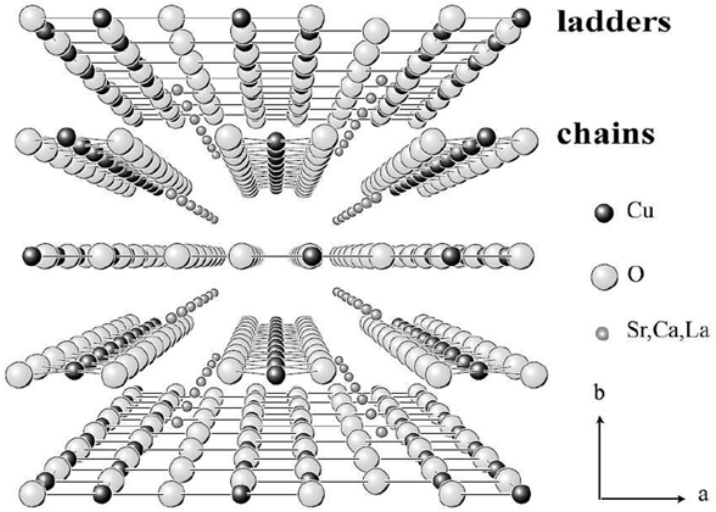

Figure 7.1.: Structure of the $(Sr,Ca,La)_{14}Cu_{24}O_{41}$ system.

For this type of compounds, experiments have revealed intricate charge and spin ordering patterns of the chains, which depend strongly on the degree of doping content. Although they possess interesting physical properties, the introduction of dopants to the lattice makes their structures rather complicated (Figure 7.1). The coexistence of two different structural motives (chain and ladder) adds additional complexity as a model. Structurally simpler quasi-one-dimensional copper oxides such as $CuGeO_3$ [94], $SrCuO_2$ [95], and Sr_2CuO_3 [96] have also been widely studied, but attempts to introduce mobile charge carriers into the copper oxide chains have thus far been unsuccessful.

Thanks to the recently developed azide/nitrate route for the synthesis of alkali-metal oxometalates a whole new series of quasi-one-dimensional compounds (Na_xCuO_2 [22] A_xMnO_2 [21]) has become accessible. Employing the route, a new family of $+2/+3$ mixed-valent quasi-one-dimensional oxomanganates $K_{29}Mn_{17}O_{34}$, $Rb_{11}Mn_8O_{16}$,

$Cs_4Mn_3O_6$ [21] and $Cs_3Mn_2O_4$ [97] have been successfully synthesized. The significance in the synthesis of these low-dimensional manganates arises from the mixed-valent manganates (III/IV), which are in the focus of research due to their colossal magnetoresistance properties they [98].

The discovery of a new class of copper oxides with quasi-one-dimensional structures such as $Na_3Cu_2O_4$, $Na_8Cu_5O_{10}$ and $Na_5Cu_3O_6$ reveals a new vantage point for a more detailed investigation of the interplay between magnetism and charge order in the cuprates. These compounds exhibit specific charge ordering patterns, which classify them as first clear manifestations of Wigner crystals [23, 99]. Furthermore, they are regarded as model systems for the cuprate superconductors.

In this chapter, a new quasi-one-dimensional alkali-metal oxocuprate(II,III) $K_3Cu_2O_4$, as well as new crystal structures of alkali-metal oxonickelates(II,III) are presented, together with the characterizations of their physical properties.

7.1. Synthesis and Physical Properties of New One-Dimensional oxocuprate $K_3Cu_2O_4$

In order gain more insights into the observations made on the sodium oxcuprates, analogous cuprate chain compounds containing potassium as a bigger alkali metal cation have been synthesiszed. From the potassium cuprates known so far (KCuO, K_3CuO_2 [53], $K_3Cu_5O_4$ [100], $KCuO_2$ [101], only $KCuO_2$ features one-dimensional $^1_\infty CuO_2$ chains. However, the oxidation state of copper in this compound is +3 and does not exhibit any unpaired spins. Here, the synthesis of $K_3Cu_2O_4$ is presented, together with the crystal structure determination and magnetic characterization. Magnetic data show $K_3Cu_2O_4$ as a one-dimensional AFM Heisenberg chain with uniform nearest neighbor spin interaction between Cu^{2+}–Cu^{2+} cations, viz. between next-nearest neighboring copper sites along the $^1_\infty CuO_2$ strand.

Parts of this chapter are included in the publication "Synthesis, Crystal Structure, and Physical Properties of the New Chain Alkalioxocuprate $K_3Cu_2O_4$" [2].

7.1.1. Synthesis, Thermal Analysis and X-ray Powder Diffraction

Starting materials for the preparation of the potassium cuprate were potassium azide, potassium nitrate (Riedel-De Haen AG Seelze, Hannover, 99.5 %) and CuO. The synthesis of CuO and KN_3 has been described in the chapter 4.3.2 and 4.1, respectively. The starting compounds were dried under vacuum (10^{-3} mbar) at 393 K overnight, mixed thoroughly in an agate mortar in a ratio according to equation 7.1, and placed under argon in a closed steel container, provided with a silver inlay.

$$7KN_3 + 2KNO_3 + 6CuO \rightarrow 3K_3Cu_2O_4 + 23/2N_2 \tag{7.1}$$

Black needle-shaped single crystals of $K_3Cu_2O_4$ were obtained when the following temperature schedule was applied 298 → 533 K (100 K/h), 533 → 673 K (5 K/h), 673 → 923 K (600 K/h), and subsequent annealing for 50 h at 923 K.

Although the azide nitrate route was shown to be successful in obtaining the $K_3Cu_2O_4$ single crystals of sufficiently good quality for structural analysis (Figure 7.2), the obtained product always contained potassium cuprates(I) in addition. Synthesis of the phase pure powder was necessary in order to investigate the physical

properties. To overcome this difficulty the synthesis of single phase $K_3Cu_2O_4$ powder mentioned, an alternative approach was chosen according to equation 7.2. Phase pure $KCuO_2$ was prepared according to the route proposed in [101] and K_2O was prepared from purified potassium by oxidation with molecular oxygen [102].

$$K_2O + KCuO_2 + CuO \rightarrow K_3Cu_2O_4 \tag{7.2}$$

Mixtures, including 2 mol. % excess of K_2O, were transferred to a gold ampoule, closed under argon atmosphere and treated at 723 K for 30 h. The obtained black powder, being very sensitive to air and moisture, was sealed and stored in glass ampoules under argon atmosphere, and all further handling was made in an inert atmosphere of purified argon. The collected powder diffraction pattern for $K_3Cu_2O_4$ is shown in Figure 7.3, and the results obtained from the Rietveld refinement are given in Table 7.1. For the Rietveld refinement atomic coordinates obtained from the single crystal analysis were used.

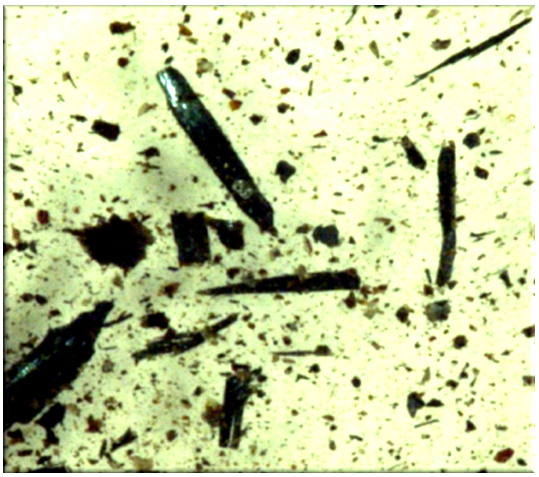

Figure 7.2.: Single crystals of $K_3Cu_2O_4$.

The thermal analysis of $K_3Cu_2O_4$ (Figure 7.4) did not reveal any chemical reaction or phase transformation during heating up to 923 K, where decomposition occurs.

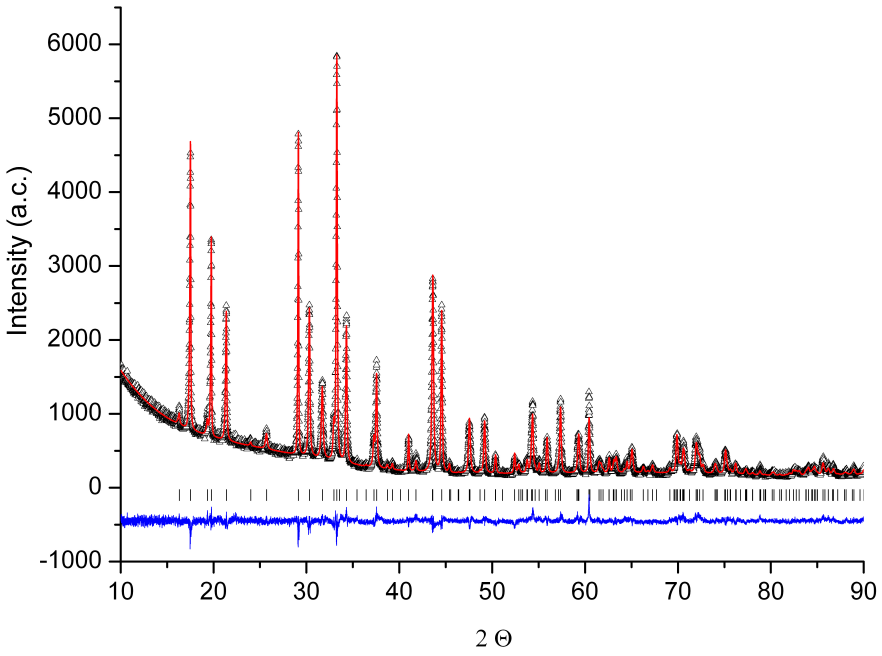

Figure 7.3.: X-ray powder diffraction data of $K_3Cu_2O_4$, observed (triangles), theoretical pattern (grey solid line) and difference between experimental and calculated patterns (underneath line). Bragg positions used to calculate the theoretical pattern of $K_3Cu_2O_4$ are marked by ticks.

Table 7.1.: Crystallographic data for $K_3Cu_2O_4$ obtained from Rietveld refinement.

Space Group, Z	$Cmcm$(No. 63), 2
Temperature/K	298(5)
Cell parameters/Å	$a = 6.1234(1)$
	$b = 8.9826(2)$
	$c = 10.8620(2)$
Cell Volume/Å^3	597.46(4)
Crystal density/g/cm^3	3.42
Wavelength/Å	Cu$K_{\alpha 1}$, $\lambda = 1.540598$
Range data collection ($2\theta/^o$	10–90
R_{Bragg}/%	3.27
R_p/%	4.86
R_{wp}/%	6.56

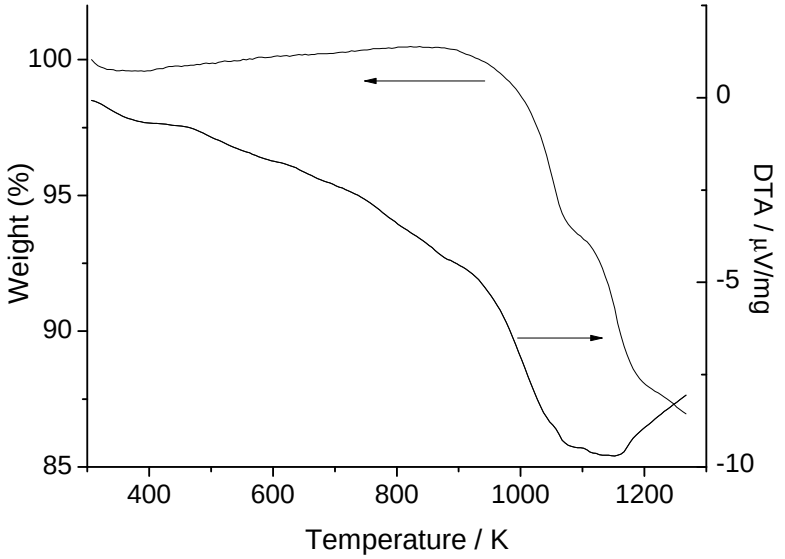

Figure 7.4.: Thermal analysis of $K_3Cu_2O_4$.

7.1.2. Single Crystal Analysis and Crystal Structure Description

The crystal structure of $K_3Cu_2O_4$ was determined from single crystal data collected at room temperature. It was found that $K_3Cu_2O_4$ crystallizes orthorhombic in the space group *Cmcm* (No.63) [2]. Details and results of the single crystal structure refinement are given in Tables 7.2– 7.4. Interatomic distances and coordination numbers (CN), for $K_3Cu_2O_4$ are presented in Table 7.5.

Single crystal analysis revealed that $K_3Cu_2O_4$ is isostructural to $K_3Ni_2O_4$ and $K_3Pt_2O_4$ [103], and shows a fully charge ordered copper partial structure. The most prominent structural feature are wave-like one-dimensional $^1_\infty CuO_2$ chains which are constructed from planar, edge-sharing CuO_4 units (Figure 7.5). From the structural analysis of the Cu–O bond lengths, valence states of either +2 or +3 can be precisely assigned to each copper atom (d(Cu^{2+}–O) = 1.939(3) Å, (d(Cu^{3+}–O) = 1.851(3) Å). The one-dimensional chains in $K_3Cu_2O_4$ are extended along the *c*-axis, where the O–Cu–O angles in the CuO_4 square units are diverging from the ideal 90 ° due to variation of oxidation states of copper, as well as due to the way, how these units are connected. The dihedral angle between two CuO_4 square units is 155.7 °. This is

Table 7.2.: Crystal data and structure refinement data for $K_3Cu_2O_4$.

Space Group, Z	$Cmcm$, 4
Cell parameters/Å	$a = 6.1275(4)$
	$b = 8.9908(7)$
	$c = 10.8708(8)$
Temperature/K	298(2)
Cell Volume/Å^3	598.88(8)
M_r/g/mol	308.38
Calculated density/g/cm^3	3.42
Crystal form, color	Needle, black
Crystal size/mm	0.25 × 0.10 × 0.08
Difrfractometer	Bruker AXS, APEX SMART CCD
Monochromator	Graphite
X-ray radiation/$\lambda/\AA$	Mo-K_α, 0.71073
θ range/^{o}	3.42 to 36.85
Index range	$-9 \leq h \leq 9$
	$-14 \leq k \leq 14$
	$-17 \leq l \leq 17$
Absorption correction	Multi-scan, SADABS [81]
Total no. reflections, N_{all}	4609
Independent reflections N	725
Reflections with $I > 2\sigma(I)$, $\acute{N}$	704
Absorption coefficient/μ/mm^{-1}	9.110
$F(000)$	588
Refinement method	Full matrix least-squares on F^2
Weighting Scheme	$w = 1/[\sigma^2(Fo^2) + (0.0190P)^2 + 8.8769P]$ where $P = ({F_0}^2 + 2{F_c}^2)/3$
Goodness-on-fit on F^2	1.376
R_1 ($\acute{N}$, N)	0.0429; 0.0439
wR_2 ($\acute{N}$, N)	0.1066; 0.1070

in contrast to the sodium cuprates ($Na_{1+x}CuO_2$) obtained also by the azide nitrate route, where the $^1_\infty CuO_2$ chains are nearly flat with dihedral angles between two CuO_4 square units approaching 180°.

The one-dimensional $^1_\infty CuO_2$ chains are distributed among the honey-comb lattice of potassium ions (Figure 7.5). The potassium ions occupy two crystallographically independent sites, exhibiting different coordination environment (Figure 7.6). K1 with the coordination number 6, connects three $^1_\infty CuO_2$ chains, maintaining bonds to two oxygen atoms from each chain forming distorted prism (Figure 7.6). K2 is

Table 7.3.: Atomic coordinates and isotropic displacement parameters / Å^2 for $K_3Cu_2O_4$.

Atom	Site	x	y	z	U_{eq}
Cu1	4a	0	0	0	0.0165(2)
Cu2	4c	0	0.0607(1)	1/4	0.0148(2)
K1	8f	0	0.3476(2)	0.0676(1)	0.0236(3)
K2	4c	0	0.6943(2)	1/4)	0.0226(3)
O1	16h	0.2952(5)	0.4377(4)	0.8859(3)	0.0234(6)

Table 7.4.: Anisotropic displacement parameters /$\times 10^{-2}$ /Å^2 for $K_3Cu_2O_4$.

Atom	U_{11}	U_{22}	U_{33}	U_{23}	U_{13}	U_{12}
Cu1	1.15(4)	2.41(4)	1.39(4)	0	0	–0.37(3)
Cu2	1.27(4)	1.69(4)	1.49(4)	0	0	0
K1	1.98(5)	2.38(5)	2.74(6)	0	0	0.055(5)
K2	1.69(7)	2.59(8)	2.49(8)	0	0	0
O1	1.2(1)	4.2(2)	1.7(1)	–0.2(1)	–0.1(1)	–0.7(1)

Table 7.5.: Interatomic distances (in Å) and coordination numbers (CN) for $K_3Cu_2O_4$.

Atom	O	CN
Cu1	1.851	4
Cu2	1.938	4
K1	2.693	6
	2.798	
	2.901	
K2	2.619	4
CN	6	

equidistant to 4 oxygen atoms of two neighboring $^1_\infty CuO_2$ chains, forming a pyramid where K2 is situated on the top of the pyramid.

7.1.3. EPR-Spectroscopy

In order to determine the g-factor, the EPR measurements were carried out on $K_3Cu_2O_4$ polycrystalline samples. Figure 7.7 presents the EPR-spectrum obtained, which is typical for a compound containing Cu^{2+} coordinated by an elongated oc-

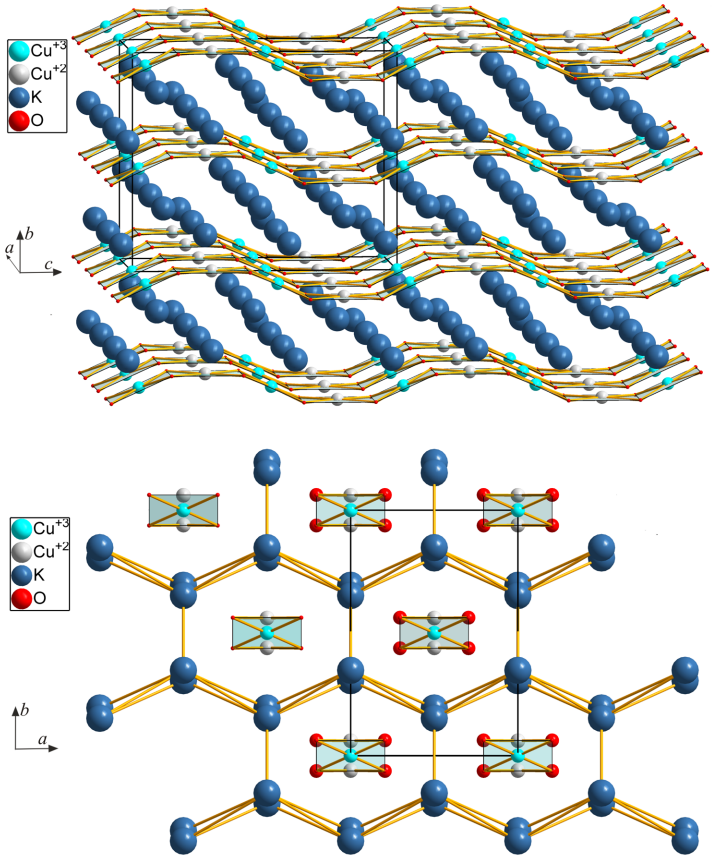

Figure 7.5.: Crystal structure of $K_3Cu_2O_4$.

tahedron of oxygen atoms.

The principal g-factors are found to be:

$g_\perp$=2.06 and $g_\parallel$ = 2.21

giving an average powder g-factor of:

$$g_{pwd} = \frac{2g_\perp + g_\parallel}{3} = 2.12 \tag{7.3}$$

7.1.4. Magnetic Measurements

The magnetic susceptibility of $K_3Cu_2O_4$ was measured at different strengths of magnetic fields in the range from 1 to 7 T, where it was found that they are independent on the field strength in the temperature range 15 - 400 K, indicating paramagnetic behavior and negligible saturation of ferro- or ferrimagnetic impurities.

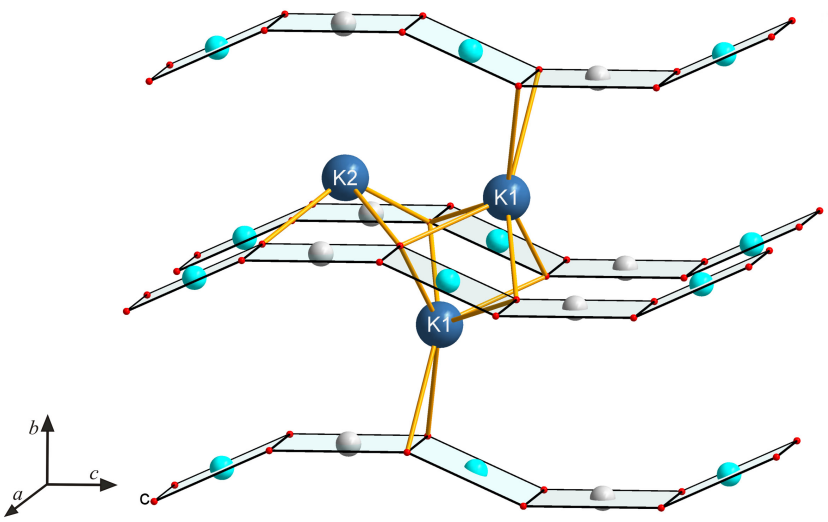

Figure 7.6.: Coordination environments for K1 and K2 ions in $K_3Cu_2O_4$.

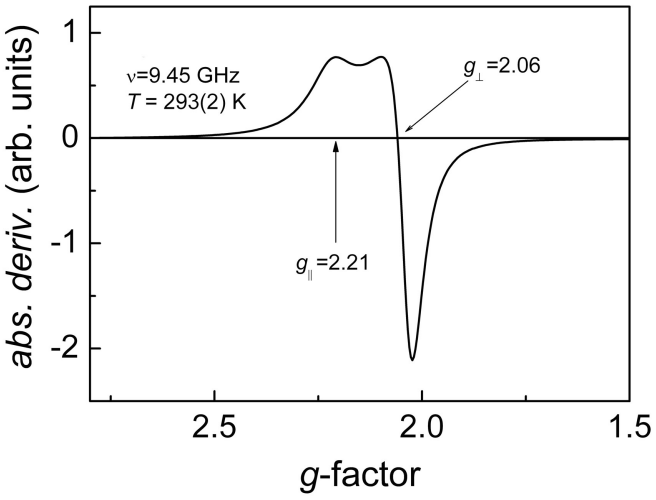

Figure 7.7.: Room temperature X-band EPR powder spectrum of $K_3Cu_2O_4$ with principal g-factors indicated. Measurements and interpretation were made by Dr. R. Kremer [2].

The low-temperature susceptibility features a broad maximum centered close to 65 K, which is a strong indication of the antiferromagnetic short range ordering consistent with the low-dimensional behavior as expected from the crystal structure.

The high temperature susceptibility (at T $\geq$ 200 K) can be fitted with the modified Curie-Weiss law (Figure 7.8), consisting of the temperature dependent susceptibility

$\chi_{spin}(T)$ and the temperature independent contribution χ_0:

$$\chi(T) = \chi_{spin}(T) + \chi_0 \tag{7.4}$$

where the spin susceptibility is :

$$\chi_{spin} = \frac{C}{T - \theta} \tag{7.5}$$

with the Curie constant:

$$C = \frac{N_A g^2 \mu_B^2 S(S+1)}{3k_B} \tag{7.6}$$

and the Curie-Weiss temperature θ. The temperature independent susceptibility χ_0 contains the diamagnetic susceptibilities of the closed shells, which are according to Selwood [104] summed up to –110×10^{-6} cm^3/mol, and the Van Vleck contribution which are positive and of the same order of magnitude as the diamagnetic contributions. The van Vleck contributions can be estimated from the energy differences of the orbitals and the spin-orbit coupling constant and are found to be typically of the order of the diamagnetic contribution (40–60 × 10^{-6} cm^3/mol). In the fitting equation the fitting parameters g, χ_0 and θ are strongly correlated, and meaningful results cannot be obtained without fixing one of them [105]. χ_0 was used as a fitting parameter and checked for its consistency. During fitting, the g-factor was fixed to the powder average of 2.12 as determined in the EPR measurements. Fitting in this way results in the following parameters: θ = –105(1) K; χ_0 = –4(7)×10^{-7} cm^3/mol; g = 2.12; μ_{eff} = 1.84 μ_B. The negative Curie-Weiss temperature is an indication for predominantly antiferromagnetic interactions. The refined value for χ_0 is in good agreement with the expected value compensated by the diamagnetic and the Van-Vleck temperature independent susceptibility.

Heisenberg model - Measurements and interpretation were made by Dr. R. Kremer [2]

The low dimensional behavior was also analysed in terms of a linear chain Heisenberg model. In this work the fittings were performed with the spin S = 1/2 antiferro-

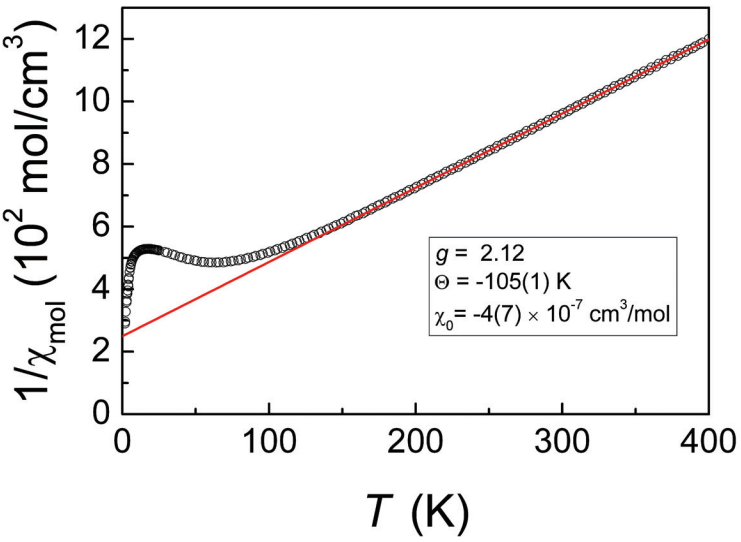

Figure 7.8.: Inverse magnetic susceptibility and CurieWeiss fit (red line) for $K_3Cu_2O_4$.Measurements and interpretation were made by Dr. R. Kremer [2].

magnetic (AF) Heisenberg Hamiltonian:

$$\mathcal{H} = \sum_{ij} J(i,j) S_i \cdot S_j \tag{7.7}$$

where J_{ij} is the Heisenberg exchange interaction between spins S_i and S_j and the sum is over unique exchange bonds. J_{ij} will be assumed to be only relevant for nearest neighbors and is denoted as J_{nn}.

To account for a diverging contribution of a Curie-type of susceptibility of impurities (Curie tail), we subtracted from the experimental susceptibility a Curie contribution of $\sim$ 1 % spin S = 1/2 entities and obtained $\chi^*(T) = \chi_{exp}(T)$-$\chi_{imp}$ where $\chi^*(T)$ was fitted to an equation $\chi(T) = f\chi_{spin}(T)$-$\chi_0$, where $\chi_{spin}(T)$ is given by the susceptibility of a S = 1/2 Heisenberg model as proposed by Johnston [106]. In addition to this model, the linear scaling factor f (0.784(4)) was added as a necessity to obtain appropriate fits. Divergence from the ideal fit can be due to the wave-like nature of the linear $^1_\infty CuO_2$ chains. During the fitting, the g-factor has been fixed to the powder average determined from the EPR experiment [60].

The experimental data can be well described by a uniform Heisenberg chain with an AFM nearest-neighbor Cu^{2+}–Cu^{2+} intrachain interaction J_{nn} of $\sim$ 101 K (Figure 7.9). The broad short-range ordering maximum peak at $\sim$ 65 K is in good agreement

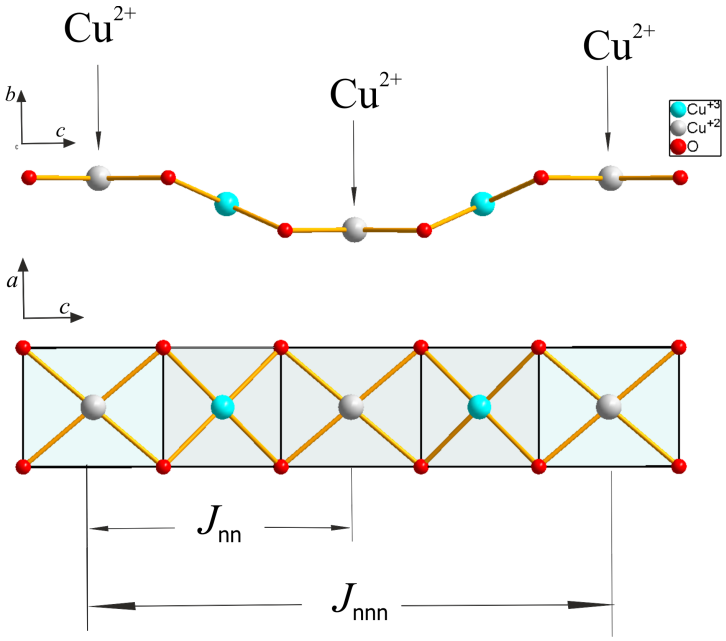

Figure 7.9.: Presentation of the J_{nn} (nearest neighbor intrachain interaction) and J_{nnn} (next nearest neighbor intrachain interaction) in $K_3Cu_2O_4$.

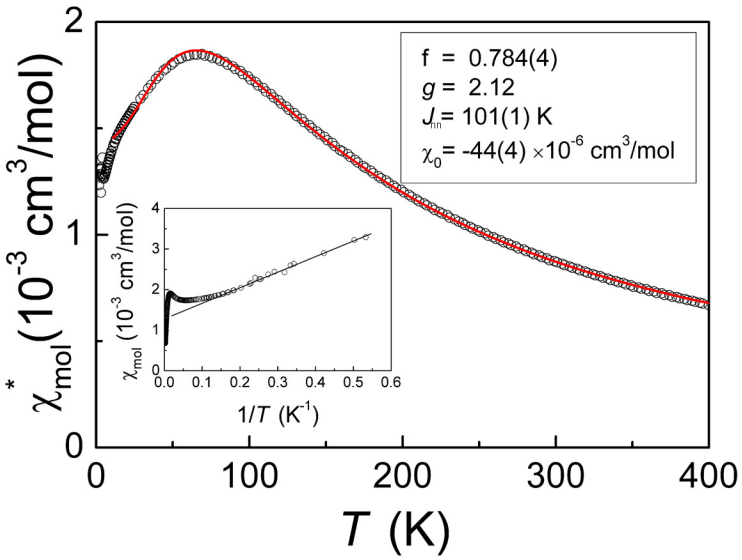

Figure 7.10.: (Main frame) Magnetic susceptibility of $K_3Cu_2O_4$ (o) fitted to the susceptibility of a S = 1/2 Heisenberg chain with uniform nearest-neighbour $Cu^{2+}Cu^{2+}$ intrachain spin exchange interaction (solid line).The lower inset displays the (uncorrected) susceptibility of $K_3Cu_2O_4$ (o) vs. the inverse temperature. Measurements and interpretation were made by Dr. R. Kremer [2].

with the ratio $T_{max}/J = 0.6408$ as given by Johnston *et al* [106].

There is, however, disagreement between the magnitudes of the experimental and computed susceptibilities at T_{max}. Theoretically, one expects a value which is about 20 % higher than the one found in experiment. Efforts to attribute this discrepancy to an additional next-nearest neighbour intrachain spin exchange interaction (J_{nnn}) by introducing a mean field type renormalisation of the susceptibility were not conclusive. A comparison of the experimental data with the exact diagonalisation results by Heidrich-Meissner et al. [107] indicated a ratio of $-0.25 < \alpha = J_{nnn}/J < 0.25$, with a clear preference to $\alpha \approx 0$, i.e. negligible next-nearest neighbour interaction. This results supports the fit of the spin susceptibility with a nearest neighbour Heisenberg chain model and proves the non-magnetic state of the Cu^{3+} cations.

7.1.5. Specific Heat Measurements

The heat capacity of $K_3Cu_2O_4$ is presented in Figure 7.11 in log-log plot, where it is shown that there is no indication of long-range magnetic ordering at low temperatures with a λ-type anomaly. However, there are some small deviations from a T^3-Debye law at low temperatures, most likely due to magnon contributions to the heat capacity.

Following the analysis of the magnetic susceptibility, we can assume that for a Heisenberg chain at temperatures T small compared to the intrachain spin exchange, J_{intra}, the magnon contributions are linear in T and can be represented by:

$$C_{mag} = \frac{2}{3} R \frac{T}{J_{intra}} \tag{7.8}$$

where R is the molecular gas constant. With J_{intra} as found from the analysis of the magnetic susceptibility, one expects $C_{mag}/T \sim 0.055$ J/molK^2 which is in fair agreement with the observed value of ~ 0.03 J/molK^2 [2].

7.1.6. Discussion

When $K_3Cu_2O_4$ is compared with the other one-dimensional sodium cuprates synthesized along the azide/nitrate route ($Na_3Cu_2O_4$, $Na_8Cu_5O_{10}$, $Na_5Cu_3O_6$), it can be seen that substitution of a potassium ion influences the dihedral angles between adjacent CuO_4 square units, which leads to the formation of undulating $^1_\infty CuO_2$

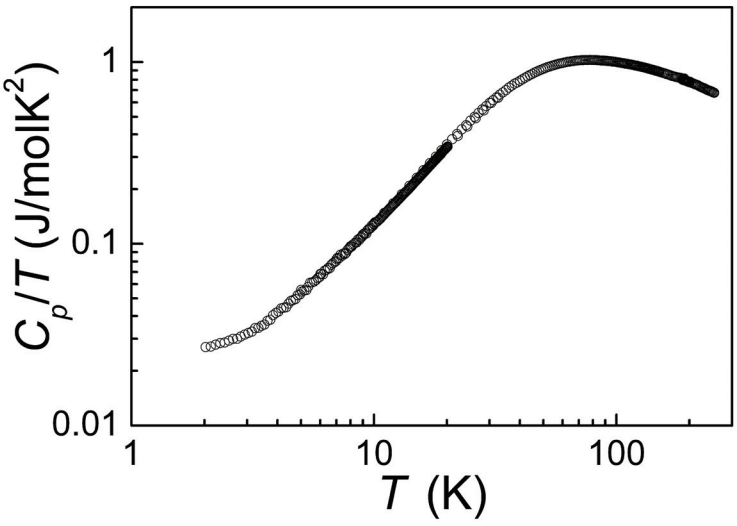

Figure 7.11.: Specific heat measurements for $K_3Cu_2O_4$. Measurements and interpretation were made by Dr. R. Kremer [2].

chains in $K_3Cu_2O_4$. The new oxocuprate(II,III) $K_3Cu_2O_4$ can be realized as a member of the compositional series $K_{1+x}CuO_2$ with x = 0.5, and with the end member $KCuO_2$ (x = 0) [101].

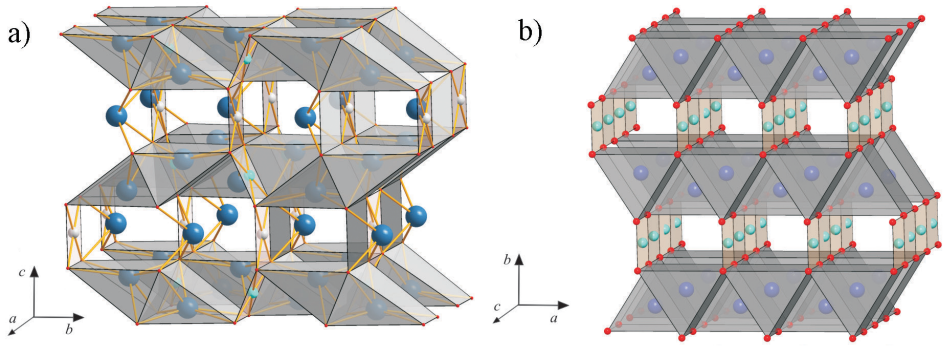

Figure 7.12.: Comparison of the crystal structures of (a) $K_3Cu_2O_4$ and (b) $KCuO_2$.

Structurally, both compounds have comparable chain arrangements as well as nearly the same distribution of cation sites which are filled with potassium ions in different ways (Figure 7.12). As can be seen from the figures, the potassium ions form layers of trigonal prisms, where its repetition in both compounds is different. In $KCuO_2$, in the layer, each second void is empty, and in $K_3Cu_2O_4$ each third and fourth. K2 atoms in $K_3Cu_2O_4$ can be incorporated between the $^1_\infty CuO_2$ chains, due

to their different orientation and distribution as in $KCuO_2$.

$K_3Cu_2O_4$ is isostructural to $K_3Ni_2O_4$ and $K_3Pt_2O_4$ [103] and the shortest Cu–Cu distance between two $^1_\infty CuO_2$ chains is $\sim$ 5.4 Å, which is in agreement with the respective value in $K_3Ni_2O_4$. In $K_3Pt_2O_4$, these distances are just slightly higher (5.5 A). Although all three compounds have the same chain arrangement, and contain transition metal ions with unpaired spins, only $K_3Cu_2O_4$ shows low-dimensional magnetic behaviour.

The analysis of the magnetic susceptibility proves that $K_3Cu_2O_4$ realizes a S = 1/2 chain system. Inclusion of nearest neighbor spin-exchange interactions suffices to describe the temperature dependence of the susceptibility adequately. There is no indication for sizeable next-nearest neighbor interactions. In view of the crystal structure, which indicates an ordered Cu^{3+}–Cu^{2+}–Cu^{3+}–Cu^{2+} arrangement along the chain, the nearest-neighbor spin exchange couples Cu^{2+} entities (Figure 7.9). The magnitude of the spin exchange interaction is somewhat lower than the one found for the analogue compound $Na_3Cu_2O_4$ (about 40 %). Like for $Na_3Cu_2O_4$, next-nearest neighbor spin exchange (J_4 in the notation of [14]) appears to be negligible. It amounted to about 10 % for $Na_3Cu_2O_4$. In contrast to $Na_3Cu_2O_4$, which exhibits long-range ordering at $\sim$ 23 K, [108] according to our heat capacity data $K_3Cu_2O_4$ shows no indication of long-range three-dimensional magnetic ordering down to 2 K. This can be understood as due to the increased interchain interaction through the shortest Cu–Cu distances in $K_3Cu_2O_4$, $\sim$ 5.4 Å as compared to $\sim$ 4.2 Å in $Na_3Cu_2O_4$. Additionally, as already pointed out by Horsch et al., [99] the interchain coupling is strongly affected by geometrical frustration, which can suppress long-range ordering, since the $^1_\infty CuO_2$ chains are arranged in a honeycomb lattice in the a,b plane (Figure 7.5). There is an apparent discrepancy between the high-temperature behavior of the magnetic susceptibility, characterized by a Curie-Weiss temperature of $\sim$ 105 K and a g-factor of 2.12, and the low-temperature behaviour, which is in good agreement with the susceptibility of a S = 1/2 Heisenberg chain with nearest-neighbour AFM spin interaction. The spin-exchange found by fitting the susceptibility to the Heisenberg chain theory indicates an AFM spin-exchange of $\sim$ 101 K. This leads, in case of a uniform chain with two neighbors for each spin, to a Curie-Weiss temperature of

$$\theta = \frac{1}{3} z J S(S+1) \tag{7.9}$$

where z presents the number of nearest neighbors (2), and thus giving the result of the Weiss constant a value of $\theta = -J_{nn}/2 \sim 50$ K. The respective required interchain interactions appear to be too small to move this value significantly towards the Curie-Weiss temperature found by fitting the high-temperature susceptibility. Such large interchain interactions would lead to long-range ordering at elevated temperatures, which has not been observed experimentally.

7.2. Synthesis and Physical Properties of New One-Dimensional Oxonickelate $K_4Ni_3O_6$

7.2.1. Synthesis, Thermal Analysis and X-ray Powder Diffraction

Starting materials in the preparation of the potassium nickelate were potassium azide, potassium nitrate (Riedel-De Haen AG Seelze, Hannover, 99.5 %) and NiO. The synthesis of NiO and KN_3 has been described in the section 4.3.1 and 4.1, respectively. The starting compounds were dried under vacuum (10^{-3} mbar) at 393 K overnight, mixed thoroughly in an agate mortar in a ratio according to equation 7.10, and placed under argon in a closed steel container, provided with a silver inlay.

$$7KN_3 + 2KNO_3 + 6NiO \rightarrow 3K_3Ni_2O_4 + 23/2N_2 \tag{7.10}$$

$$4K_3Ni_2O_4 + NiO + \frac{1}{2}O_2 \rightarrow 3K_4Ni_3O_6 \tag{7.11}$$

A powder sample containing $K_3Ni_2O_4$ was obtained according to equation 7.10, when the following temperature profile was applied: 298 → 533 K (100 K/h), 533 → 673 K (5 K/h), 673 → 873 K (600 K/h), and subsequent annealing for 30 h at 873 K (reaction 7.10). The sample was transferred to a silver crucible, sealed in a quartz ampoule under argon atmosphere and additionally annealed at 873 K for 500 h where the $K_3Ni_2O_4$ single crystals were obtained. However, due to the longer annealing, NiO was left in the mixture with $K_3Ni_2O_4$. The batch obtained (with the single crystals of $K_3Ni_2O_4$ and NiO) was transferred to a corundum crucible and treated in an oxygen stream at 873 K for 100 h (reaction 7.11), which led to the formation of $K_4Ni_3O_6$ single crystals.

The thermal analysis revealed that the product $K_4Ni_3O_6$ is stable up to ∼ 923 K. The obtained powder samples were checked for the purity and were characterized by the means of X-ray diffraction, where for the Rietveld refinement (Figure 7.13) the coordinates from the single crystal solution were used. The details obtained from the Rietveld refinement are given in the Table 7.6.

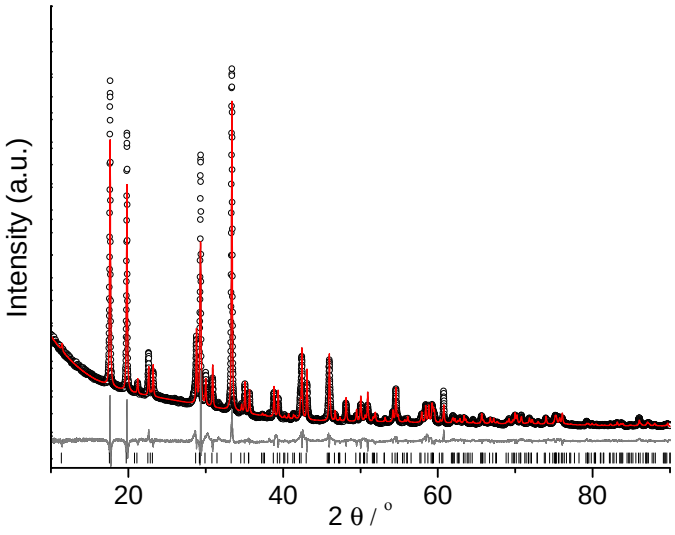

Figure 7.13.: X-ray powder diffraction data of $K_4Ni_3O_6$, observed (circles),theoretical pattern (grey solid line) and difference between experimental and calculated patterns (underneath line). Bragg positions used to calculate the theoretical pattern of $K_4Ni_3O_6$ are marked by ticks..

Table 7.6.: Crystallographic data for $K_4Ni_3O_6$ obtained from Rietveld refinement.

Space Group, Z	$C2/m$, 4
Temperature/K	298(5)
Cell parameters/Å	$a = 8.9660(3)$
	$b = 6.1027(2)$
	$c = 7.7877(2)$
	$\beta = 91.662(2)$
Cell Volume/Å^3	427.37(2)
Crystal density/g/cm^3	3.33
Wavelength/Å	Cu$K_{\alpha 1}$, $\lambda = 1.540598$
Range data collection ($2\theta/^o$	10–90
R_{Bragg}/%	7.73
R_p/%	5.13
R_{wp}/%	8.10

7.2.2. Single Crystal Analysis and Crystal Structure Description

Single crystal analysis revealed that $K_4Ni_3O_6$ crystallizes in the monoclinic space group $C2/m$. The details of the structure refinement are given in Table 7.7 – 7.9. The most prominent structural feature are one-dimensional $^1_\infty NiO_2$ chains (Figure 7.14). The elementary building block of the chains are square planar NiO_4 units. From the analysis of Ni–O distances it was not possible to deduce the oxidation state of nickel to +2 or +3 (dNi1–O = 1.8524 Å, dNi2–O = 1.8389 Å). However, from the crystallographic point of view, due to electroneutrality, Ni1 being on the position $2a$ suggests an oxidation state to +2, and the Ni2 being on the position $4i$ suggests an +3 oxidation state, respectively.

Along the $^1_\infty NiO_2$ chain, every Ni^{3+}–O_4 is connected through edge sharing with one Ni^{2+}–O_4 (dihedral angle 139.3°) and another Ni^{3+}–O_4 unit (dihedral angle 180°), whereas every Ni^{2+}–O_4 unit connects to two Ni^{3+}–O_4 units.

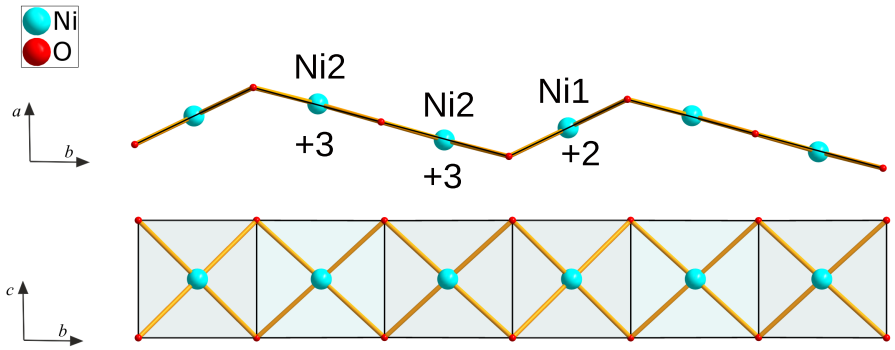

Figure 7.14.: Presentation of a $^1_\infty NiO_2$ chain in $K_4Ni_3O_6$.

The one-dimensional chains are aligned in a honey-comb lattice of potassium ions (Figure 7.15). The potassium ions occupy two independent crystallographic sites K1 and K2, both of which are coordinated by 6 O atoms, forming trigonal prisms. Figure 7.16 shows that these prisms are ordered as double layers in the structure; these double layers of K1 and K2 atoms can be easily distinguished: The K1 double layers have their prisms connected through faces and edges, while the prism of the K2 double layers are connected to each other only by face sharing.

Table 7.7.: Crystal data and structure refinement data for $K_4Ni_3O_6$.

Space Group, Z	$C2/m$, 2
Cell parameters/Å and °	a = 8.9933(14) b = 6.1010(10) c = 7.7910(13) β = 91.660(2)
Temperature/K	298(2)
Cell Volume/Å^3	427.30(12)
M_r/g/mol	428.53
Calculated density/g/cm^3	3.33
Crystal form, color	Needle, black
Crystal size/mm	0.24 × 0.16 × 0.12
Difrfractometer	Bruker AXS, APEX SMART CCD
Monochromator	Graphite
X-ray radiation/$\lambda/\mathring{A}$	Mo-K_α, 0.71073
θ range/^{o}	2.62 to 34.84
Index range	– 14 ≤ h ≤ 14 0 ≤ k ≤ 9 0 ≤ l ≤ 12
Absorption correction	Multi-scan, TWINABS [109]
Total no. reflections, N_{all}	4813
Independent reflections N	1762/ R(int)=0.043
Reflections with $I > 2\sigma(I)$, $\acute{N}$	1712
Absorption coefficient/μ/mm^{-1}	8.474
F(000)	416
Refinement method	Full matrix least-squares on F^2
Weighting Scheme	$w = 1/[\sigma^2(Fo^2) + (0.0533P)^2 + 0.7878P]$ where $P = ({F_0}^2 + 2{F_c}^2)/3$
Goodness-on-fit on F^2	1.120
R_1 ($\acute{N}$, N)	0.0297; 0.0304
wR_2 ($\acute{N}$, N)	0.0871 ; 0.0877

Table 7.8.: Atomic coordinates and isotropic displacement parameters / Å^2 for $K_4Ni_3O_6$.

Atom	Site	x	y	z	U_{eq}
Ni1	2a	0	0	0	0.0013(1)
Ni2	4i	0.0372(1)	0	0.3309(1)	0.0014(1)
K1	4i	0.3205(1)	0	0.6251(1)	0.0021(1)
K2	2a	0.3507(1)	0	0.1098(1)	0.0025(1)
O1	4d	0.0706(1)	0.2012(2)	0.1581(2)	0.0017(1)
O2	2a	0	0.2000(4)	1/2	0.0030(1)

Table 7.9.: Anisotropic displacement parameters /Å^2 ∓ 10^3 for $K_4Ni_3O_6$.

Atom	U_{11}	U_{22}	U_{33}	U_{23}	U_{13}	U_{12}
Ni1	17(1)	10(1)	13(1)	0	-2(1)	0
Ni2	18(1)	10(1)	15(1)	0	4(1)	0
K1	23(1)	16(1)	23(1)	0	-2(1)	0
K2	18(1)	20(1)	39(1)	0	5(1)	0
O1	26(1)	11(1)	14(1)	0(1)	-2(1)	0
O2	53(1)	14(1)	23(1)	0	19(1)	0

Table 7.10.: Interatomic distances (in Å), and coordination numbers (CN) for $K_4Ni_3O_6$. Lattice constants from the powder data were used.

	O	CN
Ni1–O1	1.838	4
Ni1–O1	1.838	
Ni1–O1	1.838	
Ni1–O1	1.838	
Ni2–O1	1.852	4
Ni2–O1	1.852	
Ni2–O2	1.834	
Ni2–O2	1.834	
K1–O1	2.652	6
K1–O1	2.652	
K1–O2	2.645	
K1–O2	2.645	
K1–O2	3.246	
K1–O2	3.246	
K2–O1	2.704	6
K2–O1	2.704	
K2–O1	2.830	
K2–O1	2.830	
K2–O1	2.874	
K2–O1	2.874	

7.2.3. Magnetic Measurements

The magnetic susceptibility data of $K_4Ni_3O_6$ were collected at different magnetic field intensities (0.1–7 T), where it was found that the susceptibility is independent of field strength in the temperature range 20–400 K, indicating paramagnetic behavior in this temperature range. The magnetic susceptibility is characterized by a

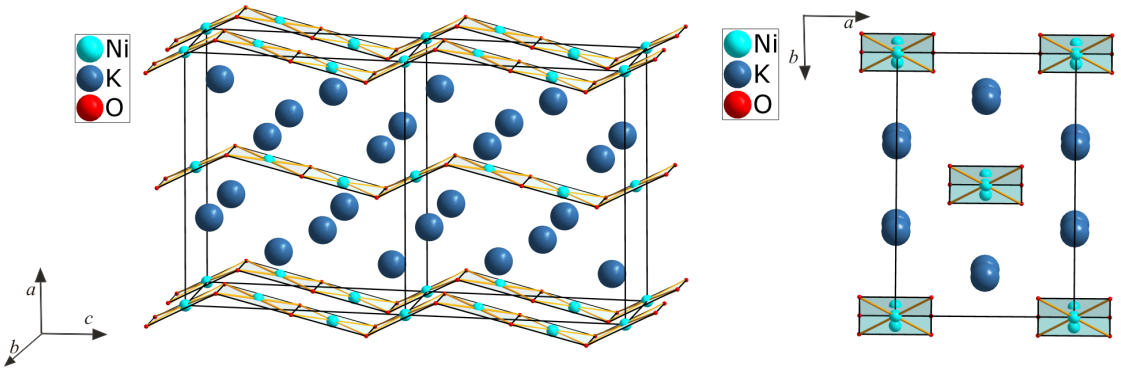

Figure 7.15.: Different crystal projection of $K_4Ni_3O_6$.

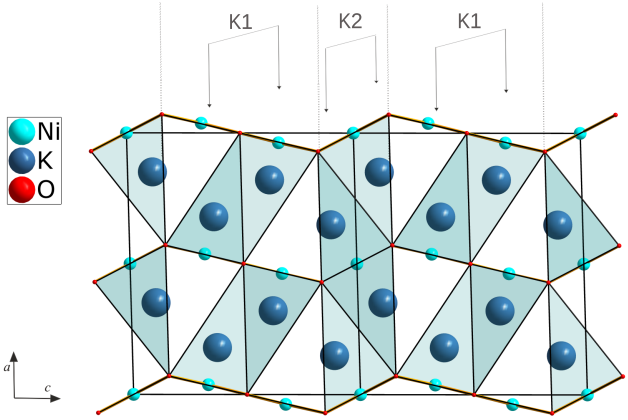

Figure 7.16.: Ordering of $K1O_6$ and $K2O_6$ polyhedra in the $K_4Ni_3O_6$ structure.

strong peak close to $\sim$ 5 K, indicating antiferromagnetic ordering in the structure (Figure 7.17). The inverse magnetic susceptibility was evaluated according to the Curie-Weiss law $\chi = C(T - \theta)^{-1}$ in the temperature range 175 – 400 K, resulting in a magnetic moment μ = 2.09 μ_B, and a Weiss constant θ = – 29.5 K, indicating antiferromagnetic interactions. The calculated magnetic moments are higher than expected for a spin only value (1.73 μ_B), implying some orbital contribution. However, according from the χ^{-1} curve it seems that some intermediate magnetic ordering in the structure takes place close to 160 K. The evaluation of the Curie Weiss law in the 20–160 K temperature range gives a similar value of the magnetic moment. However, the evaluation gives a positive value for the Weiss constant (15.0 K), which suggest the presence of ferromagnetic interactions in the system. Accord-

ing to this, above 160 K the antiferromagnetic interactions are dominating in the system, whereas below 160 K ferromagnetic interactions prevail.

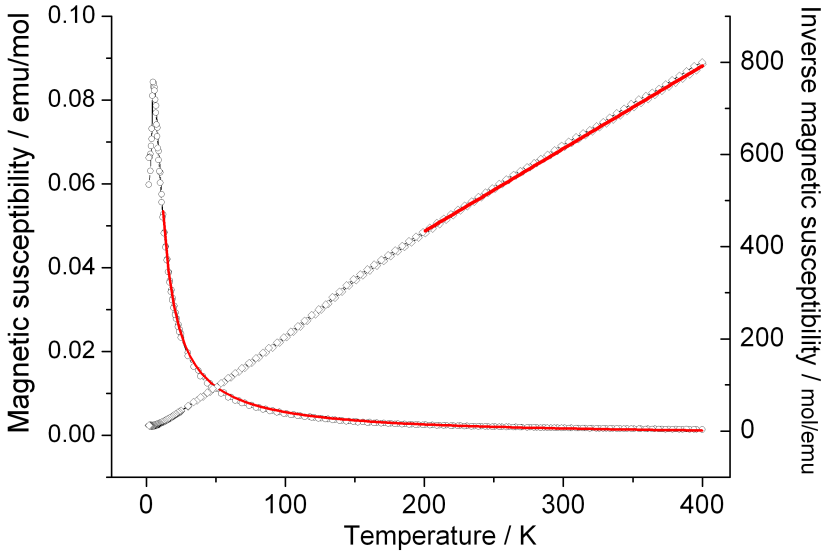

Figure 7.17.: Magnetic susceptibility of $K_4Ni_3O_6$ at 1T.

The magnetic susceptibility in the temperature range 2 – 20 K exhibits field dependency where at higher magnetic field (higher than 1 T) the antiferromagnetic ordering is suppressed (Figure 7.18).

The field dependence of the magnetization was taken at different temperatures, below and above the Néel temperature (2 K, 50K and 292 K Figure 7.19). The measured M-H curves, do not show any obvious hysteresis loops at any temperature, indicating paramagnetic behavior. Below the Néel temperature (at 2 K) the field dependency of the magnetization is larger when compared with the other curves taken at higher temperatures, where above 7 T the magnetization tends to saturate. The magnetic data at 2 K show linear paramagnetic behavior until about $\sim$ 1 T, where probably the re-orientation of the magnetic moments happens. Above 3 T, the magnetization linearly increases and then reaches almost a constant value of 0.8 μ_B. This value is in a good agreement with the saturation moment theoretically expected for the low spin Ni(III) ion.

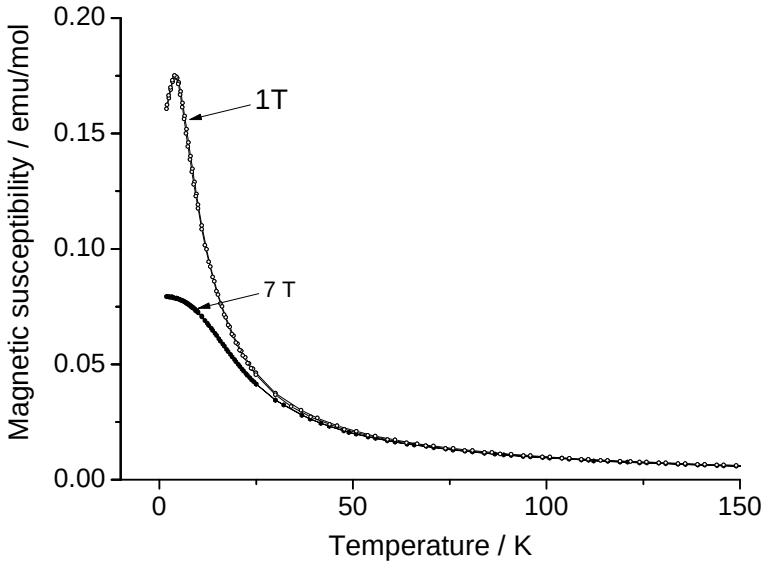

Figure 7.18.: Hysteresis of $K_4Ni_3O_6$.

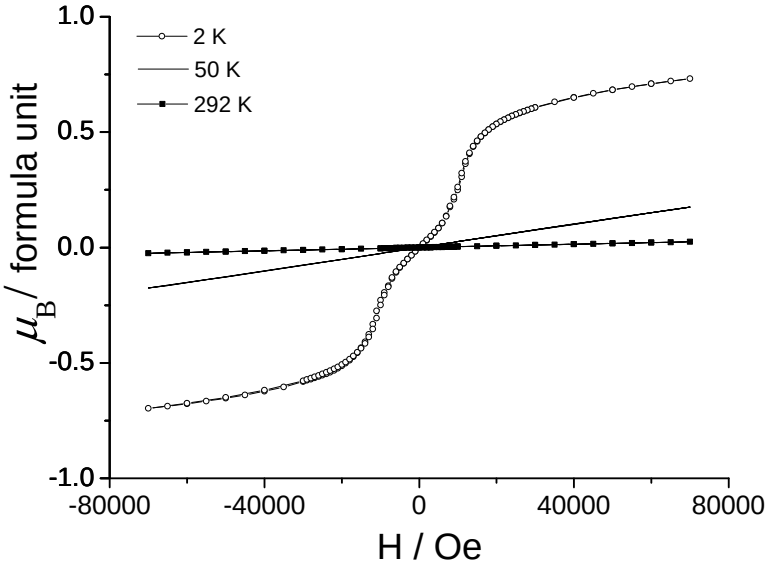

Figure 7.19.: Hysteresis of $K_4Ni_3O_6$.

7.2.4. Specific Heat Measurements

Figure 7.20 shows the temperature dependency of the specific heat for $K_4Ni_3O_6$. The data show the λ-type of anomaly close to $\sim$ 4.92 K, indicating the occurrence of the long range antiferromagnetic ordering of Ni^{3+} ions. The magnetic entropy (S_{mag}) due to the magnetic ordering was calculated by using the following equation:

$$\Delta S = \int_0^T C_{mag}/T \, \mathrm{d}T. \tag{7.12}$$

in which the magnetic specific heat was calculated from the graph Cp/T depending on temperature. The lattice contributions to specific heat were neglected. The entropy change due to the magnetic transition is obtained to be close to 3.82 J/molK, which is in a fair agreement with the theoretical value $R\ln(2S+1)$ = 5.76 J/molK, as expected for the S = 1/2 systems.

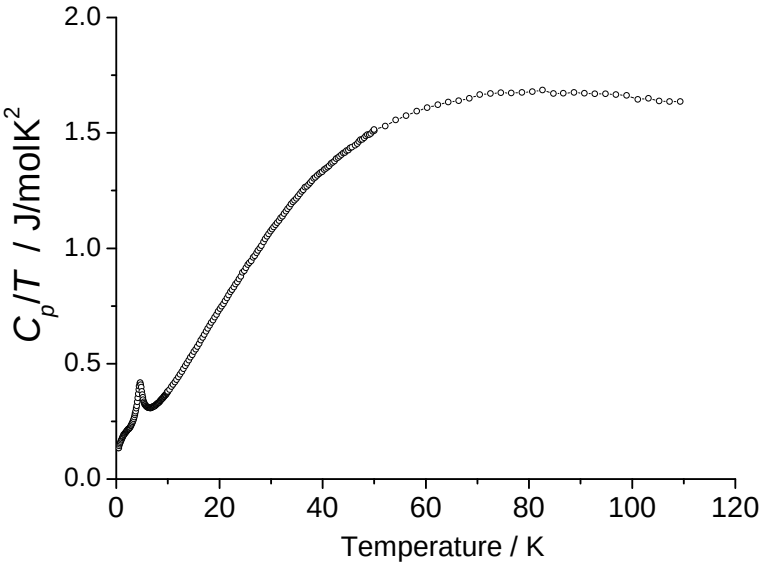

Figure 7.20.: Specific heat measurements of $K_4Ni_3O_6$.

7.3. Synthesis and Physical Properties of New One-Dimensional Oxonickelate $KNa_2Ni_2O_4$

7.3.1. Synthesis, Thermal Analysis and Powder X-ray Diffraction

The starting materials used for the preparation of the $KNa_2Ni_2O_4$ were NaN_3, KN_3, $NaNO_3$, KNO_3 and NiO. The synthesis of NiO and KN_3 has been described in the section 4.3.1 and 4.1, respectively. All starting components were dried at 373 K/12 h under vacuum (10^{-3} mbar) and mixed in an agate mortar in a molar ratio according to equation 7.13.

$$2KN_3 + KNO_3 + 5NaN_3 + NaNO_3 + 6NiO \rightarrow 3KNa_2Ni_2O_4 + 23/2N_2 \qquad (7.13)$$

Single crystals as well as phase pure powders were obtained when the following temperature program was applied 298 → 533 K (100 K/h), 533 → 673 K (5 K/h), 673 → 873 K (600 K/h), and subsequent annealing for 30 h at 873 K (7.13). Due to air and moisture sensitivity, further storage and handling of the samples was done in an inert atmosphere of argon. The thermal analysis showed that the product is approximately stable until 1023 K.

The phase purity of the product was analyzed by means of powder X-ray diffraction with Rietveld refinement (Figure 7.21), with initial atomic coordinates taken from the single crystal solution (section 7.3.2). Results obtained from the Rietveld refinement are listed in the Table 7.11.

7.3.2. Single Crystal Analysis and Crystal Structure Description

The results obtained from the single crystal analysis are presented in the Tables 7.12– 7.14. Interatomic distances (in Å) and coordination numbers (CN), are given in table 7.15.

The single crystal analysis of $KNa_2Ni_2O_4$ revealed that it crystallizes in the monoclinic $P2_1/n$ space group, and its essential structural feature, like in $K_4Ni_3O_6$, are one-dimensional $^1_\infty NiO_2$ chains, formed by NiO_4 square plaquettes. The essential repetition unit in the $^1_\infty NiO_2$ chains is made from four plaquettes (Figure 7.22),

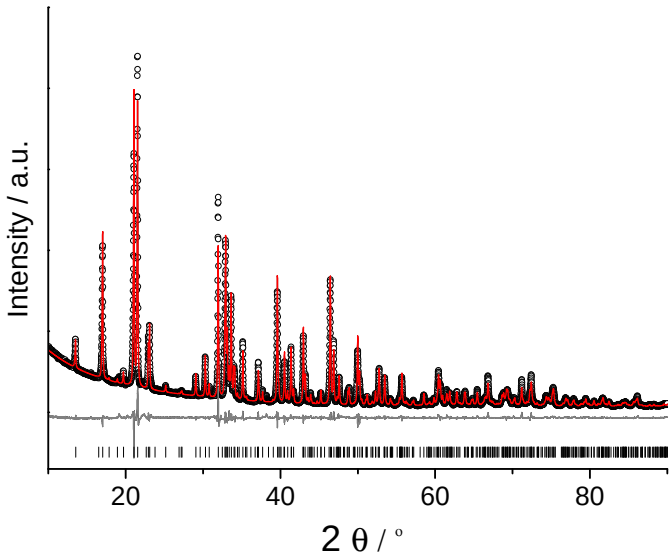

Figure 7.21.: X-ray powder diffraction data of $KNa_2Ni_2O_4$, observed (circles),theoretical pattern (grey solid line) and difference between experimental and calculated patterns (underneath line). Bragg positions used to calculate the theoretical pattern of $KNa_2Ni_2O_4$ are marked by ticks..

Table 7.11.: Crystallographic data for $KNa_2Ni_2O_4$ obtained from Rietveld refinement.

Space Group, Z	$P2_1/n$, 4
Temperature/K	298(5)
Cell parameters/Å	$a = 5.7396(2)$
	$b = 10.7271(1)$
	$c = 8.4541(1)$
	$\beta = 102.92(1)$
Cell Volume/Å^3	507.34(1)
Crystal density/g/cm^3	3.48
Wavelength/Å	Cu$K_{\alpha 1}$, $\lambda = 1.540598$
Range data collection ($2\theta/^o$	10–90
R_{Bragg}/%	1.54
R_p/%	4.37
R_{wp}/%	6.26

where combining of these units leads to undulating chains. The incorporation of sodium as a smaller atom in the structure leads to the formation of less undulating

Table 7.12.: Crystal data and structure refinement data for $KNa_2Ni_2O_4$.

Space Group, Z	$P2_1/n$, 4
Cell parameters/Å and °	$a = 5.7381(11)$
	$b = 10.731(2)$
	$c = 8.4526(17)$
	$\beta = 102.910(3)$
Temperature/K	296(2)
Cell Volume/Å^3	507.32(17)
M_r/g/mol	266.50
Calculated density/g/cm^3	3.489
Crystal form, color	Needle, black
Crystal size/mm	$0.25 \times 0.14 \times 0.11$
Difrfractometer	Bruker AXS, APEX SMART CCD
Monochromator	Graphite
X-ray radiation/$\lambda/\mathring{A}$	Mo-K_α, 0.71073
θ range/^{o}	3.12 to 28.14
Index range	$-7 \leq h \leq 7$
	$0 \leq k \leq 14$
	$0 \leq l \leq 11$
Absorption correction	Multi-scan, TWINABS [109]
Total no. reflections, N_{all}	7124
Independent reflections N	2149
Reflections with $I > 2\sigma(I)$, $\acute{N}$	1980
Absorption coefficient/μ/mm^{-1}	8.320
$F(000)$	516
Refinement method	Full matrix least-squares on F^2
Weighting Scheme	$w = 1/[\sigma^2(Fo^2) + (0.0533P)^2 + 0.8815P]$ where $P = ({F_0}^2 + 2{F_c}^2)/3$
Goodness-on-fit on F^2	1.081
R_1 ($\acute{N}$, N)	0.0378; 0.0411
wR_2 ($\acute{N}$, N)	0.1045; 0.1078

1D-chains as compared with the $K_3Ni_2O_4$ and $K_4Ni_3O_6$. From the analysis of the Ni–O bonds in the $KNa_2Ni_2O_4$, it was not possible to distinguish between 3+ and 2+ oxidation state for the Ni-ions (Table 7.15).

The $^1_\infty NiO_2$ chains are aligned in a honey-comb lattice of the potassium and sodium ions, extending along the b-axis (Figure 7.23). Up to now date there are no other reports concerning mixed valent sodium 1D-oxonickelates(II,III). The two sodium atoms occupy two independent positions where, with coordination number 5, they form square pyramids. The organization and distribution of these pyramids is presented in Figure 7.24. The potassium ion with the coordination number 6

Table 7.13.: Atomic coordinates and isotropic displacement parameters / Å^2 for $KNa_2Ni_2O_4$.

Atom	**Site**	x	y	z	U_{eq}
Ni1	4e	0.2601(1)	0.4174(1)	0.8007(1)	0.0012(1)
Ni2	4e	0.2461(1)	0.6666(1)	0.7398(1)	0.0012(1)
K1	4e	0.2818(1)	0.3896(1)	0.4542(1)	0.0022(1)
Na1	4e	-0.2193(2)	0.4209(1)	0.8947(2)	0.0017(1)
Na2	4e	0.2373(2)	0.2961(1)	0.1226(2)	0.0020(1)
O1	4e	0.0655(4)	0.2844(2)	0.8394(3)	0.0016(1)
O2	4e	0.4574(4)	0.5422(2)	0.7523(3)	0.0019(1)
O3	4e	0.0335(4)	0.7906(2)	0.7295(3)	0.0019(1)
O4	4e	0.0583(4)	0.5510(2)	0.8204(3)	0.0016(1)

Table 7.14.: Anisotropic displacement parameters / Å^2 $\mp$ 10^3 for $KNa_2Ni_2O_4$.

Atom	U_{11}	U_{22}	U_{33}	U_{23}	U_{13}	U_{12}
Ni1	13(1)	5(1)	20(1)	0(1)	6(1)	0(1)
Ni2	12(1)	5(1)	20(1)	1(1)	6(1)	1(1)
K1	23(1)	20(1)	22(1)	-1(1)	6(1)	-1(1)
Na1	16(1)	11(1)	25(1)	0(1)	5(1)	0(1)
Na2	20(1)	16(1)	24(1)	0(1)	6(1)	-2(1)
O1	16(1)	9(1)	25(1)	-1(1)	8(1)	1(1)
O2	18(1)	9(1)	32(1)	3(1)	10(1)	3(1)
O3	16(1)	10(1)	31(1)	3(1)	8(1)	0(1)
O4	16(1)	9(1)	26(1)	2(1)	8(1)	2(1)

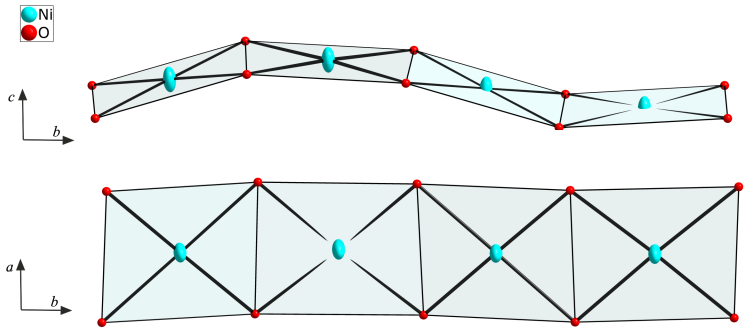

Figure 7.22.: Projections of a $^1_\infty NiO_2$ chain in $KNa_2Ni_2O_4$.

forms distorted trigonal prisms, which are connected through the corners and the

Table 7.15.: Interatomic distances (in pm) and coordination numbers (CN) for $KNa_2Ni_2O_4$.

	O	CN
Ni1–O1	1.885	4
Ni1–O2	1.857	
Ni1–O3	1.859	
Ni1–O4	1.873	
Ni2–O1	1.881	4
Ni2–O2	1.790	
Ni2–O3	1.794	
Ni2–O4	1.868	
K–O1	2.790	6
K–O2	2.644	
K–O2	2.985	
K–O3	2.852	
K–O3	2.858	
K–O4	2.753	
Na1–O1	2.319	5
Na1–O2	2.364	
Na1–O3	2.337	
Na1–O4	2.308	
Na1–O4	2.398	
Na2–O1	2.319	5
Na2–O2	2.364	
Na2–O3	2.337	
Na2–O4	2.308	
Na2–O4	2.398	

edges (Figure 7.25).

7.3.3. Magnetic Measurements

The magnetic data were collected at different strengths of the magnetic field (0.01–7T), where it was found that the susceptibility is independent of the magnetic field in the temperature range 30 – 300 K.

The plot of magnetic susceptibility as well as inverse susceptibility is shown in

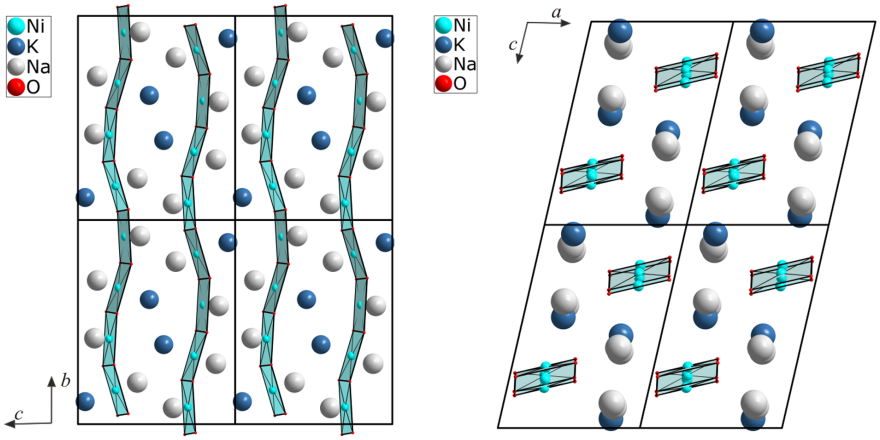

Figure 7.23.: Crystal projection in different orientation for $KNa_2Ni_2O_4$.

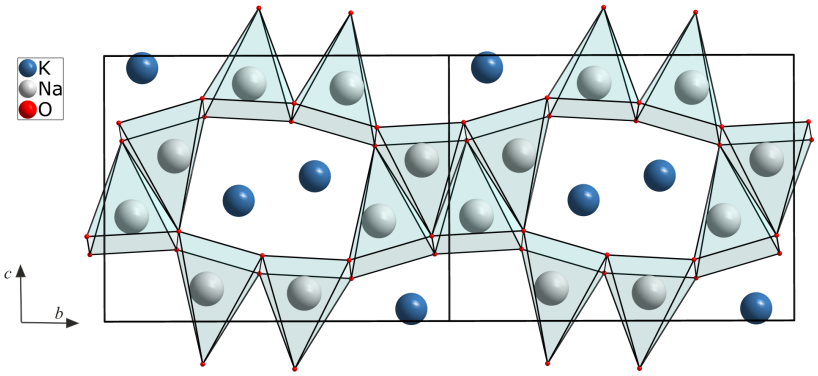

Figure 7.24.: Distribution of NaO_5 square pyramids in the $KNa_2Ni_2O_4$.

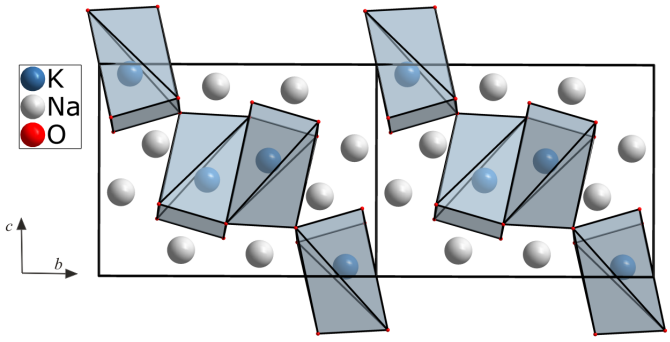

Figure 7.25.: Distriubution of KO_6 prisms in the $KNa_2Ni_2O_4$.

Figure 7.26, where it can be seen that the susceptibility indicates an antiferromagnetic transition close to 5 K. The high-temperature (30–300 K) magnetic behavior

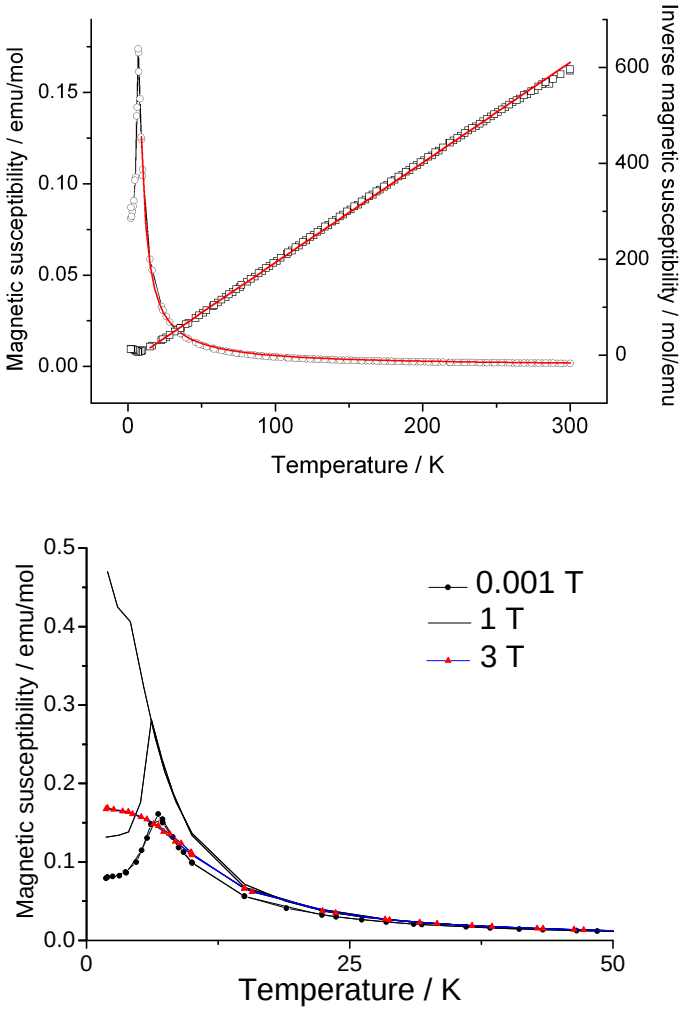

Figure 7.26.: (Upper picture)χ - T and $1/\chi$ - T Magnetic susceptibility behavior for $K_4Ni_3O_6$. The Curie-Weiss fit is given with solid line.(Lower picture) Low temperature magnetic susceptibility at different magnetic field strengths.

can be well evaluated with the Curie Weiss law $\chi = C/(T - \theta)$, resulting in a magnetic moment of $\mu = 1.96\ \mu_B$ and a positive Weiss constant $\theta = 7.65$ K. The magnetic moment is higher than expected for the S = 1/2 spin contribution (1.73 μ_B), due to orbital contributions. The positive Weiss constant implies the presence of ferromagnetic Ni–Ni interactions in the system, while the overall coupling is antiferromagnetic.

The field dependency of the susceptibility is observed at lower temperatures (2–30 K). Figure 7.26 presents magnetic susceptibilities at different magnetic fields (0.01

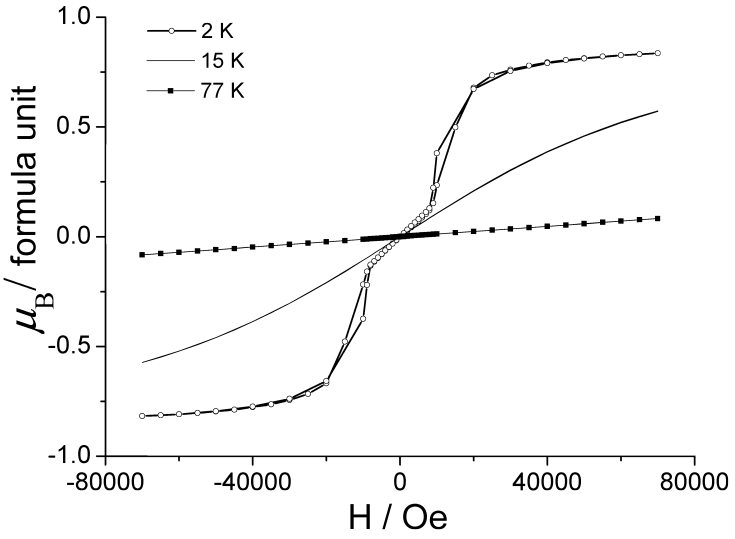

Figure 7.27.: Magnetization as function of magnetic field for $KNa_2NI_2O_4$.

T, 1 T, 3 T).

The long-range magnetic ordering with applied magnetic field can result in a spin re-orientation which is characteristic for both metamagnetism and spin-flop transitions. In order to observe how the magnetization is influenced by the magnetic field, hysteresis curve were measured at temperatures below and above the transition temperature (Figure 7.27). The low-temperature (2 K) data show linear antiferromagnetic behavior until the field reaches the value of $\sim$ 1 T, where the reorientation of magnetic moments occurs. The obtained hysteresis loop is in good agreement with the antiferromagnetic to ferromagnetic ordering at 1 T at 2 K. The spin reorientation appears in the magnetic hysteresis measurements at temperatures below the Néel magnetic transition, while it vanishes above the magnetic transition point. The hysteresis loop exhibits a zero coercive field, which is consistent with the observation that $KNa_2Ni_2O_4$ orders antiferromagnetically. Above 3 T, the magnetization linearly increases and reaches almost a constant value of 0.8 μ_B. This value is in good agreement with the saturation moment theoretically expected for the low spin Ni(III) ion.

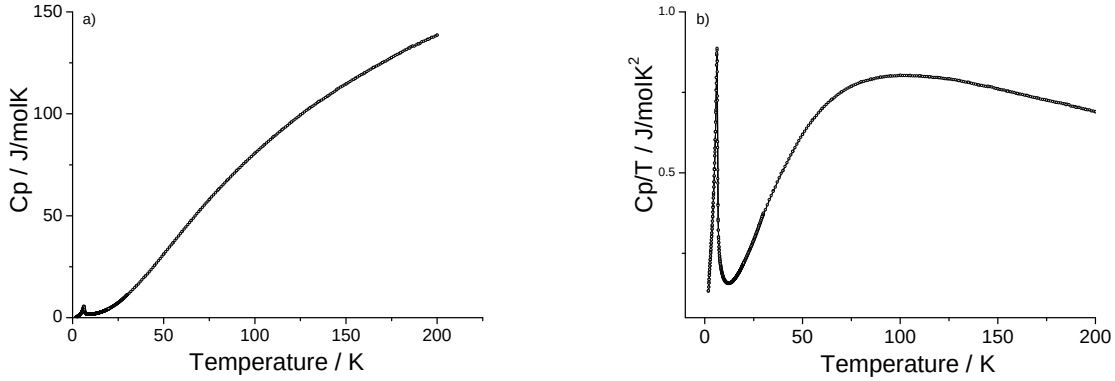

Figure 7.28.: Specific heat measurement for $KNa_2Ni_2O_4$.

7.3.4. Specific Heat Measurements

In order to see whether a $3d$ long magnetic ordering take place, low-temperature specific heat measurements were performed. Figure 7.28 presents the specific heat of $KNa_2Ni_2O_4$, where it can be seen that the magnetic phase transition close ~ 5 K is characterized by a λ-type anomaly. It can be assumed that the Ni–Ni interaction within the chain are antiferromagnetically coupled, with an additional ferromagnetic interchain interaction.

The phonon contribution is negligible at low temperatures, which allows the magnetic contribution to the specific heat to be determined experimentally (according to equation 7.12). The entropy change due to the magnetic transition is obtained to be close to 4.52 J/molK, which is in fair agreement with the theoretical value $R\ln(2S+1) = 5.76$ J/molK, as expected for the S = 1/2 systems.

8.

Preparation of Solid State Solutions by the Azide/Nitrate Route

8.1. Preparation of a $Li_2Ni_{1-x}Cu_xO_2$ Solid State Solution

Li_2CuO_2 is one of the most frequently studied compounds belonging to the family of edge-shared spin chain cuprates. One of the main reasons for the many studies on this class of materials is that these compounds feature ideally planar CuO_2 chains. Due to this fact they are considered as good models for a quasi-one-dimensional frustrated spin system, thus making them appropriate reference systems for high-T_c superconductors. In almost all quasi-one-dimensional copper chain compounds, the spins which are localized on Cu^{2+} ions are expected to be coupled along the chain via nearest neighbor (J_{nn}) ferromagnetic interactions and next-nearest neighbor (J_{nnn}) antiferromagnetic interactions. It is widely accepted that to study such systems, one-dimensional extendend anisotropic Heisenberg model with ferromagnetic (FM) nearest neighbor interactions and antiferromagnetic (AF) next-nearest neighbor one should be used [110]. The FMNN interactions (J_{nn}) strongly depend on the Cu–O–Cu bond angle. Upon increasing this angle, the AFM superexchange interactions increases, where consequently J_{nn} changes from FM to AFM interactions. Due to the induced frustration, FM and spiral in-chain correlations are competing. Since in the one-dimensional model the ground state is governed by the ratio $\alpha = -J_{nn}/J_{nnn}$, the actual three-dimensional model depends on the strengths of the inter-chain coupling and anisotropy. The magnetic structure of Li_2CuO_2 has

already been described by earlier neutron diffraction experiments [111], where it was has been found that the magnetic moments within the CuO_2 planes are ferromagnetically (FM) ordered, whereas neighboring planes are coupled antiferromagnetically (AFM) along the c-axis. Ortega et al. [112] observed at temperatures below 2.8 K the appearance of a ferromagnetic component along the direction of the applied magnetic field.

In order to gain a proper understanding of the quasi-one-dimensional cuprates, several other system has been extensively studied such as $LiCu_2O_2$, $NaCu_2O_2$, $LiCuVO_4$. In this chapter we report how efficient the azide/nitrate route can be in the preparation of the $Li_2Ni_{1-x}Cu_xO_2$ solid state solution. Furthermore, we show the influence on magnetic properties by introducing the Ni^{2+} oxidation state in the Li_2CuO_2 crystal lattice.

8.1.1. Experimental Part

The starting components in the preparation of the $Li_2Ni_{1-x}Cu_xO_2$ solid solution were LiN_3 (Sigma Aldrich, 20 % water solution), $LiNO_3$ (Alfa Aesar, 99.98 %) NiO and CuO. The synthesis of NiO and CuO has been described in the section 4.3.1 and 4.3.2, respectively. LiN_3 water solution was left to dry on a sand bath on 338 K and treated further under the vacuum at 10^{-3} (overnight) in the schlenk tube. The starting mixtures were grounded in agate mortar, in a molar ratio as in the following reactions:

$$5LiN_3 + LiNO_3 + 3CuO \rightarrow 3Li_2CuO_2 \tag{8.1}$$

$$5LiN_3 + LiNO_3 + 2.1CuO + 0.9NiO \rightarrow 3Li_2Cu_{0.7}Ni_{0.3}O_2 \tag{8.2}$$

$$5LiN_3 + LiNO_3 + 1.5CuO + 1.5NiO \rightarrow 3Li_2Cu_{0.5}Ni_{0.5}O_2 \tag{8.3}$$

$$5LiN_3 + LiNO_3 + 0.9CuO + 2.1NiO \rightarrow 3Li_2Cu_{0.3}Ni_{0.7}O_2 \tag{8.4}$$

$$5LiN_3 + LiNO_3 + 3NiO \rightarrow 3Li_2NiO_2 \tag{8.5}$$

In each reaction a 5 % molar excess of LiN_3 and $LiNO_3$ was used. The mixtures were transferred in specially designed containers with silver inlays, and the following temperature treatment was applied: 298 → 353 K (100 K/h), 353 → 673 K (5 K/h), 673 → 873 K (20 K/h), and subsequent annealing for 50 h at 873 K.

Additionally, an alternative approach was pursued in the preparation of the $Li_2Ni_{1-x}Cu_xO_2$ solid state solution. CuO-NiO precursor mixtures were prepared by the solution methods in order to secure better mixing of the Ni and Cu content. Equivalent amounts of $Ni(NO_3)_2 \cdot 6H_2O$ (Alfa Aesar, 99.985 %) and $Cu(NO_3)_2 \cdot xH_2O$ (Alfa Aesar, 99.99 %) were weighted out (n(Ni)/N(Cu) = 1) and dissolved in H_2O. Afterwards, an equivalent amount of $H_2C_2O_4 \cdot 2\,H_2O$ (Chemika, Fluka 99.5 %) was added to the solution under stirring, and the solution was left to precipitate. The precipitate was filtered on the Büchner funnel, left to dry and later was treated in the oxygen stream at 623 K for 20 h. The NiO/CuO precursor obtained was mixed with LiN_3 and $LiNO_3$ according to equation 8.3 and treated using the temperature program mentioned above. The ICP analysis of obtained product revealed that the molar ratio Cu to Ni in $Li_2Ni_{1-x}Cu_xO_2$ Ni : Cu = 0.56 : 0.46 ($x = 0.46$).

Although the lithium oxonickelates and cuprates are relatively stable in air, at least for relatively short times, due to safety reasons they were stored under the argon in glass ampoules. The color of the samples varied from green (Li_2NiO_2) to ocher color (Li_2CuO_2). The azide-nitrate route was proved as a good method in the synthesis of $Li_2Ni_{1-x}Cu_xO_2$ (x = 0, 0.3, 0.5, 0.53, 0.7, 1) solid solution.

8.1.2. X-ray Powder Analysis

The phase purity of the powders was examined by the means of powder X-ray diffraction. A Rietveld plot of the synthesized $Li_2Ni_{1-x}Cu_xO_2$ (x = 0.46) is presented in Figure 8.2, where only a small amount of the $LiNiO_2$ was present (less than 4 %). The Li_2NiO_2 and Li_2CuO_2 crystallize isostructurally in the orthorhombic space group *Immm* (Figure 8.2), and due to the similar ionic radii of Cu^{2+} and Ni^{2+} ions they easily tend to form solid solutions. The calculated lattice parameters obtained from the Rietveld refinement for all the compositions $Li_2Ni_{1-x}Cu_xO_2$ (x = 0, 0.3, 0.5, 0.7, 1), are plotted as function of the Ni/Cu ratio in Figure 8.3. It can be seen that increasing of the Cu content in the system leads to an increase of the lattice parameters b and c, while the a parameter decreases. These data are in good

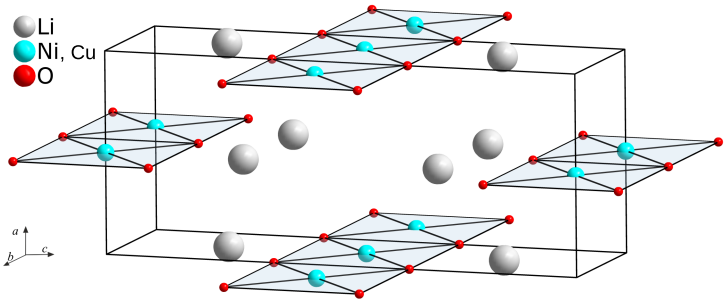

Figure 8.1.: Crystal projection for $Li_2Ni_{x-1}Cu_xO_2$.

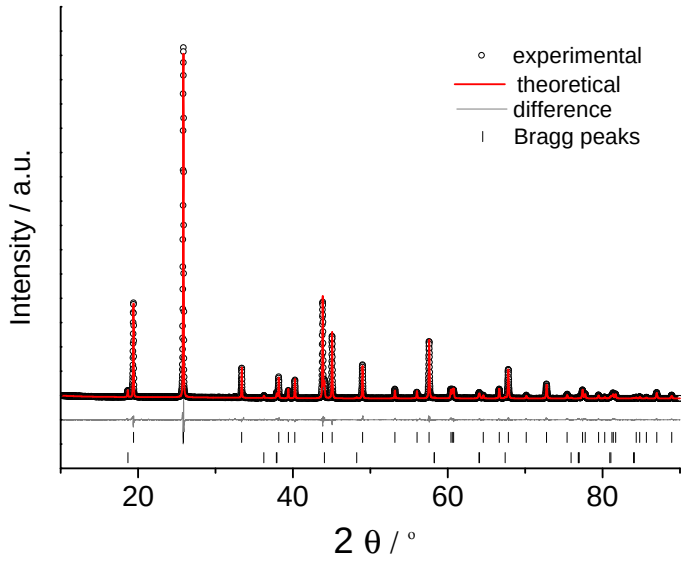

Figure 8.2.: X-ray powder diffraction data of $Li_2Ni_{0.54}Cu_{0.46}O_2$, observed (triangles),theoretical pattern (grey solid line) and difference between experimental and calculated patterns (underneath line). Bragg positions used to calculate the theoretical pattern marked by ticks..

agreement with previously published results by Imanishi *et.al.* [113]. The decrease of the lattice parameters in the b and c direction is possibly due the lower ion radius of the Ni^{2+} ion (0.69 Å), compared with the Cu^{2+} ion (0.79 Å). The Ni^{2+} ion having

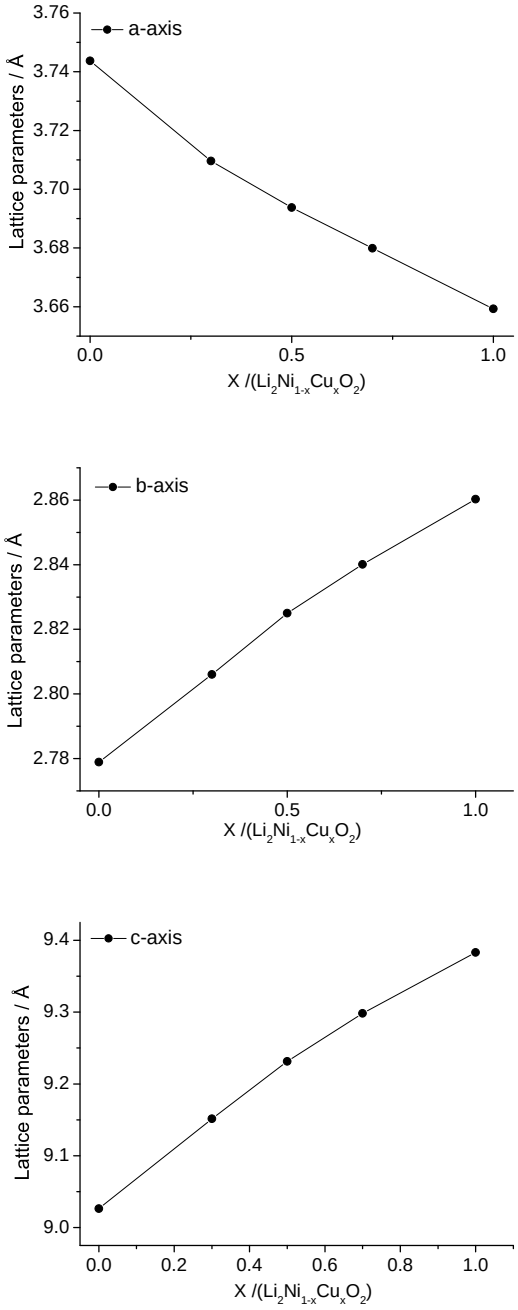

Figure 8.3.: Lattice parameters a, b and c, calculated from the Rietveld refinements of X-ray diffraction powder patterns as a function of the Ni/Cu ratio in $Li_2Ni_{1-x}Cu_xO_2$.

an electronic configuration $d^2_{z^2}$–$d^0_{x^2-y^2}$ shows a greater tendency to take the square planar coordination than Cu^{2+} ion ($d^2_{z^2}$–$d^1_{x^2-y^2}$). The distance along the a-axis

between the chains increases under the stronger effect, and thus Ni^{2+} enrichment leads to an increase in the *a*-axis length [113].

8.1.3. Magnetic Measurements

Magnetic susceptibility measurements were performed for all powder samples at different strengths of the magnetic field (0.1 – 7 T). The magnetic susceptibility of Li_2CuO_2 suggests antiferromagnetic ordering close to 9.8 K (Figure 8.4), and the evaluation of the Curie-Weiss law resulted in the magnetic moment $\mu = 2.11\ \mu_B$ and a Weiss constant close to –47.5 K. These results are in good agreement with the data reported in the literature [110]. In contrast, all the samples of the following compositions $Li_2Ni_{1-x}Cu_xO_2$ (x = 0.3, 0.5, 0.7) exhibit paramagnetic behavior in the whole temperature range and the hysteresis loop shows linear behavior for all magnetic field strengths.

The only exception noticed was for $Li_2Ni_{1-x}Cu_xO_2$ (with x = 0.46). As can be seen from Figure 8.4, the magnetic susceptibility is independent of the magnetic field strength above $\sim$ 250 K. Below 250 K, the sample exhibits irreversibility between the FC (field cooled) and ZFC (zero field cooled) magnetic susceptibilities indicating ferromagnetic behavior. The Curie temperature obtained is close to 210 K, which correponds to the temperature at which dM/dT is maximum. From the ZFC measurements of the susceptibility at 0.1 T it can be noticed, that small peak near 200 K is present, while at higher magnetic fields no difference between the ZFC and FC magnetic susceptibilities is observed.

In addition, hysteresis curves were taken at temperatures below and above the Curie temperature. At temperatures 5 and 77 K it can be seen that $Li_2Ni_{1-x}Cu_xO_2$ (x = 0.53) exhibits similar values for the coercive field (H_c = 1300 Oe), while the remanent magnetization have different values (0.021 emu/mol, 0.032 emu/mol, respectively, Figure 8.6).

8.1.4. Conclusions

The azide nitrate route has proven to be a good tool in the synthesis of $Li_2Ni_{1-x}Cu_xO_2$ (x= 0.3, 0.5, 0.53, 0.7, 1) solid solutions. The introduction of the Ni^{2+} ion into the Li_2CuO_2 crystal lattice results in an increase of the *a* lattice parameter, and a de-

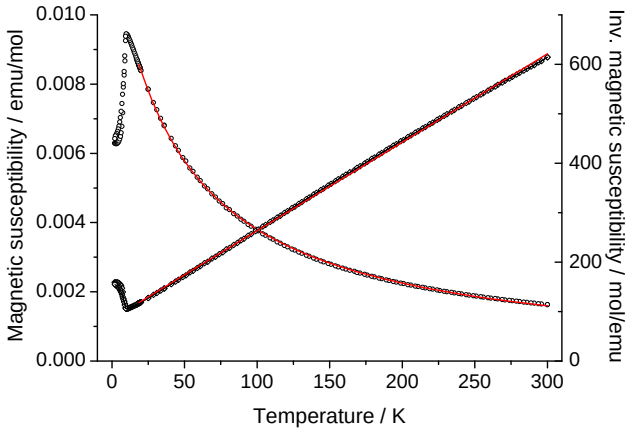

Figure 8.4.: χ - T and $1/\chi$ - T Magnetic susceptibility behavior for Li_2CuO_2. The Curie-Weiss fit is given with red line.

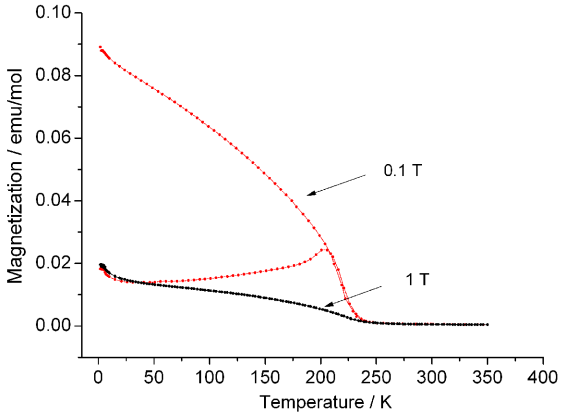

Figure 8.5.: Magnetic susceptibility behavior for $Li_2Ni_{0.54}Cu_{46}O_2$.

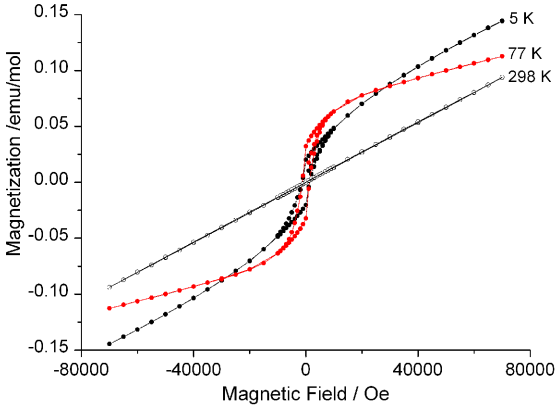

Figure 8.6.: Hysteresis loops taken at different temperatures (5 K, 77 K, 298 K).

crease in the b and c lattice parameters. Susceptibility of the end member of the family (Li_2CuO_2) is characterized with antiferromagnetic ordering close to $\sim$ 10 K. However, the magnetic susceptibilities of the samples of the following composition $Li_2Ni_{1-x}Cu_xO_2$ (x = 0.3, 0.5, 0.7) showed paramagnetic behavior in the whole temperature range (2–298 K). The exception was $Li_2Ni_{1-x}Cu_xO_2$ (x = 0.46), showing ferromagnetic behavior with Curie temperature close to 210 K. A possible explanation on these observations might be different preparation procedure of NiO/CuO precursor powders. It could be noticed that employing the preparation of highly homogenous starting mixtures of CuO and NiO, had impact on the magnetic susceptibility behavior of the final product for following representative ($Li_2Ni_{1-x}Cu_xO_2$ (x = 0.46).

9.

Synthesis of Alkaline-Earth Metal Nickel Oxide

9.1. Synthesis and Thermal Analysis

The starting components in the preparation of barium nickelate were $Ba(N_3)_2$ and NiO. $Ba(N_3)_2$ was obtained from the reaction between the HN_3 and $BaCO_3$. NiO was obtained by the decomposition of $Ni(C_2O_4) \cdot 2H_2O$ at 623 K in the oxygen stream. $Ba(N_3)_2$ and NiO were thoroughly mixed in an agate mortar according to equation 9.1 and afterwards transferred to the specially designed containers 2.2.1:

$$Ba(N_3)_2 + 2NiO \rightarrow "BaNi_2O_2" + 3N_2 \tag{9.1}$$

The following thermal treatment was applied: 298 → 378 K (100 K/h), 378 → 673 K (5 K/h), 673 → 873 K (100 K/h), and subsequent annealing for 50 h at 873 K.

Thermogravimetrical analysis did not reveal any phase transformation until 1273 K.

9.2. X-ray Powder Diffraction

The X-ray powder pattern contained the new compound and three known admixtures: elementary nickel (icsd646087), NiO (icsd76669) and $BaNiO_2$ (icsd30660). The indexing and structure solution were complicated by pseudosymmetry of the new structure. Indexing was performed using the program Topas4.1 [35] and led to

a primitive cubic unit cell. Determination of the real space group was not trivial, since several cubic groups were possible: $Pn\bar{3}m$ and its subgroups $P\bar{4}3m$, $P4_232$, $Pn\bar{3}$, $P23$. All these space groups are non-centrosymmetric, and the lattice transformation matrix between all groups are trivial: unity rotational matrix and zero origin shift. The group-subgroup relation between these five space groups is shown on Figure 9.1.

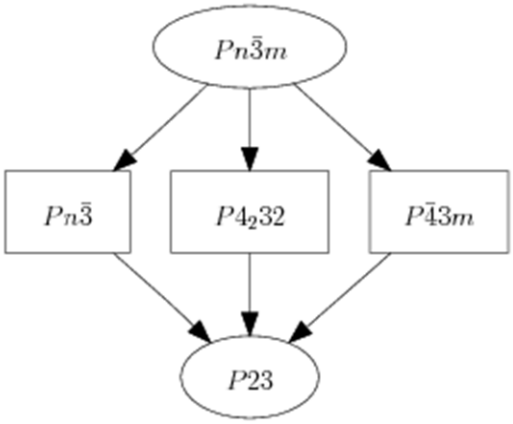

Figure 9.1.: Group-subgroup ralation between space group $Pn\bar{3}m$ and its subgroups $P\bar{4}3m$, $P4_232$, $Pn\bar{3}$, $P23$.

The new structure was solved in four space groups $Pn\bar{3}m$, $P\bar{4}3m$, $P4_232$, and $Pn\bar{3}$ from available powder data and resulted in the chemical formula $Ba_{32}Ni_{24}O_{62}$ (equivalently, $BaNi_{0.75}O_{1.9375}$, or $Ba_{16}Ni_{12}O_{31}$) and was subsequently validated by Rietveld refinement with refined atomic positions. At first, the structure was solved by simulated annealing using the program Topas 4.1 [114,115]. Furthermore, almost all atoms in the structure (except positions of O4 and O5) were found ab-initio by the charge flipping method [116,117] as implemented in Topas [118] and completed by simulated annealing. The presence of two oxygen atoms O4 and O5 with small occupancy of position was confirmed also by calculation of Fourier maps using Topas 4.1: both oxygen atoms O4 and O5 were removed from the structure, the Fourier map, based on the Rietveld refinement without these two atoms, clearly revealed both of them to be present in the structure.

Although the structure is indistinguishable in all space groups $Pn\bar{3}m$, $P\bar{4}3m$, $P4_232$, $Pn\bar{3}$ and $P23$ careful consideration of the chemical and crystallographical aspects of the structure revealed the space group $P4_232$ as the most probable true

space group. This conclusion is based on the chemical and crystallographic analysis of the results of structure solution in all five space groups. Especially based on the analysis of six membered Ni-based rings Ni_6O_{12} (Figure 9.3).

The structure of $Ba_{16}Ni_{12}O_{31}$ in the high-symmetrical space group $Pn\bar{3}m$ should be considered as a pseudosymmetrical structure. In this structure there is only one crystallographically independent position for the Ni atom. The charge balance cannot be fulfilled neither by assuming that the nickel atom has a valence charge 2+, nor by assuming that the nickel atom has a valence charge 3+. The only one possibility to fulfill the charge balance is to suggest the alternation of Ni^{2+} and Ni^{3+} atoms in the 6-membered Ni-rings. In this case the structure in space group $Pn\bar{3}m$ is a pseudosymmetrical structure, where we ignore the difference in the bond lengths between Ni^{2+} – O and Ni^{3+}– O. Such small differences in distances are usually impossible to refine from powder data, and often the pseudosymmetrical space groups are considered as true space groups. In the space groups $P\bar{4}3m$ and $Pn\bar{3}$, the structure has also only one crystallographycally independent position for the Ni atom, and this two space groups also should be rejected. Additionally, all Wyckoff positions of the space group $Pn\bar{3}$, are the special positions in the space group $Pn\bar{3}m$. As a result, all atoms in the structure of $Ba_{16}Ni_{12}O_{31}$ occupy the same position in both space groups $Pn\bar{3}m$ and $Pn\bar{3}$, and the transformation of the structure between these two space groups is trivial.

Two crystallographically independent positions for the Ni atom, allowing the alternation of Ni^{2+} and Ni^{3+} atoms in the 6-membered Ni-rings, were found only in space group $P4_232$ and its subgroup $P23$. The presence of both Ni^{2+} and Ni^{3+} atoms confirmed the right charge balance in the structure of $Ba_{16}Ni_{12}O_{31}$. The unconstrained Rietveld refinement fully validates the structure solution of $Ba_{16}Ni_{12}O_{31}$ in space group $P\bar{4}3m$.

The space group $P23$ is a subgroup of $P4_232$, and the transformation of the structure of $Ba_{16}Ni_{12}O_{31}$ from space group $P4_232$ to space group $P23$ results in the splitting of both Wyckoff positions $24m$ and $8g$ occupied by Ba atoms, two positions of oxygen atoms $24m$ from planar coordination of Ni atoms, and two other oxygen positions with Wyckoff symbols $8g$ and $2a$. The unconstrained Rietveld refinement of this model is not possible due to the big parameter/data ratio. Using the new solved structure in the space group $P4_232$, it was possible to carry out the quantitative phase analysis of the synthesized powder (25 % Ni, 7 % $BaNiO_2$, 5 %

NiO, 63 % new compound). The results obtained from Rietveld refinemet are shown in Tables 9.1- 9.2, and the Rietveld plot is given in Figure 9.2. The calculated distances as well as coordination numbers are given in Table 9.3.

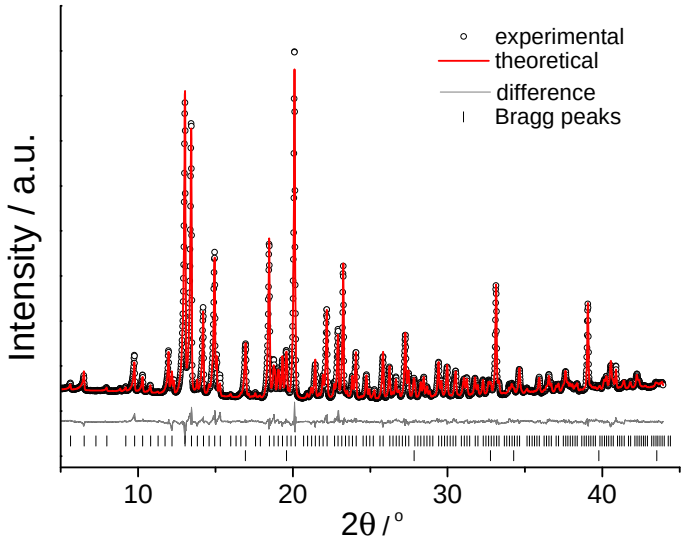

Figure 9.2.: X-ray powder diffraction data of $Ba_{16}Ni_{12}O_{31}$, observed (triangles),theoretical pattern (grey solid line) and difference between experimental and calculated patterns (underneath line). Bragg positions used to calculate the theoretical pattern marked by ticks.

Table 9.1.: Crystallographic data for $Ba_{16}Ni_{12}O_{31}$ obtained from Rietveld refinement.

Space Group, Z	$P4_232$, 2
Temperature/K	120(5)
Cell parameters/Å	a = 12.4899(3)
Cell Volume/Å^3	1948.4(1)
Molar mass/g/mol	6794.95
Absorption coefficient/μ/mm^{-1} Crystal density/g/cm^3	5.7910(3)
Wavelength/Å	Cu$K_{\alpha 1}$, λ = 1.540598
Range data collection ($2\theta/^o$	4–45
R_{Bragg}/%	2.52
R_p/%	3.74
R_{wp}/%	4.99

Table 9.2.: Atomic coordinates and isotropic displacement parameters / Å^2 for $Ba_{16}Ni_{12}O_{31}$.

Atom	Site	x	y	z	U_{eq}
Ba1	$8g$	0.8512(1)	0.1488(1)	0.1488(1)	0.66(5)
Ba2	$24m$	0.3518(1)	0.107(4)	0.107(4)	0.77(4)
Ni1	$12k$	0.607(4)	0.25	0.107(4)	0.47(8)
Ni2	$12l$	0.75	0.394(4)	0.106(4)	0.47(8)
O1	$4b$	1/4	1/4	1/4	2.98(9)
O2	$24m$	0.489(1)	0.78(2)	-0.78(2)	1.7(3)
O3	$24m$	0.097(7)	-0.6199(9)	0.897(7)	1.7(3)
O4	$8g$	0.1244(8)	0.1244(8)	0.1244(8)	3.7(8)
O5	$2a$	0	0	0	4(2)

Table 9.3.: Selected bond lenghts/Å $Ba_{16}Ni_{12}O_{31}$.

Atom	O	CN
Ba1	2.883	10
	3.025	
	3.219	
	3.445	
Ba2	2.562	8
	2.637	
	2.755	
	2.765	
	2.821	
	2.829	
	2.850	
	3.346	
Ni1	1.859	4
	1.899	
Ni2	1.893	4
	1.930	

9.3. Crystal structure description

As discussed in the previous section, the correct solution of the structure of $Ba_{16}Ni_{12}O_{31}$ was validated by Rietveld refinement in the space group $P4_232$. Only this structural model will be discussed further. The projection of the crystal structure of the new $Ba_{16}Ni_{12}O_{31}$ compound is presented in Figure 9.3 where it can be seen that the essential feature of the structure are isolated Ni_6O_{12}–rings composed from the six NiO_4 units. The unit cell contains 4 of these Ni_6O_{12}–rings. Because of the way how these units are connected as well as due to the alternating oxidation state of nickel (+2 and +3), the NiO_4 units are distorted from their usual square plane arrangement. The Ba^{2+} ions exhibit increased values of coordination numbers (CN = 10 and 8) compared to BaO. Similar building units were found in $NaBa_2Ni_3O_6$ [119], where Ni atoms also present in two different oxidation state 2+ and 3+. Analogous Cu_6O_{12}-rings were also found in [119–122] with Cu atoms in two different oxidation states 2+ and 3+. Also Pd_6O_{12}-rings in $CaBa_2Pd_3O_6$ [123] with Pd atoms in two oxidation states 2+ and 3+ are known.

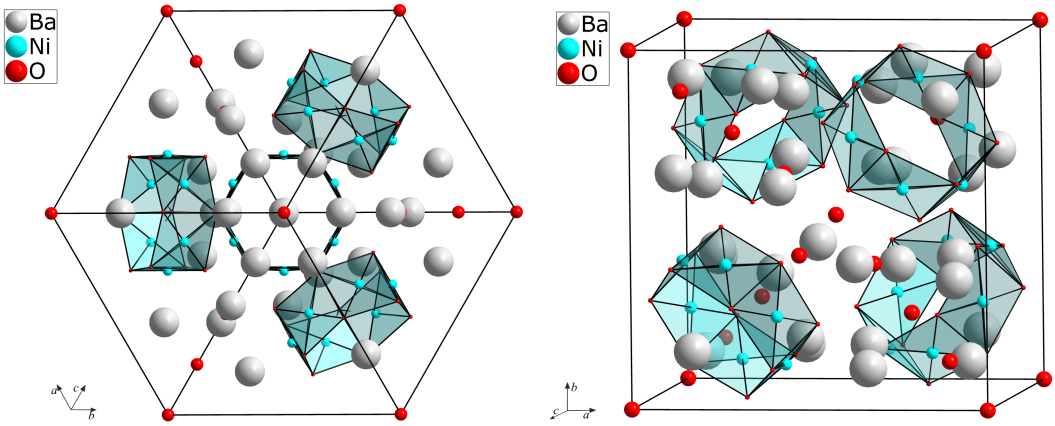

Figure 9.3.: Crystal structure of $Ba_{16}Ni_{12}O_{31}$ presented in different directions.

9.4. Conclusions

Employing the $Ba(N_3)_2$ in the synthesis of ternary metal oxides has proved to be an efficient tool in discovery of new $Ba_{16}Ni_{12}O_{31}$, exhibiting new crystal structure.

Essential structural feature of $Ba_{16}Ni_{12}O_{31}$ are unusual Ni_6O_{12}–rings composed from six NiO_4 units.

10.

Summary

During this PhD thesis, azide/nitrate route has been confirmed to be an efficient tool in the synthesis of alkali-metal oxometalates. As a particularly beneficial feature, azide/nitrate route enables to approach such metastable oxometalates, which are not in reach via classical oxide-acid-base reactions. Especially, with this method it was possible to synthesize new ternary oxides containing low valences and uncommon coordination numbers (CN) of the respective alkali ions (K, Rb, Cs) and transition metal (Ni). Most significantly, this method allows to precisely fix the oxygen content of the target compound, and thus the valence state of transition metal, by the starting azide/nitrate ratio. Along this approach, we have been able to synthesize two families of low dimensional, intrinsically doped oxocuprates(II/III) and oxonickelates(II/III). In addition, the influence of the kind of alkalimetal on the secondary structure as well as physical properties of the one dimensional polyoxometalate anion was examined. Also, introduction of the alkaline earth metal azides in the azide/nitrate route has resulted in a the new phase displaying unusual structural features.

α–K_3NiO_2

In agreement with previously published results, the K_3NiO_2 crystal structure at room temperature has been found to posses the tetragonal unit cell with lattice constants $a = 6.0337(1)$ Å, $c = 14.0623(1)$ Å, and space group $P4_12_12$. Essential feature of the structure are isolated $[NiO_2]^{3-}$ units. The crystal structure is characterized by unusual low coordination numbers, not just of nickel (2) but also for potassium as well (2 and 4). One of potassium ions exhibit increased values of

ADP (U_{33} and U_{12}). Temperature dependent single crystal analysis revealed that the observed anisotropic displacement parameters are strongly temperature dependent. The plot of principal mean square atomic displacement parameters shows that the U_{min}, U_{med}, U_{max} values are considerably reduced and quite uniform at 50 K, which implies that it comes to a dynamic type of disorder in the structure. Initial refinement in the space group $P4_12_12$ resulted in a Flack parameter of 0.53(5), implying the presence of a racemic twin ($P4_12_12/P4_32_12$)) with approximately the same portion of both enantiomorphic forms.

β–K_3NiO_2

For K_3NiO_2 a reversible structural phase transition occurs close to 400 K, as confirmed by temperature dependent X-ray powder and single crystal analysis. Single crystal X-ray analysis at 500 K has shown that the high temperature modification crystallizes in the $P4_2/mnm$ space group (Z = 2, a = 6.0436(1) Å, c = 7.1485(2)) Phase transition to β–K_3NiO_2 is not accompanied in big changes in the local structure where the volume discontinuity and coexistence of both phases (hysteresis) point to a first order phase transition. The structural relationship within the A_3NiO_2 family is analyzed and displayed as a Bärnighausen tree. Magnetic susceptibility indicates paramagnetic behavior in the whole temperature range (60–300K) where evaluation of the Curie-Weiss law resulted in a magnetic moment of μ = 2.22 μ_B (θ = –14.4(6) K). Inverse magnetic susceptibility curves of K_3NiO_2 exhibit a slight shift in the 370 und 400 K temperature range, which corresponds to the $\alpha \rightarrow \beta$ phase transition.

α–Rb_3NiO_2

New Rb_3NiO_2 was synthesized from RbN_3, $RbNO_3$ and NiO as precursors. The crystal structure of Rb_3NiO_2 was solved and refined by X-ray powder methods. The room temperature form was found to be isostructural to α–K_3NiO_2 ($P4_12_12$, Z = 4, a = 6.2651(2) Å, b = 14.7438(3) $\AA$; R_{wp}= 6.30%). Crystal structure is composed from almost linear NiO_2 dumbbells $[NiO_2]^{3-}$ units. Rb2 ion is positioned between two $[NiO_2]^{3-}$ units leading to the formation of infinite [–Ni–O–Rb2–O–Ni–] linear chains, where the (O–Rb2–O) angle of 165.1(2)° leaves Rb2 slightly shifted off the

linear chain.

β–Rb_3NiO_2

Temperature-dependent X-ray powder analysis of Rb_3NiO_2 revealed that at $\sim$ 390 K Rb_3NiO_2 exhibits a phase transition from the lower symmetry space group $P4_12_12$ to the higher symmetric space group $P4_2/mnm$ (Z = 2, $a = 6.2750(2)$ $\AA$, $b = 7.5088(3)$ $\AA$; $R_{wp} = 7.85$ %). Phase transformation to the high temperature modification β–Rb_3NiO_2 is generating totally linear [–Ni–O–Rb2–O–Ni–] chains ($\angle$ O–Rb2–O = 180 °). The phase transition monitored complies with the expectations according to the groupe-subgroup relations reported for K_3NiO_2. Magnetic susceptibility exhibit paramagnetic behavior in the whole temperature range (60–300K) where evaluation of the Curie-Weis law resulted in a magnetic moment of $\mu = 2.19$ μ_B (θ = –14.0(4) K). Inverse magnetic susceptibility curves of Rb_3NiO_2 exhibit a slight shift in the 370–400 K temperature range, which corresponds to the $\alpha \rightarrow \beta$ phase transition.

Cs_3NiO_2

Cs_3NiO_2 was synthesized for the first time from stoichiometric ratio of starting materials (CsN_3, $CsNO_3$ and NiO) at 723 K for 30 h. Rietveld refinement of Cs_3NiO_2 at room temperature data showed it to be isostructural to β–K_3NiO_2 ($P4_2/mnm$, Z = 2, $a = 6.4336(3)\AA$ $c = 8.0844(4)$ Å, $R_{wp} = 5.21$ %)) Temperature dependent X-ray powder measurements of Cs_3NiO_2 were performed up to 433 K. However, not any hint for change in the phase composition was obtained. Magnetic susceptibility indicates paramagnetic behavior in the whole temperature range, where its evaluation according to Curie-Weiss law lead to calculated magnetic moments of $\mu = 2.15$ μ_B (θ = –30.5(1.5) K)

Cs_2NiO_2

Single crystals as well as microcrystalline powders of Cs_2NiO_2 were obtained *via* the azide/nitrate route from appropriate mixtures of CsN_3, $CsNO_3$ and NiO. The single-crystal structural analysis confirmed that Cs_2NiO_2 crystallizes in the tetragonal space group $I4/mmm$ (Z = 2, a = 4.4090(3), c = 13.576(3) $\AA$, $R_1 = 0.036$, $wR_2 = 0.093$). Above 45 K, Cs_2NiO_2 is paramagnetic and an analysis based on the

Curie-Weiss law has resulted in $\mu = 2.89\ \mu_B$ paramagnetic unit, $\theta = -30.8$ K where Cs_2NiO_2 orders antiferromagnetically at $T_N = 20$ K.

$K_3Cu_2O_4$

Single crystals of new $K_3Cu_2O_4$ were prepared by the azide/nitrate route from respective stoichiometric mixtures of KN_3, KNO_3 and CuO, at 923 K, whereas powder samples were synthesised by solid state reaction of K_2O, $KCuO_2$ and CuO, sealed in gold ampoules and treated at 723 K. According to the single crystal structure analysis (*Cmcm*, $Z = 4$, a = 6.1234(1), b = 8.9826(2), c = 10.8620(2) $\AA$, $R_1 = 0.044$, $R_2 = 0.107$), the main structural feature are undulating $^1_\infty CuO_2$ chains built up from planar, edge sharing CuO_4 square units. From an analysis of the CuO bond lengths, the valence state of either +2 or +3 can be unambiguously assigned to each copper atom. The magnetic susceptibilities show the dominance of antiferromagnetic (AFM) interactions. At high temperatures, the magnetic behaviour can be fitted with the CurieWeiss law ($\mu = 1.84\ \mu_B$, $\theta = -105$ K). The experimental data can be very well described by a uniform Heisenberg chain with a nearest-neighbour spin intrachain interaction (J_{nn}) of $\sim$ 101 K. Specific heat measurement did not revealed any long range $3d$-magnetic ordering.

$K_4Ni_3O_6$

Single crystals as well as phase pure powders of the new $K_4Ni_3O_6$ were obtained in a two step synthesis. First part includes preparation of $K_3Ni_2O_4$ from stoichiometric mixture of KN_3, KNO_3 and CuO, which were treated at 873 K in an argon stream. Second part includes the treatment of the obtained $K_3Ni_2O_4$ in oxygen stream at 873 K. Single crystal analysis revealed that $K_4Ni_3O_4$ crystallizes monoclinic in the space group $C2/m$ (Z = 2; $a = 8.9933(14)\AA$, $b = 6.1010(10)$ $\AA$, $c = 7.7910(13)$ $\AA$, $\beta = 91.660(2)$ ° $R_1 = 0.0304$, $R_2 = 0.0877$). The essential feature of the structure are undulating $^1_\infty NiO_2$ chains, aligned in a honey-comb lattice of potassium ions. Magnetic susceptibility indicates paramagnetic behavior with an antiferromagnetic ordering close to 5 K. Evaluation using the Curie-Weiss law resulted in $\mu = 2.09$ μ_B, and a Weiss constant $\theta = -29.5$ K, indicating antiferromagnetic interactions. Specific heat measurements revealed that $3d$ long range magnetic ordering takes

place close to $\sim$ 5 K, as characterized by a λ-type anomaly.

$KNa_2Ni_2O_4$

The starting materials used for the preparation of the new $KNa_2Ni_2O_4$ were NaN_3, KN_3, $NaNO_3$, KNO_3 and NiO. The single crystal analysis of $KNa_2Ni_2O_4$ revealed that it crystallizes in a monoclinic $P2n$ space group (Z = 4, a = 5.7381(11) b = 10.731(2) $\mathring{A}$, c = 8.4526(17) $\mathring{A}$, β = 102.910(3)°, R_1 = 0.0411, R_2 = 0.1078), and its essential structural feature are, like in $K_4Ni_3O_6$, one-dimensional $^1_\infty NiO_2$ chains, formed by NiO_4 square plaquettes. Antiferomagnetic ordering was monitored to order close to 5 K. The high-temperature (30–300 K) magnetic behavior can be well evaluated using the Curie-Weiss law $\chi = C/(T - \theta)$, resulting in a magnetic moment of μ = 1.96 μ_B and a positive Weiss constant θ = 7.65 K. The magnetic moment is higher than expected for a S = 1/2 spin contribution (1.73 μ_B), due to orbital contributions. The positive Weiss constant implies the presence of ferromagnetic Ni–Ni interactions in the system, while the overall coupling is antiferromagnetic. Specific heat measurement revealed that the magnetic phase transition close to $\sim$ 5 K is characterized by a λ-type anomaly.

$Li_2Ni_{1-x}Cu_xO_2$

The azide/nitrate route has proven to be an efficient tool in the synthesis of $Li_2Ni_{1-x}Cu_xO_2$ (x = 0, 0.3, 0.5, 0.7, 1) solid state solution. Magnetic susceptibility of the end member of the family (Li_2CuO_2) is characterized by antiferromagnetic behavior. Evaluation of the Curie-Weiss law resulted in the magnetic moment μ = 2.11 μ_B and a Weiss constant close to –47.5 K. These results are in good agreement with the data reported in the literature. In contrast, all the samples of the following compositions $Li_2Ni_{1-x}Cu_xO_2$ (x = 0.3, 0.5, 0.7) exhibit paramagnetic behavior in the whole temperature range and the hysteresis loop shows linear behavior for all magnetic field strengths. The only exception noticed was for $Li_2Ni_{1-x}Cu_xO_2$ (with x = 0.46). The magnetic susceptibility is independent of the magnetic field strength above $\sim$ 250 K. Below 250 K, the sample exhibits FC and ZFC splitting of the magnetic susceptibilities indicating ferromagnetic behavior. Hysteresis curves were taken at temperatures below and above the Curie temperature. At temperatures

5 and 77 K it can be seen that $Li_2Ni_{1-x}Cu_xO_2$ (x = 0.53) shows similar values for the coercive field (H_c = 1300 Oe), while the remanent magnetization have different values (0.021 emu/mol, 0.032 emu/mol, respectively).

$Ba_{16}Ni_{12}O_{31}$

The starting components in the preparation of barium nickelate $Ba_{16}Ni_{12}O_{31}$ were $Ba(N_3)_2$ and NiO. The product nickelate where the respective nickelate was obtained after thermal treatment at 873 K. Thermogravimetrical analysis of the as obtained product did not reveal any phase transformation until 1273 K. The structure was solved from X-ray powder data by simulated annealing using the program Topas 4.1., and refined by the Rietveld procedure in space group $P4_232$ (Z = 2, a = 12.4899(3), R_{wp} = 4.99 %). Essential feature of the structure are isolated six member Ni_6O_{12} rings composed from NiO_4 plaquettes, where the Ba ion also build unusual polyhedra in the structure (CN = 8 and 10).

11.

Zusammenfassung

Im Rahmen der vorliegenden Dissertation wurde gezeigt, dass die Azid-Nitrat-Route ein effizientes Werkzeug zur Synthese von Alkalimetal-oxometallaten darstellt. Ein besonders herauszustellender Vorteil dieser Methode ist die möglich gewordene Synthese metastabiler Oxometallate welche nicht durch die klassische Oxid-Säure-Base-Reaktion hergestellt werden können. So war es möglich neue ternäre Oxide, mit ungewöhnlicher Koordinationszahl (CN) der Alkali- (K, Rb, Cs) sowie der Übergangs-metalle (Ni und Cu) und ungewöhnlich niedriger Oxidationszahl des Nickels, darzuste-llen. Das Bedeutsame dieser Methode stellt vor allem die genaue Einstellung des Sauerstoffgehalts und somit der Oxidationszahl des Übergangsmetalls, über das Verhältnis von Azid zu Nitrat, in der Zielverbindung dar. Anhand dieses Vorgehens war es uns möglich zwei Klassen niederdimensonaler, *intrinsisch* dotierter Oxocuprate (II/III) und -nickelate (II/III) darzustellen. Zusätzlich wurde der Einfluss des jeweiligen Alkalimetalls auf die Sekundärstruktur wie auch die physikalischen Eigenschaften des eindimensionalen Polyoxometallatanions untersucht. Ebenso führte die Verwendung von Erdalkalimetallaziden in der Azid-Nitrat-Route zu einer neuen Phase mit ungewöhnlichen strukturellen Eigenheiten.

α-K_3NiO_2

In Übereinstimmung mit den zuvor publizierten Ergebnissen kristallisiert K_3NiO_2 in der tetragonalen Raumgruppe $P4_12_12$, mit den Gitterkonstanten $a = 6.0337(1)$ Å, $c = 14.0623(1)$ Å. Im Wesentlichen besteht die Struktur aus isolierten $[NiO_2]^{3-}$

Einheiten. Charakteristisch für die Kristallstruktur sind ungewöhnlich niedrige Koordinationszahlen, nicht nur von Nickel (CN = 2), sondern auch von Kaliums (CN = 2 und 4). Ein Kaliumkation zeigt erhöhte anisotrope Auslenkungsparameter. Temperaturabhängige Messungen am Einkristall bewiesen, dass die Auslenkung stark temperaturabhängig ist. Die Auftragung des einfachen mittleren quadratischen Fehlers der atomaren Auslenkungspara-meter zeigt bei 50 K einen deutlich reduzierten und gleichmäßigen Wert von U_{min}, U_{med}, U_{max} welcher darauf schließen lässt, dass es zu einer dynamischen Fehlordnung innerhalb der Struktur kommt. Anfängliche Verfeinerung in der Raumgruppe $P4_12_12$ resultierte in einem Flack-Parameter von 0.53(5), welcher die Anwesenheit einer racemischen Verzwillingung ($P4_12_12/P4_32_12$)) mit annähernd gleichen Anteilen beider enantiomorphen Formen impliziert.

β–K_3NiO_2

Für K_3NiO_2 konnte, durch temperaturabhängige Pulver- und Einkristallmessungen belegt, eine reversible Phasenumwandlung bei 400 K beobachtet werden. Messungen an Einkristallen bei 500 K haben gezeigt, dass die Hochtemperaturphase in der Raumgruppe $P4_2/mnm$ kristallisiert (Z = 2, a = 6.0436(1) Å, c = 7.1485(2)) ist. Die Phasenumwandlung zu β–K_3NiO_2 geht nicht mit einer großen Änderungen der lokalen Struktur einher, wobei die Diskontinuität des Volumen und Koexistenz beider Phasen (Hysterese) auf einen Übergang erster Ordnung hindeuten. Die strukturelle Verwandtschaft zur Klasse der A_3NiO_2 wurde analysiert und als Bärninghausendiagramm dargestellt. Messung der magnetischen Suszeptibilitt deutet auf paramagnetisches Verhalten im gesamten Temperaturbereich (60 – 300 K), die Auswertung mit Hilfe des Gesetzes von Curie-Weiss resultiert in einem magnetischen Moment von μ = 2.22 μ_B (θ = –14.4(6) K). Die leichte Verschiebung der inversen magnetischen Suszeptibilität zwischen 370 und 400 K kann der Phasenumwandlung von α-K_3NiO_2 in β-K_3NiO_2 zugeschrieben werden.

α–Rb_3NiO_2

Das neue Rb_3NiO_2 wurde aus den Vorläufern RbN_3, $RbNO_3$ und NiO dargestellt. Die Kristallstruktur des Rb_3NiO_2 wurde durch Pulvermethoden gelöst und verfein-

ert. Die Raumtemperaturform ist isostrukturell zur α-K_3NiO_2 Phase ($P4_12_12$, Z = 4, a = 6.2651(2) Å, b = 14.7438(3) $\mathring{A}$; R_{wp}= 6.30%). Die Struktur ist aus nahezu linearen $[NiO_2]^{3-}$ Hanteln aufgebaut. Ein Rubidiumkation (Rb2) befindet sich zwischen zwei $[NiO_2]^{3-}$ Einheiten. Dies führt zu einer unendlichen linearen Kette [–Ni–O–Rb2–O–Ni–], wobei der (O–Rb2–O) Winkel 165.1(2)° beträgt, weshalb das Rb2 ein wenig außerhalb der Ebene der linearen Kette liegt.

β–Rb_3NiO_2

Durch temperaturabhängige Pulvermessungen des Rb_3NiO_2 konnte gezeigt werden, dass die Phasenumwandlung bei 390 K von der Raumgruppe $P4_12_12$ mit geringer Symmetrie zur höher symmetrischen Raumgruppe $P4_2/mnm$ (Z = 2, a = 6.2750(2) $\mathring{A}$, b = 7.5088(3) $\mathring{A}$; R_{wp} = 7.85 %) führt. Die Umwandlung zur β–Rb_3NiO_2 Hochtemperaturphase erzeugt vollständig lineare [–Ni–O–Rb2–O–Ni–] Ketten. Die Phasenumwandlung folgt den Voraussagen die bereits auf Grund der Gruppe-Untergruppe-Beziehung für K_3NiO_2 dargestellt wurde. Die magnetische Suszeptibilität zeigt paramagnetisches Verhalten im gesamtem Temperaturbereich (60 – 300 K), die Auswertung mit Hilfe des Gesetzes von Curie-Weiss resultiert in einem magnetischen Moment von μ = 2.19 μ_B (θ = –14.0(4) K). Die leichte Verschiebung der inversen magnetischen Suszeptibilität zwischen 370 – 400 K kann der Phasenumwandlung von $\alpha \rightarrow \beta$ zugeschrieben werden.

Cs_3NiO_2

Cs_3NiO_2 wurde im Rahmen dieser Dissertation erstmals aus einem stöchiometrischen Gemenge der Edukte CsN_3, $CsNO_3$ and NiO bei 723 K dargestellt. Rietveld Verfeinerung an Raumtemperaturdaten zeigt, dass Cs_3NiO_2 als isostrukturell zu β–K_3NiO_2 ($P4_2/mnm$, Z = 2, a = 6.4336(3)$\mathring{A}$ c = 8.0844(4) Å, R_{wp} = 5.21 %)) ist. Temperaturabhängige Röntgenmessungen am Pulver wurden bis 433 K durchgeführt. Jedoch wurde kein Hinweis für eine Phasenumwandlung gefunden. Die magnetische Suszeptibilität zeigt paramagnetisches Verhalten im gesamtem Temperaturbereich an, die Auswertung mit Hilfe des Gesetzes von Curie-Weiss führt zu einem magnetischen Moment von μ = 2.15 μ_B (θ = –30.5(1.5) K).

Cs_2NiO_2

Messungen von Einkristallen wie auch am mikrokristallinem Pulver konnte von Cs_2NiO_2, das durch adäquate Mischungen von CsN_3, $CsNO_3$ und NiO ber die Azid-Nitrat-Route dargestellt wurde, durchgeführt werden. Die Einkristallstrukturanalyse bestätigt, dass Cs_2NiO_2 in der tetragonalen Raumgruppe $I4/mmm$ (Z = 2, a = 4.4090(3), c = 13.576(3) $\AA$, $R_1 = 0.036$, $wR_2 = 0.093$) kristallisiert. Über 45 K zeigt Cs_2NiO_2 Paramagnetismus und die Analyse basierend auf dem Curie-Weiss Gesetz resultiert in einem magnetischen Moment von $\mu = 2.89\ \mu_B$ und θ = –30.8 K. Bei T_N = 20 K liegt eine antiferromagnetische Ordnung des Cs_2NiO_2 vor.

$K_3Cu_2O_4$

Einkristalle des neuen $K_3Cu_2O_4$ konnten über die Azid-Nitrat-Route aus stöchiometrischen Mischungen von KN_3, KNO_3 und CuO, bei 923 K erhalten werden. Pulverproben wurden durch Festkörperreaktion von K_2O, $KCuO_2$ und CuO, in verschlossenen Goldampullen, bei 723 K dargestellt. Die Einkristallanalyse (*Cmcm*, *Z* = 4, a = 6.1234(1), b = 8.9826(2), c = 10.8620(2) $\AA$, $R_1 = 0.044$, $R_2 = 0.107$) zeigt, dass das Hauptstrukturelement aus gewellten $^1_\infty CuO_2$ Ketten, aufgebaut aus quadratisch-planaren, kantenverknüpften CuO_4 Einheiten, besteht. Durch die Analyse der Cu–O Bindungslänge konnte der Oxidationszustand jedes Kupferatomes (II/III) eindeutig zugeordnet werden. Die magnetischen Messungen zeigen das Vorliegen von antiferromagnetischen Kopplungen. Bei hohen Temperaturen kann das magnetische Verhalten dem Curie-Weiss Gesetz ($\mu = 1.84\mu_B$, θ = –105 K) angepasst werden. Die experimentellen Daten können sehr gut über eine gleichförmige Heisenbergkette, mit nächstliegender Nachbar-Spin-Intraketten Wechselwirkung ($\mu = 1.84\mu_B$ mit Weiss-Konstante θ = –105 K) beschrieben werden. Messungen der spezifischen Wärme offenbarte keine magnetische $3d$ Fernordung.

$K_4Ni_3O_6$

Einkristalle wie auch phasenreines Pulver des neuen $K_4Ni_3O_6$ wurde durch eine zweistufige Synthese erhalten. Zuerst wurde $K_3Ni_2O_4$ aus einer stöchiometrischen Mischung aus KN_3, KNO_3 und CuO bei 873 K im Argonstrom erhalten. Im Anschluss wurden Einkristalle des $K_3Ni_2O_4$ in Sauerstoffstrom bei 873 K behandelt.

Messungen am Einkristall offenbarte, dass $K_4Ni_3O_4$ in der monoklinen Raumgruppe $C2/m$ (Z = 2; a = 8.993(2)$\mathring{A}$, b = 6.101(1) $\mathring{A}$, c = 7.791(1) $\mathring{A}$, β = 91.660(2)° R_1 = 0.0304, R_2 = 0.0877) kristallisiert. Das Hauptstrukturelement besteht aus gewellten $^1_\infty NiO_2$ Ketten die sich in einem honigwabenartigen Gitter, bestehend aus Kaliumkationen, befinden. Messungen der magnetischen Suszeptibilität lassen auf Paramagnetismus schließen mit antiferromagnetischer Ordnung nahe 5 K. Die auswertung mit Hilfe des Curie-Weiss-Gesetzes zeigen ein magnetisches Moment von μ = 2.09 μ_B und einer Weiss-Konstante θ = – 29.5 K, die auf antiferromagnetisches Verhalten schließen lassen. Messungen der Spezifischen Wärme lassen auf eine magnetische Fernordnung bei $\sim$ 5 K schließen, die als λ-artige Anomalie klassifiziert werden konnte.

$KNa_2Ni_2O_4$

Als Ausgangsmaterialien für die Synthese des neuen $KNa_2Ni_2O_4$ wurde NaN_3, KN_3, $NaNO_3$, KNO_3 und NiO verwendet. Einkristallanalyse des $KNa_2Ni_2O_4$ offenbarte, dass die Verbindung in der monoklinen Raumgruppe $P2_1/n$ Z = 4, a = 5.738(1) b = 10.731(2) $\mathring{A}$, c = 8.453(2) $\mathring{A}$, β = 102.910(3)°, R_1 = 0.0411, R_2 = 0.1078) kristallisiert, und das Hauptstrukturmerkmal, wie in $K_4Ni_3O_6$, eindimensionale $^1_\infty NiO_2$ Ketten, die aus quadratisch-planaren NiO_4 Einheiten bestehen, darstellt. Das Verhalten der magnetische Suszeptibilität weist eine antiferromagnetische Ordnung nahe 5 K auf. Das magnetische Verhalten bei höherer Temperatur (30 – 300 K) kann gut mit dem Curie-Weiss-Gesetz $\chi = C/(T - \theta)$ ausgewertet werden, es resultiert ein magnetisches Moment von μ = 1.96 μ_B mit einer positiven Weisskonstante von θ = 7.65 K. Das magnetische Moment ist höher als der erwartete Beitrag eines Systems mit Spin S =1/2 (1.73 μ_B), dies ist auf Bahnmoment zurückzuführen. Die positive Weisskonstante impliziert das Vorhandensein von ferromagnetischer Ni–Ni Wechselwirkung innerhalb des Systems, obwohl die insgesamt resultierende Kopplung antiferromagnetischer Natur ist. Messungen der spezifischen Wärme legen nahe, dass der magnetische Phasenübergang bei ca. $\sim$ 5 K ein Kennzeichen einer λ-artige Anomalie ist.

$Li_2Ni_{1-x}Cu_xO_2$

Die Azid-Nitrat-Route hat sich auch als Methode zur Darstellung von festen Lösungen wie $Li_2Ni_{1-x}Cu_xO_2$ (x = 0, 0.3, 0.5, 0.7, 1) bewährt. Die magnetische Suszeptibilität des Schlussgliedes der Klasse (Li_2CuO_2) ist gekennzeichnet durch antiferromagnetisches Verhalten. Auswertung des Curie-Weiss-Gesetzes endet in einem magnetischen Moment von μ = 2.11 μ_B und eine Weiss-Konstante nahe –47.5 K. Dies ist in guter Übereinstimmung mit den in der Literatur berichteten Werten. Im Gegensatz dazu zeigen alle Verbindungen der folgenden Zusammensetzungen $Li_2Ni_{1-x}Cu_xO_2$ (x = 0.3, 0.5, 0.7) paramagnetisches Verhalten im gesamten Temperaturbereich. Die Hystereseschleife weist lineares Verhalten bei allen magnetischen Feldstärken auf. Die einzige Ausnahme zeigte $Li_2Ni_{1-x}Cu_xO_2$ (with x = 0.46). Über $\sim$ 250 K ist die magnetische Suszeptibiltät unabhängig von der angelegten Feldstärke. Unterhalb 250 K zeigt die Probe Irreversibilität zwischen der magnetischen FC und ZFC Suszeptibilität, dies impliziert ferromagnetisches Verhalten. Bei Temperaturen zwischen 5 und 77 K werden für $Li_2Ni_{1-x}Cu_xO_2$ (x = 0.53) gleiche Werte bei eingeschränktem Feld (H_c = 1300 Oe) beobachtet, da die zurückbleibende Magnetisierung verschiedene Werte annimmt (0.021 emu/mol, 0.032 emu/mol).

$Ba_{16}Ni_{12}O_{31}$

Als Edukte für die Synthese des Bariumnickelates $Ba_{16}Ni_{12}O_{31}$ wurde $Ba(N_3)_2$ und NiO eingesetzt, wobei das Nickelat nach thermischer Behandlung bei 873 K erhalten wurde. Thermogravimetrische Analyse zeigte keine Phasenumwandlung unterhalb 1273 K. Die Struktur wurde mittels Simulation mit dem Programm Topas 4.1 gelöst. Die Strukturlösung des $Ba_{16}Ni_{12}O_{31}$ wurde mittels Rietveldverfeinerung in der Raumgruppe $P4_232$ (Z = 2, a = 12.4899(3), R_{wp} = 4.99 %) bestätigt. Hauptstrukturmerkmal stellen isolierte sechsgliedrige Ni_6O_{12}–Ringe bestehend aus NiO_4 Untereinheiten dar, wobei die Bariumkationen ein ungewöhnliche Polyeder in der Struktur ausbilden (CN = 8 und 10).

Part IV.

Formalia

Declaration

The work described in this thesis was carried out by the author in the Department of Prof. Jansen and in the Max Planck Institute for Solid State Research from September 2008 to December 2012. The contents are the original work of the author except where indicated otherwise and have not been previously submitted for any other degree or qualification at any academic institution.

Stuttgart, November 2012 Katarina Djuris

Erklärung

Die vorliegende Doktorarbeit wurde vom Autor selbst in der Abteilung von Prof. Jansen und am Max-Planck-Institut für Festkörperforschung, im Zeitraum von September 2008 bis Dezember 2012 angefertigt. Der Inhalt ist die eigene Arbeit des Autors, Ausnahmen sind gekennzeichnet, und wurde noch nicht zur Erlangung einer Qualifizierung oder eines Titels an einer akademischen Institution eingereicht.

Stuttgart, November 2012 Katarina Djuris

Curriculum Vitae

Name:	Katarina Djuris
Date of birth:	20. August 1979
Place of birth:	Pancevo, Serbien
E-Mail:	k.djuris@fkf.mpg.de
	katdjuris@gmail.com
Marital status:	Single

Academic Studies

09/2008 - 02/2013 PhD research in the in the department of Prof. Dr. Dr. h. c. Martin Jansen at Max-Planck Institute for Solid State Research, Stuttgart, Germany

Major: **Solid State Chemistry**, Chemistry Department, University in Stuttgart

Dissertation: Synthesis and Characterization of New Alkali-Metal Oxometalates Obtained via the Azide-Nitrate Route

11/2005 - 12/2008 **Magister Studies in Material Science**

Multidisciplinary Studies at the University in Belgrade, Serbia

Magister thesis: Synthesis and Characterization of Undoped and Ca, Sr -doped $LaMnO_3$ by Polymerization From Citrate Precursors

10/1998 - 12/2004 **Studies in Chemistry**

Major: **Applied Chemistry**

Faculty for Chemistry, University in Belgrade, Serbia

Diploma Thesis: Isolation and Characterization of Xanthones From Plant Species *Gentiana Utriculosa*

School Education

09/1994 - 06/1998 Technical Gymnasium "23.Maj", Pancevo, Serbien

09/1986 - 06/1994 Primary School "Marsal Tito", Padina, Serbien

Employment records

since 09/2008 **Research Scientist** (PhD)

Max-Planck Institute for Solid State Research, Stuttgart, Germany

01/2006 - 12/2008 **Research Assistant**

Institute for Multidisciplinary Research, Belgrade, Serbia

List of Publications

1. **K. Đuriš**, O. V. Magdysyuk, M. Jansen, "Synthesis, structure and magnetic properties of new alkalioxnickelates(I) A_3NiO_2 (A = K, Rb, Cs)" *Solid State Sci.* 14 (2012) 1399.

2. **K. Đuriš**, M. Jansen, "Cs_2NiO_2 Revisited. Crystal Structure and Magnetic Properties" *Z. Naturforsch.* 67b (2012) 57.

3. **K. Đuriš**, U. Müller, M. Jansen, "K_3NiO_2 Revisited, Phase Transition and Crystal Structure Refinement" *Z. Anorg. Allg. Chem.* 638 (2012) 737.

4. **K. Đuriš**, R. K. Kremer, M. Jansen, "Synthesis, Crystal Structure, and Physical Properties of the New Chain Alkalioxocuprate $K_3Cu_2O_4$" *Z. Anorg. Allg. Chem.* 637 (2011) 1101.

5. **K. Đuriš**, M. Sofin, J. Nuss, M. Jansen, "Syntheses and crystal structures of new chain alkalioxocuprates $A_{1+x}CuO_2$ (A = K, Na)" *Z. Anorg. Allg. Chem.* 636 (2010) 2059.

6. Z. Brankovic, **K. Đuriš**, A. Radojkovic, S. Bernik, Z. Jaglicic, M. Jagodic, K. Vojisavljevic, G. Brankovic, "Magnetic properties of doped $LaMnO_3$ ceramics obtained by a polymerizable complex method" *J. Sol-Gel Sci. Technol.* 55, 2010, 311.

7. D. Poleti, Lj. Karanovic, T. Dordevic, **K. Đuriš**, "Sodium citrate dihydrate doped with Mn^{3+} ions" *Acta Crystallogr. Sect. C* C65 (2009) m355.

8. G. Brankovic, **K. Đuriš**, Z. Jaglicic, M. Jagodic, and Z. Brankovic, "Magnetic properties of pure and Ca^{2+} and Sr^{2+} doped $LaMnO_3$ prepared by polymerisable complex method" *Adv. Appl. Ceram.* 108 (2009) 267.

9. I. Krkljuš, Z. Brankovic, **K. Đuriš**, S. Bernik, G. Brankovic, "Preparation of $LaMnO_3$ for cathode-supported SOFC by means of electrophoretic deposition", *Int. J. Appl. Ceram. Tec.* 5 (2008) 548.

10. **K. Đuriš**, G. Brankovic, Z. Brankovic, S. Bernik, M. Pocuca, "Synthesis of pure and doped $LaMnO_3$ powders from citrate precursors", *Mater. Sci. Forum*, 555 (2007) 237.

Bibliography

[1] H. Rieck and R. Hoppe. *Z. Anorg. Allg. Chem.*, 400:311–320, 1973.

[2] K. Đuriš, R. K. Kremer, and M. Jansen. *Z. Anorg. Allg. Chem.*, 637(9):1101–1107, 2011.

[3] J. Gopalakrishnan, N. Bhuvanesh, and K. Rangan. Towards rational synthesis of inorganic solids. *Current Opinion in Solid State and Materials Science*, 1(2):285–294, April 1996.

[4] J. C. Schön and M. Jansen. *Angew. Chem.*, 108(12):1358–1377, 1996.

[5] M. Jansen. *Angew. Chem. Int. Ed.*, 41(20):3746–3766, 2002.

[6] F. C. Krebs. *Solar Energy Materials and Solar Cells*, 93(4):394–412, 2009. cited By (since 1996) 591.

[7] Sossina M. Haile. *Acta Materialia*, 51:59816000, 2003.

[8] P. X. Zhang, G. Y. Zhang, C.T. Lin, and H.U. Habermeier. *Egyptian Journal of Solids*, 27:1, 2004.

[9] R. Srinivasa. Spintronics, principles, devices and materials. *Resonance*, pages 53–62, 2005.

[10] S. W. Cheong and M. Mostovoy. *Nature Materials*, 6(1):13–20, January 2007.

[11] H. P. Baldus and M. Jansen. *Angew. Chem. Int. Ed.*, 36(4):328–343, 1997.

[12] M. Jansen and H. P Letschert. *Nature*, 404(6781):980–982, April 2000.

[13] K. Takada, H. Sakurai, E. Takayama-Muromachi, F. Izumi, R. A. Dilanian, and T. Sasaki. *Nature*, 422(6927):53–55, March 2003.

[14] R. Audette, J.Quail, W. Black, and B. Robertson. *J. Solid State Chem.*, 8:43–49, 1973.

[15] F. Bernhardt and R. Hoppe. *Z. Anorg. Allg. Chem.*, 619:969–975, 1993.

[16] M. Jansen. *Z. Anorg. Allg. Chem.*, 638:1910–1921, 2012.

[17] C. N. Rao. *Materials Science and Engineering*, B18:1–21, 1993.

[18] A. Möller. *Z. Anorg. Allg. Chem.*, 631(12):2285–2296, 2005.

[19] D. Trinschek and M. Jansen. *Angew. Chem. Int. Ed.*, 38(1-2):133–135, 1999.

[20] E. Zintl and H. H. v. Baumbach. *Z. Anorg. Allg. Chem.*, 198(1):88–101, 1931.

[21] S. Pfeiffer, J. Nuss, and M. Jansen. *Z. Anorg. Allg. Chem.*, 636:23–29, 2010.

[22] M. Sofin, E. M. Peters, and M. Jansen. *J. Solid State Chem.*, 178(12):3708–3714, 2005.

[23] N. Zafar Ali, Jesko S., J. Nuss, P. Horsch, and M. Jansen. *Physical Review B*, 84(3):035113–, July 2011.

[24] M. Sofin, H. U. Guedel, R. Bircher, E. M. Peters, and M. Jansen. *Angew. Chem. Int. Ed.*, 42:3527–3529, 2003.

[25] W. Schlenk and A. Thal. *Ber. Dtsch. Chem. Ges.*, 46:2840–2854, 1913.

[26] N. Zafar Ali. *New ternary alkalioxometallates of the first-row transition-metal elements through the Azide Nitrate Route*. PhD thesis, Dissertation an der Universitt Stuttgart, 2011.

[27] R. Paneerselvam. *Automated parametric Rietveld refinement and its application to twodimensional X-ray powder diffraction experiments*. PhD thesis, University in Stuttgart, Germany, 2011.

[28] P. Y. Zavalij V. K. Pecharsky. *Fundamentals of Powder Diffraction and Structural Characterization of Materials*. Kluwer Academic Publishers, 2003.

[29] H. M. Rietveld. *Acta Cryst.*, 22:151, 1967.

[30] H. M. Rietveld. *J. Appl. Cryst.*, 2:65–71, 1969.

[31] A. Le Bail, H. Duroy, and J. L. Fourquet. *Mater. Res. Bull.*, 23:447–452, 1988.

[32] A. K. Cheetam. Structure determination from powder diffraction data:an overview. *http://fds.oup.com/www.oup.co.uk/pdf/0-19-850091-2.pdf*.

[33] Christopher Hammond. *The Basics of Crystallography and Diffraction*. Oxford University Press, 2009.

[34] V. K. Peterson. *Powder Diffraction*, 1:14–17, 2005.

[35] Germany 2007. TOPAS version 4.1 Bruker-AXS, Karlsruhe.

[36] 1999 G. Stoe, Software Package Stoe Stadi P.

[37] 2000. icdd in PCPDFWIN 2.2.

[38] G. Cakmak, J. Nuss, and M. Jansen. *Z. Anorg. Allg. Chem.*, 635:631636, 2009.

[39] Bruker AXS Inc. Madison WI USA 1997 Bruker AXS: SMART Bruker Molekular Analysis Research Tool, version 5.632.

[40] G. M Sheldrick: SADABS Bruker AXS area detector scaling and University of Gttingen Germany 2008 absorption, version 2008/1.

[41] G. M. Sheldrick. *Acta Crystallogr., Sect. A: Found. Crystallogr.*, 64:112–122, 2008.

[42] V. Saltykov. *The Relativistic Effect in Intermetallic Phases of Gold, Platinum and Thallium.* PhD thesis, Dissertation an der Universitt Stuttgart, 2011.

[43] R. Bachmann, F. J. DiSalvo Jr.and T. H. Geballe, R. L. Greene, R. E. Howard, C. N. King, H. C. Kirsch, K. N. Lee, R. E. Schwall, H. U. Thomas, and R. B. Zubeck. *Review of Scientific Instruments*, 43:205, 1972.

[44] J. S. Hwang, K. J. Lin, and C. Tien. *Review of Scientific Instruments*, 68:94, 1997.

[45] http://www.phys.ethz.ch/phys/students/bachelor/vp/vp-expliste/esr.pdf.

[46] H. Lueken. *Magnetochemie.* Teubner, Stuttgart, 1999.

[47] R. F. Walker H. D. Fair. *Energetic Materials (Volume 1), Physics and Chemistry of the Inorganic Azides.* Plenum Press, New York and London, 1864.

[48] Fernindar Enke. *Handbuch der Prparativen Anorganischen Chemie, Vol. 2.* Stuttgart, 1978.

[49] S. G. Wang and W.H.E. Schwarz. *J. Alloys Compd.*, 246(12):131 – 138, 1997.

[50] R. Hoppe, D. Fischer, and J. Schneider. *Z. Anorg. Allg. Chem.*, 625:1135–1142, 1999.

[51] D. Kissel and R. Hoppe. *Z. Anorg. Allg. Chem.*, 559:40–48, 1988.

[52] R. Hoppe and H.J. Roehrborn. *Naturwissenschaften*, 49:419–420, 1962.

[53] R. Hoppe and W. Losert. *Z. Anorg. Allg. Chem.*, 521:69–78, 1985.

[54] G. Wagner and R. Hoppe. *Journal of the Less-Common Metals*, 120:225–237, 1986.

[55] G. Wagner and R. Hoppe. *Z. Anorg. Allg. Chem.*, 549:26–34, 1987.

[56] W. Carl and R. Hoppe. *Z. Anorg. Allg. Chem.*, 574:79–88, 1989.

[57] W. Losert and R. Hoppe. *Z. Anorg. Allg. Chem.*, 515:87–94, 1984.

[58] S. Wang and W. Schwarz. *J. Chem. Phys.*, 109(17):7252–7262, 1998.

[59] R. Burbank, W. Falconer, and W. Sunder. *Science*, 178:1285–1286, 1972.

[60] K. Đuriš, U. Müller, and M. Jansen. *Z. anorg. allg. Chem.*, 638(5):737–743, 2012.

[61] O. Jarchow. *Zeitschrift für Kristallographie*, 136:122–134, 1972.

[62] M. Crespin, P. Levitz, and L. Gatineau. *J. Chem. Soc.Faraday Trans. 2*, 79:1181–1194, 1983.

[63] P. Levitz, M. Crespin, and L. Lucien. *J. Chem. Soc. Faraday Trans. 2*, 79:1195–1203, 1983.

[64] V.I. Anisimov, D. Bukhvalov, and T. M. Rice. *Phys. Rev. B*, 59:7901–7906, Mar 1999.

[65] M. Crespin, J.M. Bassat, P. Odier, P. Mouron, and J. Choisnet. *J. Solid State Chem.*, 84(1):165 – 170, 1990.

[66] M. Crespin, C. Landron, P. Odier, J.M. Bassat, P. Mouron, and J. Choisnet. *J. Solid State Chem.*, 100(2):281 – 291, 1992.

[67] V. Poltavetsand, K. Lokshin, S. Dikmen, M. Croft, T. Egami, and M.Greenblatt. *J. Am. Chem. Soc.*, 128(28):9050–9051, 2006. PMID: 16834375.

[68] V.V. Poltavets, K.A. Lokshin, M. Croft, T.K. Mandal, T. Egami, and M. Greenblatt. *Inorg. Chem.*, 46:10887–10891, 2007.

[69] R. Scholder. *Angew. Chem.*, 70(19):583–594, 1958.

[70] H. D. Wasel-Nielen and R. Hoppe. *Z. Anorg. Allg. Chem.*, 359:36–40, 1968.

[71] H. Sabrowsky and R. Hoppe. *Z. Anorg. Allg. Chem.*, 358:241–256, 1968.

[72] R. Hoppe K. Hestermann. *Z. Anorg. Allg. Chem.*, 360(3-4):113–116, 1968.

[73] D. Fischer, W. Carl, H. Glaum, and R. Hoppe. *Z. Anorg. Allg. Chem.*, 585:75–81, 1990.

[74] F. Schenk and R. Hoppe. *Naturwissenschaften*, 56:414–414, 1969.

[75] W. Burow, J. Birx, F. Bernhardt, and R. Hoppe. *Z. Anorg. Allg. Chem.*, 619:923–933, 1993.

[76] A. Möller, M. A. Hitchman, E. Krausz, and R. Hoppe. *Inorg. Chem.*, 34:2684–2691, 1995.

[77] A. J. Bridgeman. *J. Chem. Soc. Dalton Trans.*, 24:4555–4562, 1996.

[78] K. Đuriš, O. Magdysyuk, and M. Jansen. *Solid State Sciences*, 14(10):1399–1404, October 2012.

[79] U. Müller. *Symmetriebeziehungen zwischen verwandten Kristallstrukturen.* Vieweg+Teubner Verlag, 2012.

[80] H. Flack. *Acta Crystallographica Section A*, 39:876–881, 1983.

[81] G. M. Scheldrick in SADABS. Bruker axs area detector scaling and absorption, version 2008/1, vol. page Scheldrick08, 2008.

[82] P. Engel, T. Matsumoto, G. Steinmann, and H. Wondratschek. *Suppl. no 1 der Z. Kristallogr.*, 1984.

[83] K. Cenzual, L. M. Gelato, M. Penzo, and E. Parthe. *Acta Crystallographica B*, 47:433–439, 1991.

[84] H. Yamane, S. Kikkawa, and M. Koizumi. *J. Solid State Chem.*, 71:1–11, 1987.

[85] P. Hoehn and R. Kniep. *Zeitschrift für Naturforschung, Teil B. Anorganische Chemie, Organische Chemie*, 47:434–436, 1992.

[86] J. Jager and R. Kniep. *Zeitschrift für Naturforschung, Teil B. Anorganische Chemie, Organische Chemie*, 47b:1290, 1992.

[87] A. Helms and W. Klemm. *Z. Anorg. Allg. Chem.*, 242:33–40, 1939.

[88] D. Orobengoa, C. Capillas, M. Aroyo, and J. Perez-Mato. *Journal of Applied Crystallography*, 42:820833., 2009.

[89] A. Möller. *Z. Anorg. Allg. Chem.*, 628(1):77–80, 2002.

[90] M. Hitchman, H. Stratemeier, and R. Hoppe. *Inorg. Chem.*, 27(14):2506–2510, 1988.

[91] K. Đuriš and M.Jansen. *Z. Naturforsch.*, 67b:57–60, 2012.

[92] M. Jansen M. Sofin. *Z. Anorg. Allg. Chem.*, 627:2115–2117, 2001.

[93] Patrick Marcel Richard Ribeiro. *One-Dimensional Quantum Magnets in Cuprates: Single Crystal Growth and Magnetic Heat Transport Studies*. PhD thesis, der Fakultt fr Mathematik und Naturwissenschaften der Technischen Universitt, Dresden, 2007.

[94] Masashi Hase, Ichiro Terasaki, and Kunimitsu Uchinokura. *Phys. Rev. Lett.*, 70(23):3651–3654, June 1993.

[95] M. Matsuda and K. Katsumata. *Phys. Rev. B*, 55:R11 953–R11 956, 1997.

[96] J. Schlappa, K. Wohlfeld, K. J. Zhou, M. Mourigal, M. W. Haverkort, V. N. Strocov, L. Hozoi, C. Monney, S. Nishimoto, S. Singh, A. Revcolevschi, J.-S. Caux, L. Patthey, H. M. Ronnow, J. van den Brink, and T. Schmitt. *Nature*, 485(7396):82–85, May 2012.

[97] J. Nuss, M. A. Senaris-Rodriguez, Prasad L. V. K. Dasari, M. Stahl, and M. Jansen. *J. Am. Chem. Soc.*, 134 (28):11734–11739, 2012.

[98] A. P. Ramirez. *Journal of Physics: Condensed Matter*, 9:8171–8199, 1997.

[99] P. Horsch, M. Sofin, M. Mayr, and M. Jansen. *Phys. Rev. Lett.*, 94(7):076403–076403–4, February 2005.

[100] A. Möller. *Z. Anorg. Allg. Chem.*, 627:1192–1198, 2001.

[101] K. Hestermann and R. Hoppe. *Z. Anorg. Allg. Chem.*, 367:249–260, 1969.

[102] G. Brauer. *Handbuch der Prparativen Anorganischen Chemie*. Ferdinand Enke Verlag, 1978.

[103] H. Zentgraf, K. Claes, and R. Hoppe. *Z. Anorg. Allg. Chem.*, 462:92–105, 1980.

[104] P. W. Selwood. *Magnetochemistry*. Interscience, New York, 1956.

[105] M. G. Banks, R. K. Kremer, C. Hoch, A. Simon, B. Ouladdiaf, J.-M. Broto, H. Rakoto, C. Lee, and M.-H. Whangbo. *Phys. Rev. B*, 80:024404, 2009.

[106] D. C. Johnston, R. K. Kremer, M. Troyer, X. Wang, A. Klümper, S. L. Bud'ko, A. F. Panchula, and P. C. Canfield. *Phys. Rev. B*, 61:9558–9606, Apr 2000.

[107] F. Heidrich-Meisner, A. Honecker, and T. Vekua. *Phys. Rev. B*, 74:020403, Jul 2006.

[108] M. Sofin. *Neue Alkalioxometallate ber die Azid/Nitrat-Route*. PhD thesis, Von der Fakultät Chemie der Universität Stuttgart, 2003.

[109] G. M. Sheldrick. Twinabs bruker axs scaling for twinned crystals, version 2008/4, university of gttingen, germany 2008.

[110] E. Plekhanov, A. Avela, and F. Mancini. *Journal of Physics: Conference Series*, 200(2):022047, 2010.

[111] F. Sapina, J. Rodrguez-Carvajal, M.J. Sanchis, R. Ibanez, A. Beltran, and D. Beltran. *Solid State Commun.*, 74(8):779–784, May 1990.

[112] R. J. Ortega, P. J. Jensen, K. V. Rao, F. Sapina, D. Beltran, Z. Iqbal, J. C. Cooley, and J. L. Smith. *J. Appl. Phys.*, 83(11):6542–6544, 1998.

[113] N. Imanishi, K. Shizuka, T. Ikenishi, T. Matsumura, A.Hirano, and Y. Takeda. *Solid State Ionics*, 177(1516):1341–1346, June 2006.

[114] A. Coelho. *J. Appl. Cryst.*, 33:899–908, 2000.

[115] A. Coelho. *J. Appl. Crystallogr.*, 38:455–461, 2005.

[116] G. Oszlanyi and A. Suto. *Acta Crystallographica Section A*, A60:134–141, 2004.

[117] G. Oszlanyi and A. Suto. *Acta Cryst.*, A61:147–152, 2005.

[118] A. Coelho. *Acta Crystallogr A.*, A63:134–141, 2007.

[119] E. Quarez, M.Huve, P. Roussel, and O. Mentre. *J. Solid State Chem.*, 165(2):214–227, May 2002.

[120] G. Tams and Hk. Müller-Buschbaum. *Z. Anorg. Allg. Chem.*, 617(11):19–22, 1992.

[121] G. Tams Hk. Müller Buschbaum, C. Lang. *Zeitschrift fuer Naturforschung, Teil B. Anorganische Chemie, Organische Chemie*, 50:681–683, 1995.

[122] M. Scheikowski and Hk. Müller-Buschbaum. *Z. Anorg. Allg. Chem.*, 620:313–318., 1994.

[123] P. Sonne and Hk. Müller-Buschbaum. *Z. Anorg. Allg. Chem.*, 619:1004–1006., 1993.